

Feature-Preserving Image Restoration and Its Application in Biological
Fluorescence Microscopy

Zhen Qiu

Submitted for the degree of Doctor of Philosophy

Heriot-Watt University

School of Engineering and Physical Sciences

January 2013

The copyright in this thesis is owned by the author. Any quotation from the thesis or use of any of the information contained in it must acknowledge this thesis as the source of the quotation or information.

Abstract

This thesis presents a new investigation of image restoration and its application to fluorescence cell microscopy. The first part of the work is to develop advanced image denoising algorithms to restore images from noisy observations by using a novel feature-preserving diffusion approach. I have applied these algorithms to different types of images, including biometric, biological and natural images, and demonstrated their superior performance for noise removal and feature preservation, compared to several state of the art methods. In the second part of my work, I explore a novel, simple and inexpensive super-resolution restoration method for quantitative microscopy in cell biology. In this method, a super-resolution image is restored, through an inverse process, by using multiple diffraction-limited (low) resolution observations, which are acquired from conventional microscopes whilst translating the sample parallel to the image plane, so referred to as translation microscopy (TRAM). A key to this new development is the integration of a robust feature detector, developed in the first part, to the inverse process to restore high resolution images well above the diffraction limit in the presence of strong noise. TRAM is a post-image acquisition computational method and can be implemented with any microscope. Experiments show a nearly 7-fold increase in lateral spatial resolution in noisy biological environments, delivering multi-colour image resolution of ~ 30 nm.

Acknowledgements

This thesis cannot be completed without the support, guidance and love from many people around me.

First and foremost, I would like to especially thank my supervisor, Dr. Weiping Lu. With his patience and wisdom, Weiping has spent great efforts to guide me in each phase in preparing this doctoral thesis, from conceptual initialization, mathematical analysis and algorithm design to numerical result analysis, and extending to paper writing and talk preparation. Besides his profound scientific vision, his extraordinary research passion and good methodologies in all aspects are things that I shall cherish during my whole research career. It is my great pleasure to have enjoyed the opportunity to work with him.

I would like to express my gratitude to Prof. Alan H. Greenaway for generously sharing his intellect and ideas. His smiling face, patience, and unswervingly offering of a research position in his group after this thesis are constant sources of encouragement to me.

I gratefully acknowledge my former colleague, Dr. Lei Yang, at the Heriot-Watt University. Lei is not only a good friend but a great mentor to me personally. I am always inspired by our daily enjoyable discussions, and always encouraged by his attitude towards research. I also benefit a lot from him and his wife, Rongping Xu, for my living in Edinburgh.

I am grateful to Dr. Colin Rickman and Prof. Rory Duncan, for sharing their knowledge in biology and providing fluorescence microscopy images to me. Their great senses of humour during our discussions are really impressive.

My thanks also go to my friends and colleagues, Yan Feng, Yuewei Liu, Jinghua Sun, Yujia Cheng, Ai Lien Ong and Ben Birns for their unconditional friendship and supports in Edinburgh. Thank my mates in DB 2.40 and many others in “Chaplaincy” for moral support over the past few years.

Among all my former advisors, I want to thank Prof. Yuanyuan Wang and Prof. Weiqi Wang at Fudan University, for leading me to the signal and image processing path during my master phase, and continuously encouraging me during my doctoral study.

This thesis would be impossible without my parents' love and sacrifice. My gratitude to them is beyond what I can express in words. Last, and most definitely not the least, I want to thank my loving wife, Jing He, for standing by me through my years in Edinburgh, for believing in me and making my life always so wonderful. I am lucky to have her by my side.

Table of Contents

Abstract	ii
Acknowledgements	iv
Table of Contents	vii
List of Publications by the Candidate	xi
Chapter 1	1
Introduction	1
1.1 Background	1
1.1.1 Image Restoration	1
1.1.2 Image Denoising	2
1.1.3 High-Resolution Image Restoration	3
1.1.4 Super-Resolution Imaging	4
1.1.5 Image Restoration in Fluorescence Microscopy and Main Challenges	5
1.2 Contributions and Organization of the Thesis	6
Part I	9
Image Denoising	9
Chapter 2	10
Image Denoising – A Review	10
2.1 Introduction	10
2.2 Spatial-domain Denoising	11
2.2.1 Variational Methods	11
2.2.2 Neighborhood Filter	19
2.3 Transform-Domain Denoising Methods	25
2.4 Summary	26
Chapter 3	29
A Feature-Preserving Nonlinear Anisotropic Diffusion for Denoising Images Containing Blobs and Ridges	29
3.1 Introduction	29

3.2	Second-order Nonlocal Difference.....	32
3.2.1	<i>Nonlocal Difference</i>	33
3.2.2	<i>Second-order Nonlocal Difference</i>	35
3.2.3	<i>Directional Second-order Nonlocal Difference in 2-D Images</i>	39
3.2.4	<i>Isotropic Second-order Nonlocal Difference in 2-D Images</i>	42
3.3	Feature-Preserving Diffusion	44
3.4	Experiments	47
3.4.1	<i>1-D Signals</i>	49
3.4.2	<i>2-D Images</i>	50
3.5	Conclusion and Discussion	59
Chapter 4.....		61
A Generalized Feature-preserving Nonlinear Anisotropic Diffusion Method for Denoising Natural Images		61
4.1	Introduction	61
4.2	A Combined Nonlocal Difference	62
4.3	Generalized Feature-Preserving Nonlinear Diffusion	64
4.4	Experiments	65
4.4.1	<i>1-D Signals</i>	66
4.4.2	<i>2-D Images</i>	67
4.5	Conclusions and Discussion.....	75
Part II		77
Super-Resolution in Fluorescence Microscopy		77
Chapter 5.....		78
Super-Resolution Fluorescence Microscopy for Cell Imaging		78
5.1	Introduction	78
5.2	Super-Resolution in Fluorescence Microscopy.....	79
5.3	Current Super-Resolution Fluorescence Microscopy Techniques	81
5.3.1	<i>Hardware-based SR Fluorescence Microscopy</i>	82
5.3.2	<i>Single Molecule Localization Microscopy</i>	85
5.4	Summary	88

Chapter 6.....	90
Feature-Preserving Super-Resolution Restoration for Fluorescence Microscopy	90
6.1 Introduction	91
6.2 Feature-Preserving SR Restoration.....	93
6.2.1 SR Restoration by Optimization of an Energy Function.....	93
6.2.2 A New Prior Model	96
6.2.3 Energy Minimization	98
6.2.4 Translation Microscopy (TRAM)	100
6.3 Experiments	100
6.3.1 Validation on Synthetic Data.....	101
6.3.2 Validation on Face Data.....	107
6.3.3 Validation on Fluorescence Microscopy Data.....	109
6.4 Conclusion.....	113
Chapter 7 Conclusion	115
Appendix	118
Energy minimization in Feature-Preserving Super-Resolution Restoration	118
A.1 Algorithm Procedure	118
A.2 Numerical implementation	123
References	127

List of Publications by the Candidate

1. **Z. Qiu**, L. Yang, R. Duncan, C. Rickman, and W. Lu, “Multi-color super-resolution translation microscopy,” (submitted to *Nature Methods*).
2. L. Yang, A. R. Dun, K. J. Martin, **Z. Qiu**, A. Dunn, G. J. Lord, W. Lu, R. R. Duncan, and C. Rickman, “Secretory vesicles are preferentially targeted to areas of low molecular SNARE density,” *PLoS ONE*, vol. 7, no. 11, pp. e49514, 2012.
3. L. Yang, **Z. Qiu**, A. H. Greenaway, and W. Lu, “A new framework for particle detection in low-SNR fluorescence live-cell images and its application for improved particle tracking,” *IEEE Transactions on Biomedical Engineering*, vol. 59, no. 7, pp. 2040-2050, 2012.
4. **Z. Qiu**, L. Yang, and W. Lu, “A new feature-preserving nonlinear anisotropic diffusion for denoising images containing blobs and ridges,” *Pattern Recognit. Lett.*, vol. 33, no. 3, pp. 319-330, 2012.
5. **Z. Qiu**, L. Yang, and W. Lu, “A new feature-preserving nonlinear anisotropic diffusion method for image denoising,” *Proc. BMVC*, vol. 22, pp. 73.1-73.11, 2011.
6. L. Yang, R. Parton, G. Ball, **Z. Qiu**, A. H. Greenaway, I. Davis, and W. Lu, “A 2D+t feature-preserving non-local means filter for image denoising and improved detection of small and weak particles,” *Proc. BMVC*, vol. 21, pp. 14.1-14.11, 2010.
7. L. Yang, R. Parton, G. Ball, **Z. Qiu**, A. H. Greenaway, I. Davis, and W. Lu, “An adaptive non-local means filter for denoising live-cell images and improving particle detection,” *Journal of Structural Biology*, vol. 172, no. 3, pp. 233-243, 2010.

Chapter 1

Introduction

1.1 Background

1.1.1 Image Restoration

In recent years, images and videos have become integral parts of our lives. Applications now range from casual documentation of events [1] and visual communication [2], to the more serious surveillance [3], medical [4] and biological fields [5]. This has led to an ever increasing demand for accurate and visually pleasing images with high image quality for various tasks in these applications. However, images acquired by modern digital cameras inevitably undergo a degrading process, which as shown in Fig. 1.1, involves the corrupting of an original high-quality image due to many effects, such as blurring, down-sampling, contamination of photon or dark-current noises, etc. Although several models have been proposed to mathematically formulate such degrading process based on the optical design in different applications, the most popular and generalized one is still the forward model given as [6],

$$\mathbf{J} = \mathbf{P} \cdot \mathbf{I} + \mathbf{N}, \quad (1.1)$$

where the column vectors \mathbf{J} and \mathbf{I} consist of row-wise concatenations of the acquired and original images, \mathbf{N} represents the noise corruption and \mathbf{P} is a matrix describing blurring effects due to camera motion, atmosphere turbulence, point spread function (PSF) of the imaging system, etc.. Since the high-quality image \mathbf{I} is not available to

observers, it can only be estimated based on the acquired image J from imaging devices which is also called as observation. Image restoration aims to “invert” the imaging process Eq. (1.1) to recover an image that is as close as possible to the original one, I . Image restoration is therefore an inverse process.

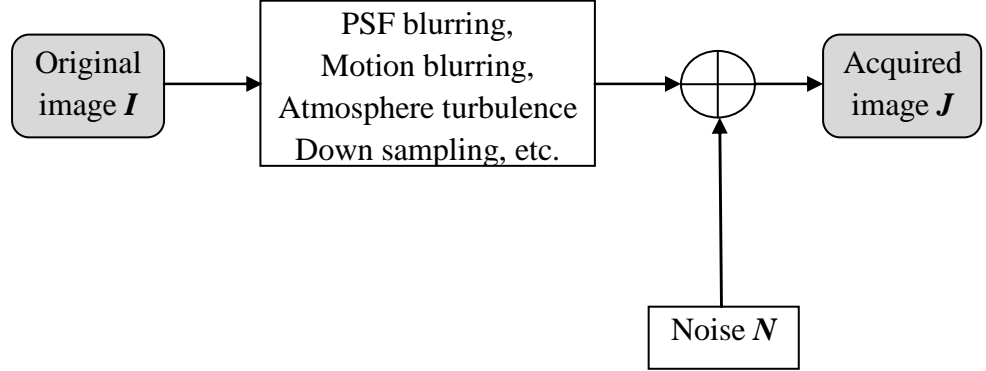


Fig. 1.1 A flowchart of image formation process

1.1.2 Image Denoising

In fluorescence microscopy or medical imaging, the atmosphere turbulence and motion blur in most cases can be neglected so the blurring occurs mostly due to the PSF. When the object size is much (50-100 times) larger than the PSF size, the blurring matrix P can be considered to be unitary. Image restoration is then simplified as a denoising process, which estimates a noise-free image from its noisy observation. The noise N in Eq. (1.1) can arise from different sources and in different forms, including fixed-pattern, dark-current, shot, thermal, quantization noise and so on [7], all of which can be modelled as a random variable with a specific probability density distribution (PDF) [8]. Noise removal is then often achieved by smoothing, i.e., replacing the randomly fluctuating intensities with their mean values. However, the smoothing process is a double-edge sword for image restoration; on one hand it can suppress noise in the background regions; on the other hand it can blur the features of interest in the image, resulting in an unsuccessful restoration. To avoid this problem, denoising should be locally adapted in the images, so it is encouraged in background regions while inhibited in the vicinity of the features or structures.

In general, an edge is a fundamental feature that underlies more complicated features or structures in an image. The latter can be preserved as long as edges are preserved after denoising. Since the edge can be characterised by a first-order difference (gradient), most existing methods [9-18] use the gradient as an edge detector to reject smoothing at edges and permit smoothing in other places. These methods have achieved

remarkable performance of improving image quality under noise contamination both visually and quantitatively. Here I use a simple example to illustrate the effectiveness of edge preserving in denoising. Fig. 1.2 shows an original (noise-free) and noisy images together with two denoised images by pure smoothing and by total variation (TV) diffusion [19] respectively, the last of which is an edge-preserving denoising method. As seen, although both Fig. 1.2(c) and (d) remove noise effectively, the former brings unpleasant blurring effects.

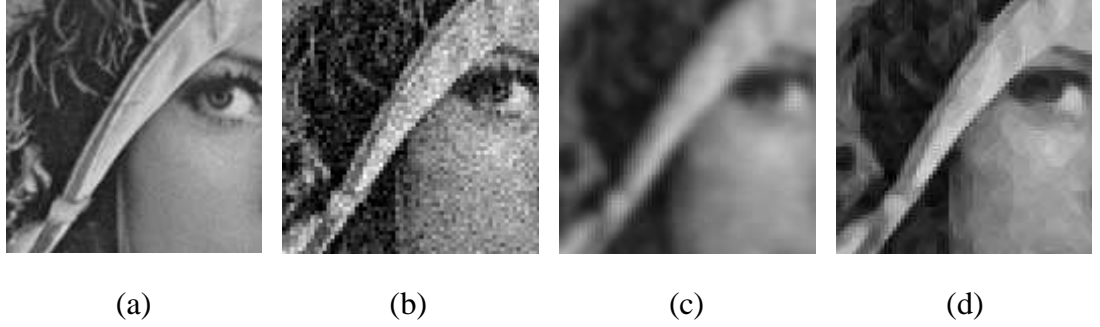


Fig. 1.2 Denoising test on a natural image. (a - b) The original (noise-free) and noisy image corrupted by additive white Gaussian noise of Std $\sigma_n = 20$; (c - d) Denoised results by linear and TV diffusion [19], respectively.

1.1.3 High-Resolution Image Restoration

When the blurring matrix \mathbf{P} in Eq. (1.1) is non-unitary, image restoration involves not only noise removal but also improving the image resolution that has been decreased during the imaging process to offer more image content that may be critical in various applications. This is usually called high-resolution (HR) image restoration. Compared to denoising, HR restoration is a more sophisticated process which is required to remove noise while recovering fine structures that are lost in the image degrading process. Such goal can be achieved through an inverse process by using multiple low resolution (LR) observations from a same HR image due to the degrading process. Through the inverse process, the contents of the restored image are increased [20] with combined information [21] from different LR observations.

Similar to image denoising, noise removal during the inverse process of HR restoration should be also spatially adapted to avoid over-smoothing of features of interests. To date, noise removal in HR restoration is undertaken based on the edge-preservation concept [22]; features are restored as long as all the edges are preserved in the inverse process. Fig. 1.3(a-b) shows respectively a LR and HR image obtained by a

Bayesian HR restoration approach that uses edges to model the visual complexity of the image [23]. As seen, details that are blurred in the LR image are clearly distinguishable in the resulting HR one after the HR restoration.

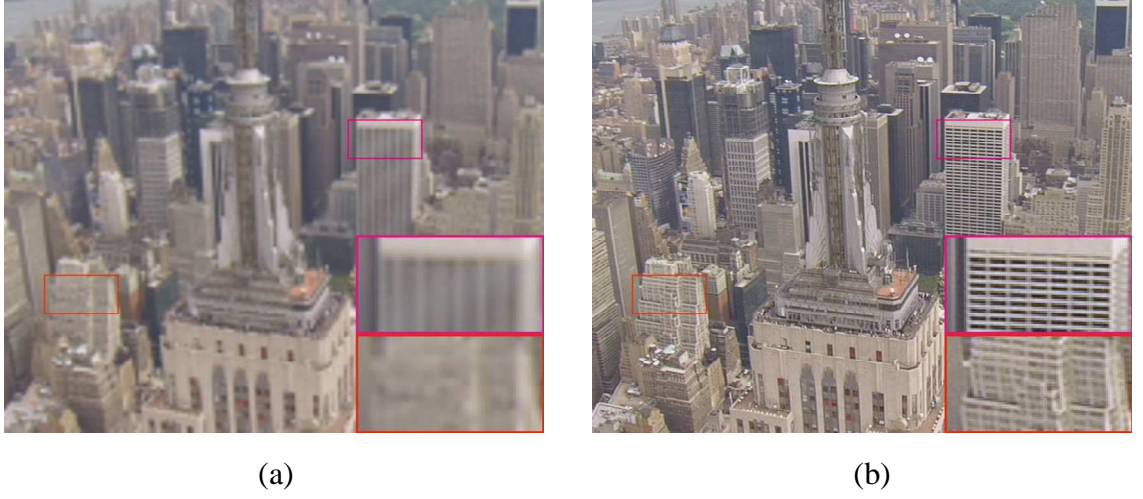


Fig. 1.3 An example of HR restoration. (a-b) the LR image and HR result by a Bayesian HR restoration [23].

1.1.4 Super-Resolution Imaging

In microscopy, the resolution of an imaging system is measured by the minimal distance of two distinguishable (resolvable) points. Such distance is often restricted by the diffraction limit, which is determined by the size of PSF of the imaging system and is given by the Abbe diffraction criterion of $\lambda/(2NA)$ [24], where λ is the wavelength of light and NA is the numerical aperture of the lens that characterizes the range of angles over which the lens can accept or emit light [25]. Resolutions that exceed this limit are referred to as super-resolution (SR). There are currently two popular approaches to generate SR images in microscopy imaging. The first one aims to reduce the size of PSF by employing optical patterning of the excitation and a nonlinear response of the sample, such as stimulated emission depletion (STED) [26] and structured illumination microscopy (SIM) [27]. The second approach is single-molecule localization microscopy (SMLM) [28], which acquires images of individual single molecule at different time duration and then locates the peaks of each molecule. A SR image is finally generated by mapping together all the individual peaks [28]. The two approaches have yielded an order of magnitude improvement in spatial resolution and are currently two dominant methods to achieve SR in microscopy.

1.1.5 Image Restoration in Fluorescence Microscopy and Main Challenges

In biology, various biological processes related to cells can be observed only when proteins can be visualized and located through microscopes. Unfortunately, cells are not suitable for direct optical visualization since they are mostly transparent in natural state, and the immense numbers of molecules that constitute them are optically indistinguishable from one another. This makes the identification of a particular protein a very complex task. However, if a bright marker that can be directly observed with visible lights were attached to the protein of interest, it would be able to very precisely indicate its position. With several bright markers being attached together to the proteins, I can then easily visualize these biological samples. For this purpose, fluorescence microscopy was proposed to visualize biological processes by marking samples with fluorescence and then generating images using microscopes.

Fluorescence microscopy was invented almost a century ago. But it was not until the 1990s that fluorescence microscopy began to revolutionize the biological research, when Chalfie, et al. [29] succeeded in expressing a green fluorescent protein occurring in a jelly fish species onto other organisms by modifying their genome to code for this protein. To date, fluorescence microscopy has been the primary modality for biological imaging, and experimental requirements, such as live-cell imaging with high- or super-resolution, are continuously stimulating new developments.

However, the application of fluorescence microscopy in live-cell imaging is still hindered by the low quality of the acquired images. Firstly, the live-cell fluorescence images are often contaminated by severe noise. In fluorescence live-cell microscopic imaging there is always a compromise between image quality and cell viability. Excitation of fluorescent probes causes photobleaching and phototoxicity to cells, which limit the light intensity and exposure times that can be used. The requirement to image fast and in multiple dimensions to capture dynamic intracellular events also constrains illumination and exposure regimes and requires fast camera readout. This in turn results in low signal-to-noise ratio (SNR) fluorescence images with mixed Poisson-Gaussian noise [30, 31]. Secondly, the current two dominant SR imaging approaches introduced in the last subsection have their limitations in fluorescence microscopy: they either involve complex optical design or work slow and are computationally intensive [32], and both cases require special fluorephores that current techniques cannot provide in an easy way. To solve these problems in live-cell and SR imaging, image restoration, as a computational approach independent of the optical and chemical design, is therefore an indispensable tool to improve the SNR of images, and an alternative choice for SR

imaging to facilitate both visual and computational analysis of the data in the fluorescence microscopy community.

As discussed earlier, most existing image restoration approaches are based on the edge-preserving concept. These methods have achieved remarkable performance in many applications, such as medical imaging, satellite imaging, security surveillance and mobile phones[33-36]. Compared to these applications, fluorescence microscopy images are more challenging. Fluorescence cell images of intracellular structures are often contaminated by very severe mixed Poisson-Gaussian noise and contain abundant and heterogeneous features of various shapes and sizes, and complex networks that are made of these features. Sizes of features in these images are also much smaller, sometime by 10 times than the resolution limit [37], compared to 2-3 times in typical medical images. In general, edges embedded in complex and small features are prone to noise contamination. In other words, when the edges are partly lost to a certain extent or weak and contaminated severely by noise, these methods may not be able to recover these edges and thus fail to restore other features that are made of by the edges, such as blobs, ridges and textures, which are important in the study of cell biology. As such, traditional edge-preservation image restoration methods do not perform well in fluorescence microscopy. This calls for a more sophisticated approach for feature characterization in the image restoration methods to reverse the imaging process Eq. (1.1) for a robust and accurate estimation of the original fluorescence microscopical images.

1.2 Contributions and Organization of the Thesis

The remainder of this thesis is organized into two parts as follows.

In the first part, which includes Chapter 2, 3, and 4, I study the problem of image denoising. In Chapter 2 I firstly review several popular denoising methods and briefly analyze their similarities and dissimilarities. Based on the analysis, I propose in Chapter 3 a novel second-order nonlocal difference (2^{nd} -order NLD) as a feature detector and incorporate it into a diffusion process to form a novel feature-preserving nonlinear anisotropic diffusion model for denoising images containing blobs and ridges. Experiments show that the new diffusion filter outperforms many popular filters for preserving blobs and ridges, reducing noise and minimizing artifacts. In Chapter 4, I further extend our work in the previous chapter. We propose a new and more sophisticated feature detector by combining 1^{st} - and 2^{nd} -order NLD for a more generalized nonlinear anisotropic diffusion model that denoises natural images

containing not only blob and ridge feature but also other complex features under extreme severe noise contamination.

In the second part, which includes Chapter 5 and 6, I study the SR restoration in the application of fluorescence cell imaging. I first provide a review on existing SR imaging in fluorescence cell imaging in Chapter 5. In Chapter 6, I then propose to use the HR restoration in the image processing community to achieve SR imaging in fluorescence microscopy. I explore a new prior model based on the feature detector developed in the first part to form a feature-preserving SR restoration (FP-SR) method. By combining the FP-SR restoration with a multiple LR image acquisition modality of translating the microscopes, I present translation microscopy (TRAM) as a novel, simple and inexpensive super-resolution imaging technique. It can be implemented with any microscopes and result in a 7-fold increase in lateral spatial resolution in noisy biological environments, delivering multi-colour image resolution of $\sim 30\text{nm}$.

Part I

Image Denoising

Chapter 2

Image Denoising – A Review

Abstract: I start my study from image denoising in the first part of the thesis. A major challenge facing a denoising algorithm is to suppress noise while preserving features and fine details in the images. Over the years, researchers have proposed many different methods that attempt to achieve these contradictory goals. These methods vary widely in their approaches. Generally, denoising approaches can be categorized based on their operation domains - spatial or transform domain. In this chapter, I briefly review some of the most popular approaches within each category. I also briefly analyze their similarities and dissimilarities and point out that most of these approaches are based on the edge-preserving concept; more complicated features or structures can be preserved as long as edges are preserved.

2.1 Introduction

Traditionally, image restoration is to reduce undesirable degradations during the imaging process while preserving important features such as edges and textures. Perhaps the most fundamental image restoration task is image denoising: an ideal image I is measured in the presence of an additive zero-mean noise, N , with standard deviation (Std) σ_n . The noisy observation J can then be formulated as,

$$J = I + N, \quad (2.1)$$

where N can be independent or dependent of I . Given Eq. (2.1), image denoising then aims to remove the noise N from J , in order to achieve a denoised image that is as close as possible to the original image I . In general, the noise corruption is hardly avoided in an imaging process since intensity quantization can also bring noise [8], as discussed in Chapter I. As such, image denoising forms a preliminary but important step for various subsequent tasks, such as image segmentation [38], feature extraction [39], pattern recognition [40], object tracking [41], etc. There now exist many denoising methods

that vary widely in their approaches. Broadly, these methods can be categorized based on the domains they operate - spatial or transform domain. Spatial-domain methods are mainly made of variational methods [9, 12, 13, 42-52] and neighborhood filters [11, 16, 53-56]. Since our study for image denoising belongs to the variational method, in the reminder of this chapter, I review and discuss several existing spatial-domain methods for image denoising. We then briefly outline some of the most popular approaches within the transform-domain category [57-70].

2.2 Spatial-domain Denoising

Denoising methods where the pixel intensities are used directly in the denoising process are said to be spatial-domain filters, which consist of the variational methods and neighbourhood filters. The former usually uses the calculus of variations to denoise the image in an iterative scheme. The latter performs the denoising of an image pixel by its neighboring pixel intensities.

2.2.1 Variational Methods

Of all denoising methods, variational methods have been particularly successful [71], and remain one of the most active areas of research in mathematical image processing and computer vision [72, 73]. Variational methods search for solutions of an image denoising problem by minimising an appropriate functional. When using the calculus of variations, the minimization technique of the chosen functional routinely involves the solution of diffusion models derived as necessary optimality conditions [10].

Let us first consider the following functional $E(I)$ defined in the space of the original two-dimensional (2-D) image $I: \Omega \subset \mathbb{R}^2 \rightarrow \mathbb{R}$ over a support Ω as,

$$E(I) = \int_{\Omega} f(I) d\mathbf{x}, \quad (2.2)$$

where $f() \geq 0$ is an increasing function, $\mathbf{x} = [x, y]^T \in \Omega$ denotes the image pixel and the image support Ω is open and bounded. Given Eq. (2.2), the original image I is then denoised by solving the following minimization problem,

$$\hat{I} = \arg \min_I E(I), \quad (2.3)$$

which can be estimated by computing the Euler-Lagrange equation of Eq. (2.2) with calculus of variations [74]. A gradient-descent solution of Eq. (2.3) can then be obtained as the following partial differential equation (PDE),

$$\begin{cases} \frac{\partial I(t)}{\partial t} = \text{div}[c(I(t))\nabla I] \\ I(t=0) = J \end{cases}, \quad (2.4)$$

where the coefficient function $c(I)$ is in the form of

$$c(I) = \frac{1}{\|\nabla I\|_2} \frac{df(\|\nabla I\|_2)}{d(\|\nabla I\|_2)}, \quad (2.5)$$

div is the divergence operator, ∇ is the gradient operator, $\|\cdot\|_2$ denotes the ℓ^2 norm and J is the noisy observation. The PDE Eq. (2.4) is in fact a diffusion equation; the image data are iteratively diffused from high-contrast regions to low-contrast to generate a sequence of smoother image $I(t)$. The image noise will be therefore gradually removed from the observation J by the smoothing behaviour, which is controlled by the diffusion coefficient (DC) $c(I)$. Based on the diffusion model, Eq. (2.4) and (2.5), many diffusion approaches have been proposed so far in the literature for image denoising. The methods have shown impressive denoising performances both visually and quantitatively. In the following, I describe some of the most classical methods.

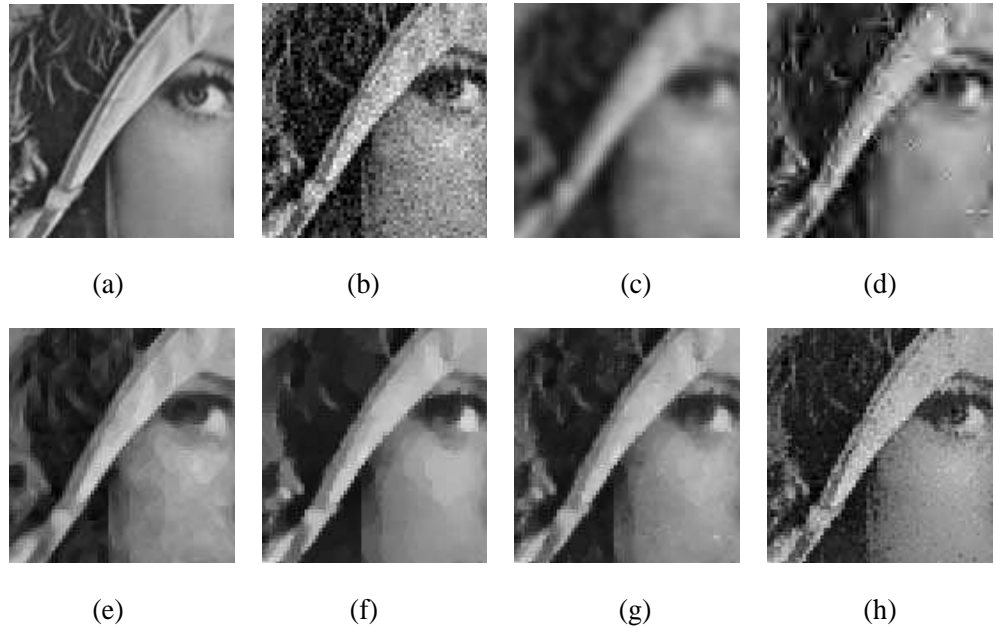


Fig. 2.1. Denoising experiences on an 8-bit natural image (a - b) original noise-free and noisy image contaminated by AWGN of Std $\sigma_N = 20$; (c - h) denoised results of linear

diffusion, P-M model, TV minimization, Tadmor–Nezzar–Vese iterated TV, Osher *et al.* iterated TV, and bilateral filter.

2.2.1.1 Linear diffusion

When I set the function f in the functional $E(I)$ Eq. (2.2) as $f(I) = \frac{1}{2} \|\nabla I\|_2^2$, the coefficient can be then obtained as $c(I) = 1$ according to Eq. (2.5). The diffusion model Eq. (2.4) is hence expressed as,

$$\begin{cases} \frac{\partial I(t)}{\partial t} = \text{div}[\nabla I] = \Delta I = \frac{\partial^2 I}{\partial x^2} + \frac{\partial^2 I}{\partial y^2}, \\ I(t=0) = J \end{cases} \quad (2.6)$$

which is equivalent to the well-known heat equation, used in physics for instance to describe heat flows through solids. Koenderink [75] proved that the solution of Eq. (2.6) at a particular time t is the convolution of the noisy image J with a normalized 2D Gaussian function G_σ of Std $\sigma_x = \sigma_y = \sigma = \sqrt{2t}$:

$$I(t) = J * G_\sigma, \quad (2.7)$$

where,

$$G_\sigma(x, y) = \frac{1}{2\pi\sigma^2} \exp\left(-\frac{x^2 + y^2}{2\sigma^2}\right). \quad (2.8)$$

The diffusion model Eq. (2.6) is thus named as the linear diffusion model since the convolution is a linear operation. Given Eq. (2.7) and (2.8), a major drawback of the linear diffusion framework is clear: the linear diffusion uniformly filters local signal features and noise little by little during the diffusion process, and thus blurs the whole structure of the image. Fig. 2.1(a-b) shows a noise-free and noisy image with additive white Gaussian noise (AWGN) of Std $\sigma_n = 20$. The denoising result by using the linear diffusion Eq. (2.6) is shown in Fig. 2.1(c). As seen, all image structures are blurred by such a linear convolution scheme.

2.2.1.2 Perona–Malik Model

To overcome the limitations of linear smoothing, Perona and Malik [9] proposed a nonlinear diffusion method. They considered a non-uniform diffusion process that reduces diffusion at image locations with a larger likelihood to be edges while encouraging diffusion at other places. This likelihood is measured by the first-order (1st-

order) difference of the local image intensities, or the gradient ∇I . Based on such consideration, they revised the DC $c(I)$ as a decreasing function $c(\nabla I)$ of the gradient ∇I in the form of

$$c(\nabla I) = \frac{1}{1 + \left(\frac{\|\nabla I\|_2}{h} \right)^2} \quad (2.9)$$

or

$$c(\nabla I) = \exp\left(-\frac{\|\nabla I\|_2^2}{h}\right), \quad (2.10)$$

where h is a gradient threshold estimated from the noise level. Combined with Eq. (2.9) or (2.10), the diffusion model, Eq. (2.4), is then referred to as Perona-Malik (PM) diffusion model. In this model, the gradient magnitude $\|\nabla I\|_2$ serves as an edge detector; if $\|\nabla I\|_2 \gg h$, then $c(\nabla I) \rightarrow 0$ and I have a stop filter that discourages the smoothing in the vicinity of the edges to preserve image details; if $\|\nabla I\|_2 \ll h$, then $c(\nabla I) \rightarrow 1$ and I perform the linear diffusion (Gaussian smoothing) in background regions to remove noise. The PM model is therefore a nonlinear diffusion process that adaptively alters the local smoothing based on the image contents. Experiments by Perona and Malik [9] were visually very impressive: edges remained stable and noise is removed after diffusion process finishes. Fig. 2.1(d) shows the denoised result by the PM model after 107 iterations. As seen by comparing Fig. 2.1(d) and (c), the PM model outperforms the linear diffusion enormously by providing better preservation of features, including eyes, hairs and hats in the girl's head.

However, since the gradient is measured by the gray-value difference of only two pixels, the gradient operator ∇I cannot achieve a robust separation of edges and noise. In other words, the gradient operator may fail to detect some weak edges or misinterpret noise as spurious edges. The PM model may therefore preserve or even enhance large variations generated by the noise and thus create artifacts in denoised images. As seen in Fig. 2.1(d), the PM model produces several speckle-like artifacts in the girl's face, which are unacceptable for the subsequent tasks such as feature detection, pattern recognition, etc..

2.2.1.3 Total Variation Model

Another well-known variational denoising method is the total variation (TV) model that was first introduced by Rudin, Osher and Fatemi [19, 46]. In the TV model, the original noise-free image I is assumed to be piecewise-constant. Namely, the image I consists of a set of flat regions (uniform intensity) separated by edges as boundaries. The image I is constant inside the flat regions but with jumps across the boundaries. Under such assumption, Rudin, et al. [46] set the function $f(I)$ in the functional $E(I)$ Eq. (2.2) as $f(I) = \|\nabla I\|$. The functional $E(I)$ Eq. (2.2) is then expressed as

$$E(I) = \int_{\Omega} \|\nabla I\|_2 dx dy, \quad (2.11)$$

with $\frac{\partial I}{\partial x} = \frac{\partial I}{\partial y} = 0$ on the boundary of $\Omega = \partial\Omega$, [46] where Eq. (2.11) is called the TV of the image I . In another study, Chambolle and Lions [76] proved that Eq. (2.11) is strictly convex and hence its minimum exists, is unique and computable. Given the TV functional Eq. (2.11), the diffusion model Eq. (2.6) can then be written as,

$$\begin{cases} \frac{\partial I(t)}{\partial t} = \text{div} [c(I) \nabla I] = \text{div} \left[\frac{\nabla I}{\|\nabla I\|_2} \right], \\ I(t=0) = J \end{cases} \quad (2.12)$$

where the DC $c(I) = \frac{1}{\|\nabla I\|_2}$ is also a decreasing function of the gradient magnitude $\|\nabla I\|_2$, similar to the DCs Eq. (2.9) or (2.10) in the PM model. The two models therefore share the same nonlinear diffusion idea; the smoothing is inhibited in the vicinity of the edges (high gradients) to preserve structures while encouraged in the background (low gradients) to remove noise.

The TV model given in Eq. (2.12) was further extended to process colour or vector-valued images by Blomgren and Chan [77] that defined an alternative semi-norm TV functional $TV_d(I) = \sqrt{\sum_{l=1}^d [E(I_l)]}$, where d is the number of colour channels and $E(I_l)$ is given by Eq. (2.11) for the l^{th} -channel image I_l . Since coupling all channels in the TV functional, the Blomgren-Chan model can avoid producing the colour-noise artifacts [10] during the diffusion process [77].

Although the TV model has been demonstrated to achieve a good balance between noise removal and edge preservation, it tends to produce staircase artifacts that divide the whole image by artificial edges [78]. This is because the pixel-level gradient

operator ∇I can either fail to detect the weak edges or misinterpret the noise as the edges, as has been demonstrated in Section 2.2.1.2 for PM model. Fig. 2.1(e) shows denoised result of the noisy image Fig. 2.1(b) by using the TV model Eq. (2.12) after 231 iterations. As seen, the TV model generates several artificial edges that are visually unpleasant and likely to result in false reorganization for the subsequent applications.

2.2.1.4 Iterated Total Variation Refinement

In the original TV model Eq. (2.12), the gradually removed noise $I - J$ during the diffusion process is treated as an error and no longer studied. In practice, since fine structures can be falsely classified as the noise by the gradient operator, they are over-smoothed during the diffusion process. Recent work has proposed to avoid this oversmoothing [22, 78] by studying the removed noise.

A. The Tadmor-Nezzar-Vese Approach

In the original TV model, the TV Eq. (2.11) was minimized only once by using the diffusion model Eq. (2.12). Tadmor, et al. [78] proposed to minimize the TV Eq. (2.11) not only once but for many times. They firstly decompose the noisy image, $J = I_0 + n_0$, by using the diffusion model Eq. (2.12). So taking the residual error n_0 contains both noise and structure information of the original image I , they decompose $n_0 = I_1 + n_1$ by the same diffusion model Eq. (2.12) except that the initial condition $I(t=0) = n_0$. Iteratively decomposing $\{n_j\}_{j=0,1,\dots,k}$ one can obtain $J = I_0 + I_1 + \dots + I_k + n_k$. Finally, the denoised estimation \hat{I} was given by $\hat{I} = \sum_{l=0}^k I_l$. This strategy is in some sense close to the matching pursuit methods [79], which can be seen as a multi-layer decomposition of the noisy observation J in an intermediate scale of spaces between those of bounded-variation [80] and ℓ^2 . Some theoretical results on the convergence of this expansion were also presented in [78].

B. The Osher-et al. approach

Another iterative TV model was proposed by Osher, et al. [22] through iteratively introducing fidelity terms in the TV functional during the diffusion process as follows:

- i. Initiation. Solve the minimization problem,

$$I_1 = \arg \min_{I_1} \int_{\Omega} |\nabla I_1(x, y)| + \lambda |J(x, y) - I_1(x, y)|^2 dx dy ,$$

to obtain the decomposition $J = I_1 + n_1$.

- ii. Iterate: compute I_{k+1} as a minimizer of the modified TV functional,

$$I_{k+1} = \arg \min_{I_{k+1}} \int_{\Omega} |\nabla I_{k+1}(x, y)| + \lambda |J(x, y) + n_k(x, y) - I_{k+1}(x, y)|^2 dx dy$$

where n_k is the residual noise estimated by the first step. The correction step adds the initial estimate n_k of the noise to the noisy image J and raises the decomposition $J + n_k = I_{k+1} + n_{k+1}$.

As $k \rightarrow \infty$, Osher, et al. [22] proved that the denoised estimation I_{k+1} can approach the noise-free image I monotonically within the Bregman distance [77] associated with the BV semi-norm [77], at least within the distance $\|I_k - J\|^2 \leq \sigma^2$, where σ is the noise Std.

Both the Tadmor-Nezzar-Vese and Osher methods refine the TV diffusion process to choose the denoised result I_k . Their results have therefore more details preserved, as shown in Fig. 2.1(f - g), which smooth the hairs less and generate less artifacts, compared to the traditional TV result, Fig. 2.1(e). However, the face in the image still looks blocky since the edge is still measured by the pixel-level gradient operator ∇I .

2.2.1.5 Coherence-Enhancing Diffusion

In the above section, all the reviewed diffusion models utilize a scalar DC c to control the diffusion process and thus the diffusion is spatially isotropic. In other words, the smoothing behaviors during the diffusion process are applied to the image with the same weight in all the spatial directions. Such isotropic smoothing may be however not able to well preserve shapes of oriented structures after diffusion since the structure orientation is not taken into account. To overcome this problem, Weickert [13, 49] firstly considered an anisotropic diffusion by proposing a 2×2 matrix \mathbf{D} to replace the scalar DC c in the diffusion model as

$$\begin{cases} \frac{\partial I(t)}{\partial t} = \text{div}[\mathbf{D} \nabla I] \\ I(t=0) = J \end{cases} \quad (2.13)$$

where the matrix \mathbf{D} was symmetric and semi positive-definite and varied at different pixel positions $\mathbf{x} = [x, y]^T$ to control the diffusion strength and direction. We hence name \mathbf{D} diffusion matrix or diffusion tensor (DT). Based on singular value decomposition [72], \mathbf{D} can be rewritten in the form of

$$\mathbf{D} = [\mathbf{V}_0 \quad \mathbf{V}_1] \begin{bmatrix} \lambda_1 & 0 \\ 0 & \lambda_2 \end{bmatrix} [\mathbf{V}_0 \quad \mathbf{V}_1]^T, \quad (2.14)$$

where the vectors $\mathbf{V}_0, \mathbf{V}_1$ and the scalars λ_0, λ_1 are the eigenvectors and eigenvalues of the DT \mathbf{D} , respectively. Using Eq. (2.14), one can then design \mathbf{D} for each pixel \mathbf{x} by

selecting different eigenvectors and eigenvalues of \mathbf{D} . The vectors $\mathbf{V}_0, \mathbf{V}_1$ determine the smoothing directions during the diffusion process. To perform a good preservation of the feature geometry in the 2-D images, Weickert [13, 49] proposed to select $\mathbf{V}_0, \mathbf{V}_1$ for each pixel $\mathbf{x} = [x, y]^T$ as the eigenvectors of a smoothed structure tensor (2×2 symmetric and semi positive-definite matrix) $\mathbf{S} = G_\rho * \nabla(G_\sigma * I) [\nabla(G_\sigma * I)]^T$, denoted as θ_0, θ_1 , so the smoothing during the diffusion process is performed along the directions perpendicular and parallel to image isophotes. The eigenvalues λ_0, λ_1 are weights determining the smoothing strength along the two directions. To perform a better preserving of the feature (intensity) contrast, the smooth strength should be preferred more in the image isophote direction instead of the gradient direction. Weickert [13] proposed to choose the eigenvalues λ_0, λ_1 so that $\lambda_0 \geq \lambda_1$ holds in the form of

$$\begin{aligned} \lambda_0 &= \alpha \\ \lambda_1 &= \begin{cases} \alpha & \text{if } \kappa = 0 \\ \alpha + (1 - \alpha) \exp(-h/\kappa) & \text{else} \end{cases}, \\ \kappa &= (\mu_0 - \mu_1)^2 \end{aligned} \quad (2.15)$$

where $h > 0$ and $\alpha \in [0, 1]$ are fixed thresholds, μ_0, μ_1 are eigenvalues of the structure tensor \mathbf{S} . The $h > 0$ serves as a threshold parameter: for $\kappa \gg h$ I get $\lambda_1 \approx 1$ and $\kappa \ll h$ leads to $\lambda_1 \approx \alpha$. The idea behind the choice of Eq. (2.15) is then:

- In almost constant regions, I should have $\mu_0 \approx \mu_1 \approx 0$ and then $\kappa \rightarrow 0$ and $\lambda_1 \approx \alpha \approx \lambda_0$. The diffusion model Eq. (2.13) performs a linear isotropic smoothing.
- In the vicinity of the edges, I have $\mu_1 \neq \mu_2 \neq 0$ and $\kappa > h$, and then $\lambda_1 > \alpha > \lambda_0$. The smoothings at these regions are then anisotropic, mainly directed by the direction parallel to the image isophotes.

As a result, the coherence-enhance (CE) diffusion model Eq. (2.13) can more precisely preserve the oriented image structures after denoising, compared to the isotropic ones. In another study, Tschumperlé and Deriche [50] extended the anisotropic diffusion model Eq. (2.13) to denoise vector-value (colour) images.

However, since the smoothing strength is still derived by the pixel-level gradient operator, the CE diffusion may produce many line-like artifacts or spurious edges in the background area. Another drawback of the CE model Eq. (2.13) is its high

computational burden. In a study, Weickert, et al. [81] used the additive operator splitting (AOS) scheme to solve Eq. (2.13), which is ten times more efficient than the widely used explicit schemes. But such scheme is restricted to the special form Eq. (2.15) of the diffusion tensor \mathbf{D} .

2.2.1.6 Selective Smoothing Diffusion Model

By comparing Eq. (2.15), (2.12) and (2.9), I can find that all the smoothing strength in the previous nonlinear diffusion models are derived in a similar manner; they are all the decreasing functions of pixel-level 1st-order difference, which is not robust for edge measurement under noise contamination. Based on the PM model Eq. (2.9), Catté, et al. [12] proposed an improved nonlinear diffusion version wherein the edge is measured by the Gaussian smoothed gradient in the following equation,

$$\begin{cases} \frac{\partial I(t)}{\partial t} = \text{div} [c(|\nabla G_\sigma * I|) \nabla I] \\ I(t=0) = J \end{cases}, \quad (2.16)$$

where the DC c is in the form of

$$c(|\nabla G_\sigma * I(x, y)|) = \exp\left(-\frac{|\nabla G_\sigma * I(x, y)|^2}{h}\right), \quad (2.17)$$

h is the gradient threshold and the function $G_\sigma(x, y) = \exp(-\frac{x^2 + y^2}{2\sigma^2})$ is the 2-D Gaussian kernel with Std σ . Since the gradient is derived in the Gaussian-smoothed noisy image instead of the noisy one, it is more robust to noise. The diffusion model Eq. (2.16) can therefore generate fewer artifacts than the PM model. However, Gaussian smoothing of the noisy image can blur the image structures and significantly decrease the contrast of the structures whose sizes are smaller than the Std σ of the Gaussian smoothing function G_σ . The gradients of these structures in the smoother image can hence be rather low, giving rise to a high smoothing strength for these structures. As such, the diffusion model Eq. (2.16) is named as selective smoothing diffusion model since it can only selectively preserve structures with scales similar as that of the Gaussian kernel [12].

2.2.2 Neighborhood Filter

The neighbourhood filter (NF) suppresses the noise through a weighted averaging process in which the intensity of a pixel in the denoised image is the weighted average

of the intensities of its surrounding neighbouring pixels in the noisy image [36]. Since iterating only once to denoise, the NFs often smooth out noise less efficiently than the variational methods do.

2.2.2.1 Bilateral Filter

One of the most popular NF is bilateral filtering (BF), which was introduced by Tomasi and Manduchi [11] to estimate the weights by the distances of the spatial positions and the intensities between the central pixel and its surrounding neighborhood pixels in the following form,

$$I(x, y) = \frac{\sum_{k=-W}^W \sum_{l=-W}^W c(x, y, k, l) J(x+k, y+l)}{\sum_{k=-W}^W \sum_{l=-W}^W c(x, y, k, l)}, \quad (2.18)$$

where

$$c(x, y, k, l) = \exp\left(-\frac{(J(x, y) - J(k, l))^2}{h^2} - \frac{(x-k)^2 + (y-l)^2}{K^2}\right) \quad (2.19)$$

denotes the weight of the neighbouring pixel $(x+k, y+l)$, W denotes the half width of the searching window and K is the thresholding parameter of the spatial distance. The weight $c(x, y, k, l)$ given in Eq. (2.19) both utilized the difference of two pixels in gray-value domain and spatial domain. As such, similar pixels in the neighborhood contribute more in the weighted averaging to remove the noise contained in the central pixel, so avoiding smoothing across edges. BF is therefore a nonlinear edge-preserving filter. However, being a NF, the BF performs smoothing only once, so the noise may not be removed effectively. Fig. 2.1(h) shows the denoised result of the noisy one Fig. 2.1(b) by the BF. As seen by comparing Fig. 2.1(h) with Fig. 2.1(d-g), the BF cannot smooth out all noise on the face of the girl in the noisy image, compared to the variational methods.

The traditional BF does not take into account the spatial orientation of the features in the image. Takeda, et al. [17] incorporate the direction of the pixel position (k, l) into the weight $c(x, y, k, l)$, which was called steering NF by taking robust estimation of the local gradients into account to measure the similarity between two pixels, is given by

$$c(x, y, k, l) = \exp\left(-\frac{(J(x, y) - J(k, l))^2}{h^2} - \frac{[x-k, y-l] \mathbf{S}(\nabla(G_\sigma * J)) [x-k, y-l]^T}{K^2}\right), \quad (2.20)$$

where the 2×2 diagonal matrix $\mathbf{S}(\nabla(G_\sigma * \mathbf{J}))$ is the structure tensor defined in Section 2.2.1.5. In the background regions where $\mathbf{S}(\nabla(G_\sigma * \mathbf{J}))$ is unitary, Eq. (2.20) is simplified as the BF Eq. (2.19). However, in the vicinity of edges where $\mathbf{S}(\nabla(G_\sigma * \mathbf{J}))$ is no longer unitary, the local gradient direction information contained in the structure tensor $\mathbf{S}(\nabla(G_\sigma * \mathbf{J}))$ adaptively “steer” the local weights (kernel) $c(x, y, k, l)$, resulting in rotated, elongated or elliptical shapes spread along the directions of the local edge structure. With these locally adapted kernels, the steering NF can result in better preservation of details than BF does. However, both BFs Eq. (2.19) and (2.20) calculate the similarity of the two pixel (x, y) and (k, l) by using only the 1st-order difference of the two pixel intensities in the noisy image \mathbf{J} , in a similar manner as the variational methods Eq. (2.15), (2.12) and (2.9) that detects edges by using the pixel-level gradient. Thus the BFs still cannot achieve a good balance between noise removal and feature preservation.

2.2.2.2 Nonlocal-Means Filter

Nonlocal-Means (NLM) filter was proposed simultaneously by Awtate and Whitaker [14] and Buades, et al. [15] in 2005. In general, the intensity difference $I(x, y) - I(k, l)$ of the two pixels in the noise-free image I is unknown and can only be estimated from the noisy observation J . In the BF filter Eq. (2.19), the difference is measured by the pixel-level intensity difference $J(x, y) - J(k, l)$ in the noisy observation J . The NLM filter improved the estimation of the unknown difference, $I(x, y) - I(k, l)$, by a novel Euclidean distance between intensities of several pixels within two regions centred respectively at (x, y) and (k, l) in the observation, J . Belonging to the NF, NLM algorithm estimates the denoised intensity $I(x, y)$ of the pixel $\mathbf{x} = [x, y]^T$ as a weighted average of the intensities of all image pixels whose surrounding regions look like that of \mathbf{x} in the form of

$$I(x, y) = \frac{1}{m(x, y)} \sum_{k=-H_I}^{H_I} \sum_{l=-W_I}^{W_I} \exp\left(-\frac{d_\sigma(I(x, y), I(x+k, y+l))}{h^2}\right) J(x+k, y+l), \quad (2.21)$$

where $m(x) = \sum_{k=-H_I}^{H_I} \sum_{l=-W_I}^{W_I} \exp\left(-\frac{d_\sigma(I(x, y), I(x+k, y+l))}{h^2}\right)$ is the normalizing factor, H_I

and W_I denotes respectively the half height and width of the image \mathbf{I} , h denotes the

weights threshold. The distance $d_\sigma(I(x, y), I(x + k, y + l))$ in Eq. (2.21) denotes the intensity difference of the two pixel (x, y) and $(x + k, y + l)$ in the unknown noise-free image I and is given by the intensity differences between several neighbouring pixels around the two pixels as [53],

$$d_\sigma(I(x, y), I(x + k, y + l)) = \sum_{m=-W_N}^{W_N} \sum_{n=-W_N}^{W_N} G_\sigma(m, n) (J(x + m, y + n) - J(x + k + m, y + l + n))^2, \quad (2.22)$$

where G_σ is a Gaussian function with Std σ , W_N is the half width of the neighborhood window. The difference of the two pixels is thus not pixel-level but patch-level between two patches, each of which contains noisy intensities of several neighbouring pixels. The difference Eq. (2.22) is robust against noise contamination due to Gaussian weighted averaging. It is also more likely to preserve finer edges than the Catté *et al.* method Eq. (2.16) does since the Gaussian smoothing in the Eq. (2.22) is not applied directly on the image but on the square of the image differences.

The standard NLM algorithm is computationally expensive. In another study, Buades, et al. [82] proposed to limit the search region within which similar neighborhoods are looked for. As such, the NLM filter can be also seen as a neighbourhood filter. Other researchers further proposed to accelerate the NLM filter by many strategies, such as a pre-selection of the contributing neighborhoods based on average value and gradient [83], mean values and variance [84] or higher-order statistical moments [85], and principal component analysis [55]. Also the calculation of the difference between different neighbourhoods Eq. (2.22) can be optimized using the fast Fourier transform [86] or a moving average filter [87].

The NLM filter was also applied in the spatial-time domain for denoising video [88], fluorescence microscopy image sequences [56], 2-D [35] and 3-D medical images [84]. The selection of the parameters in the NLM filter was also discussed in many studies. In the ref. [88], the weight threshold h in Eq. (2.21) was pre-set between $0.75\sigma_n$ and σ_n , where σ_n is the noise Std. In another study [89], the threshold h was determined by the median average deviation of the nonlocal distances of the whole image. In a recent study, Van De Ville and Kocher [90] proposed to optimize the parameters in the NLM filter based on the Stein's unbiased-risk-estimate (SURE) criteria [91] and achieved an apparent denoising improvement over the NLM filter with other parameter selection methods.

2.2.2.3 Iterative Versions of the Nonlocal Means Filter

The NLM filter Eq. (2.21) performs local smoothing only once on the whole image for noise removal and thus may not be able to remove the whole noise contained in the noisy image. Based on the traditional NLM filter, Kindermann, et al. [92] proposed a NLM functional,

$$E_{BCM}(\mathbf{I}) = \int_{\Omega \times \Omega} \left(1 - \exp\left(-\frac{d_{\sigma}(\mathbf{I}(x, y), \mathbf{I}(k, l))}{h^2}\right) \right) \exp\left(-\frac{(x-k)^2 + (y-l)^2}{K^2}\right) dx dy dk dl, \quad (2.23)$$

where $d_{\sigma}(\mathbf{I}(x, y), \mathbf{I}(k, l))$ is the nonlocal difference given in Eq. (2.22). By minimizing the above functional to restore the noise-free image \mathbf{I} , I can then obtain an iterative NLM filter that iteratively remove the noise from the noisy observation \mathbf{J} . However, a major problem for minimizing Eq. (2.23) is that the functional is non-convex and its global minimum is thus hardly achieved.

Another iterative NLM algorithm was introduced by Gilboa and Osher [93] who proposed to minimize the functional

$$E(\mathbf{I}) = \frac{1}{4} \int_{\Omega \times \Omega} (\mathbf{I}(x, y) - \mathbf{I}(k, l))^2 w_J(x, y, k, l) dx dy dk dl, \quad (2.24)$$

where the weight function w_J is only related to the noisy observation \mathbf{J} and given by $w_J(x, y, k, l) = \exp\left(-\frac{d_{\sigma}(\mathbf{J}(x, y), \mathbf{J}(k, l))}{h^2}\right)$. As such, the weight w_J during the whole diffusion iteration process remains unchanged. This is in contrast to the iterative scheme of Kindermann, et al. [92] for minimizing Eq. (2.23), where the weights are gradually updated at each iteration step based on the previous denoised result. By using the calculus of variations to minimize the functional Eq. (2.24), I can obtain the following iterative equations,

$$\begin{cases} \mathbf{I}(x, y, t) = -\int_{N_{x, y}} (\mathbf{I}(x, y, t-1) - \mathbf{I}(k, l, t-1)) w_J(x, y, k, l) dk dl \\ \mathbf{I}(t=0) = \mathbf{J} \end{cases}, \quad (2.25)$$

where $N_{x, y}$ is the set of the neighbouring region around the pixel (x, y) . To ensure properties such as preservation of the average image intensity and convergence of the whole iteration process, the weights $w_J(x, y, k, l)$ in Eq. (2.25) are adaptively chosen in two ways [93]; (i) In a neighbouring region $N_{x, y}$, only the 5 largest weights as well as those for the four spatial neighbors of each pixel (x, y) are kept and all other weights are set to 0; (ii) in case that $w_J(x, y, k, l) = 0$ and $w_J(k, l, x, y) \neq 0$, $w_{I0}(x, y, k, l)$ is set to $w_{I0}(k, l, x, y)$.

$l, x, y) \neq 0$. The first choice (i) ensures irreducibility of the PDE Eq. (2.25) and therefore the solution of the PDE can converge to a trivial steady state [93]. The second condition (ii) ensures that the iteration process is conservative [93], i.e., the mean intensity of the whole image is preserved. Extensions of Eq. (2.25) were presented in the studies [94] and [95]. The first replaced the ℓ^2 norm in Eq. (2.24) by other norms, such as $|\mathbf{I}(x, y) - \mathbf{I}(k, l)|$, resulting in a better edge preservation. The second study proposed extensions such as iteratively selecting size of the searching region and how to deal optimally with colour images.

Another NLM-based variational method was suggested in [54], in which the functional $E(\mathbf{I})$ aimed to minimize the difference between the original image and the filtered image in the following form,

$$E(\mathbf{I}) = \int_{\Omega} \left(\mathbf{I}(x, y) - \frac{\int_{N_{x,y}} w_I(x, y, k, l) \mathbf{J}(k, l) dk dl}{\int_{N_{x,y}} w_I(x, y, k, l) dk dl} \right)^2 dx dy, \quad (2.26)$$

where the nonlocal weight w_I is given by $w_I(x, y, k, l) = \exp\left(-\frac{d_{\sigma}(\mathbf{I}(x, y), \mathbf{I}(k, l))}{h^2}\right)$.

To minimize the functional Eq. (2.26), I compute its Euler-Lagrange equation and obtain the simplified iteration equation,

$$\mathbf{I}(x, y, t+1) = \mathbf{I}(x, y, t) - \Delta t \left(\mathbf{I}(x, y, t) - \frac{\int_{N_{x,y}} w_I(x, y, k, l) \mathbf{J}(k, l) dk dl}{\int_{N_{x,y}} w_I(x, y, k, l) dk dl} \right) \quad (2.27)$$

with $\mathbf{I}(t=0) = \mathbf{J}$, where Δt is the step size. According to Eq. (2.27), the smoothing weights can be estimated more accurately from the already denoised image $\mathbf{I}(t)$ than directly from the noisy one \mathbf{J} . Moreover, since the weighted smoothing behaviours are always applied to the noisy image \mathbf{J} during the iteration process, the over-smoothing can be in some sense inhibited, thus providing a better balance between noise removal and feature preservation, compared to the traditional NLM filter Eq. (2.21). However, such method is still not able to efficiently remove all the noise contained in the image. So far, the best iterative NLM filter is perhaps the one proposed by Kervrann and Boulanger [16, 89], which adaptively and iteratively revise the size of the search window for each pixel at each iteration step based on the local structures of the images. Their iterative NLM is therefore named as structure adaptive filter (SAFIR) and leads to considerable improvement in denoising performance of the NLM filter.

2.3 Transform-Domain Denoising Methods

The methods reviewed above use directly the intensities of pixels in the spatial domain of the images. In this section I review another type of denoising methods, transform-domain denoising where the pixel intensity is transformed into new spaces to separate noise-free image and noise components. Since this thesis focus mainly on the variational method, I here provide only a brief review of transform-domain method. For more details about this approach, I refer the interested reader to [36, 79, 96, 97].

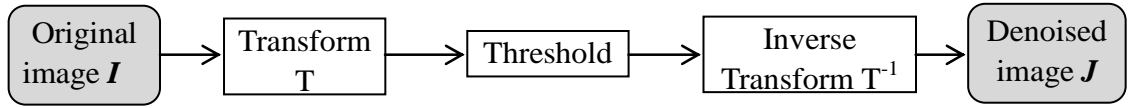


Fig. 2.2 Principal operations in shrinkage-based denoising methods [98]

The basic principle behind most transform-domain denoising methods is shrinkage - truncation (hard thresholding) or scaling (soft thresholding) of the transform coefficients to suppress the effects of noise, as shown in Fig. 2.2. For such thresholding, the challenge is to develop a suitable coefficient-mapping operation that does not sacrifice the details in the image. The final denoised image is obtained by performing an inverse transform on the shrunk coefficients. Apart from the choice of the thresholding operator, the choice of the transform domain is also critical. In the image processing literature, a variety of such transform domains or bases have been proposed. Examples of such bases include 2-D extensions of the well-studied discrete cosine (DCT) bases used in [58], as well as those developed specifically for image modeling purposes, namely curvelets [59], ridgelets [60], contourlets [61], etc. Of the many transform bases used in literature, the space-frequency localization property of the wavelet domain makes it the most popular choice.

Since the seminal work by Donoho and Johnstone [62], the wavelet basis has been at the core of many transform-domain denoising methods [63-66]. Of these, the denoising method proposed by Portilla, et al. [67] has shown considerable promise. There the authors proposed a denoising approach based on the scale mixture of a Gaussians (GSM) model for the wavelet coefficients [68]. The noisy image is first broken into multiple sub-bands in the wavelet domain, and in each sub-band the wavelet coefficients within a local neighborhood are modeled as a Gaussian scale mixture [69],

where the scale indicates the standard deviation of the Gaussian function. A Wiener filter is then used to denoise the wavelet coefficients in a Bayesian least-squares framework. The denoised coefficients across sub-bands are then inversely transformed to form the final denoised image. Recently, Lyu and Simoncelli [70] extended this local framework by incorporating a global model for natural images using Gaussian Markov random field (MRF) to form a Field of GSMs (FoGSM). Such a global model was shown to improve upon the performance of the BLS-GSM method of [67].

The Wiener filter forms the basis of another celebrated denoising method proposed by Dabov, et al. [58]. There the authors proposed BM3D - a two-step denoising method which exploits both spatial and frequency information of an image. The first step involves a shrinkage-based-transform-domain operation. The transform domain of choice for strong noise was the DCT basis, although the wavelet basis was recently shown to improve performance somewhat [99]. The initial denoised image is then used as a guide or pilot estimate of the ground-truth \mathbf{I} for a Wiener filtering operation. What makes this approach unique is that in each step it exploits patch redundancy within the image to improve performance. This is done by first identifying intensity-similar patches in the image spatial domain. This group is then used to perform an adaptive thresholding in the shrinkage step. This allows them to process the entire group of patches simultaneously. A similar grouping on the pilot estimate is used to perform a transform-domain Wiener filtering. Use of a group of patches to adaptively estimate the threshold and parameters of the Wiener filter lends robustness to the process in presence of strong noise. As such, this hybrid approach can be seen as the start-of-art denoising methods at present [] [].

Although performing denoising in the transform domain, many of the so-called transform-domain denoising methods in fact have equivalent spatial-domain interpretations. A thorough analysis showing such equivalence for a more general class of shrinkage-based estimators was presented in [98]. More recently, Milanfar [36] also cast the hybrid approach of BM3D in a spatial-domain weighted averaging framework. Consequently, various denoising methods may be distinct preferably based on how a specific filter is implemented rather than on the domain of denoising.

2.4 Summary

In this chapter, I have reviewed in detail most of the popular spatial-domain denoising methods; from linear to nonlinear, isotropic to anisotropic, and pixel-level

local to patch-level nonlocal approaches. All of these methods aim to restore an image by achieving a good balance between noise removal and feature preserving. Since the edge is a fundamental feature, all these popular methods are designed by using the 1st-order difference of the image intensities to derive the smoothing strengths based on the edge-preservation concept; more complicated features or structures can be preserved as long as edges are preserved. Some of these methods have achieved an impressive denoising performance, as shown in Fig. 2.1. Besides, II have also briefly reviewed another popular denoising approach, transform-domain approach, and pointed out that most of the transform-domain-based methods can in fact have their equivalent variational interpretation in the image spatial domain.

However, the edge-preserving denoising approach has also their limits. In the next chapter of Part I in this thesis, II point out that the edge-preserving denoising approach has their limits in preserving complex structures and textures, particularly under the severe noise contamination. I discuss such limitations and proposed new denoising methods for denoising images containing blobs and ridges, such as live-cell images. In Chapter 4, II extend our method in Chapter 3 to propose a more generalized diffusion method for denoising natural images containing multiple types of features.

Chapter 3

A Feature-Preserving Nonlinear Anisotropic Diffusion for Denoising Images Containing Blobs and Ridges

Abstract: In this chapter, I present a new diffusion method for denoising low SNR images containing blob and ridge features. In general, blobs and ridges underlie many important features in biological, biometric and remote-sensing images. Objects in these images are likely to be corrupted by noise, such as live cells in fluorescent biological images, ridges and valleys in fingerprints and moving targets in synthetic aperture radar and infrared images. A commonly used denoising method makes use of edge information in an image to achieve a good balance between noise removal and feature preserving. However, if edges are partly lost to a certain extent or contaminated severely by noise, such an approach may not be able to preserve these features, leading to loss of important information. To overcome this problem, I propose a novel second-order nonlocal difference as a robust blob and ridge detector and incorporate it into a diffusion process to form a novel feature-preserving nonlinear anisotropic diffusion model. Experiments show that the new diffusion filter outperforms many popular filters for preserving blobs and ridges, reducing noise and minimizing artifacts.

3.1 Introduction

As reviewed in Chapter 2, image denoising has been a long-studied subject in image processing which tries to restore an original noise-free image from the noisy observation for improved visual quality and for subsequent processing tasks such as image segmentation, feature extraction and image analysis. There now exist many

denoising approaches, ranging from linear [42-45] and nonlinear diffusion model [9, 12, 46-48], tensor-driven diffusion model [13, 49-52], neighborhood filters [11, 16, 53-56], to transform-domain denoising [57-60, 62-68, 70, 98], all of which aim to optimally remove noise by minimizing the mean square error (MSE) between the original and denoised images. Prior knowledge of key features in the image is usually taken into account in the minimization process of MSE, directly or indirectly, in order to achieve a good balance between noise removal and feature preserving in denoised images.

Nonlinear diffusion is a popular denoising approach in which prior information of image features can be incorporated via the diffusion coefficient c (DC) into the filtering processing. In general, an edge is a fundamental feature that underlies more complicated features or structures in an image. The latter can be preserved as long as edges are preserved after denoising. Since the edge can be characterised by a 1st-order difference (gradient), Perona and Malik [9] first used the gradient as an edge detector to derive the DC that can reject diffusion at edges and permit smoothing in other places. Weickert [13] further took into account the orientation of edges and developed a tensor-driven diffusion model in which smoothing is further discouraged along the directions perpendicular to the edge orientations. Building on the work of Weickert [13], researchers have developed various tensor-driven diffusion models [13, 50-52]. In particular, Tschumperlé and Brun [51] proposed a method for anisotropic image smoothing by developing a new high-dimensional structure tensor field. The method has shown impressive denoising performances both visually and quantitatively on nature images [100], as reviewed in the previous chapter.

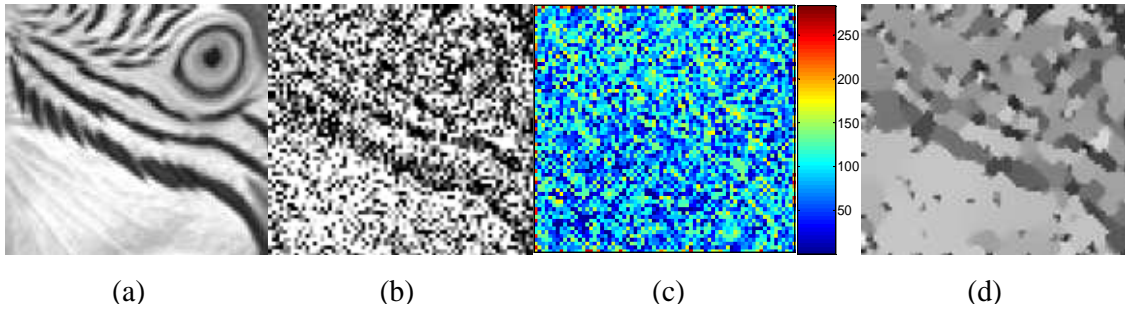


Fig. 3.1 (a) – (b) Noise-free and noisy fragments of an 8-bit image *Parrot* [101], the latter of which contains additive Gaussian white noise of a Std $\sigma_n = 20$; (c) Gradient amplitude of the noisy image calculated by the 1st-order central difference(b); (d) Denoising result by PM diffusion [9] on (b)

While there has been a considerable focus on the methods of anisotropic diffusion, the smoothing strengths, either DCs, eigenvalues of diffusion tensor or the averaging weights of the neighbourhood filter for determining where and how much smoothing effect should be encouraged or discouraged, are all derived using the grayscale gradient information, which effectively corresponds to edge detection. However, in low-contrast and/or low-SNR images, the gradient is not robust to characterize the features contained in noise-free images. Fig. 3.1(a-b) shows noise-free and noisy fragments of the image *Parrot* [101]. Fig. 3.1(c) shows the gradient amplitude of the noisy image Fig. 3.1(b) by using a simple 1st-order central difference. The colour bar in this figure indicates the scale of the gradient amplitude: a red colour means a high value of gradient amplitude. As seen by comparing Fig. 3.1(a) and (c), I can find that almost no features (the eye, eye socket and stripes on the face of the parrot) can be characterized in the gradient map. Although one can perform a smoothing to remove noise before calculating the gradient, the edges in the image can be also blurred or smoothed out. As such, when the edges are partly lost to a certain extent or are contaminated severely by noise, the gradient-based denoising methods, one of which is shown in Fig. 3.1(d), may not be able to recover these edges and thus fails to preserve other common features that are made of by the edges, such as blobs, ridges and textures, which are important in the study of many subjects, such as live-cell imaging [31], detection and tracking of small moving targets [102], and recovery of ridges for pattern recognition of fingerprints. This calls for a more sophisticated feature detector than the edge detector in the diffusion-based denoising methods.

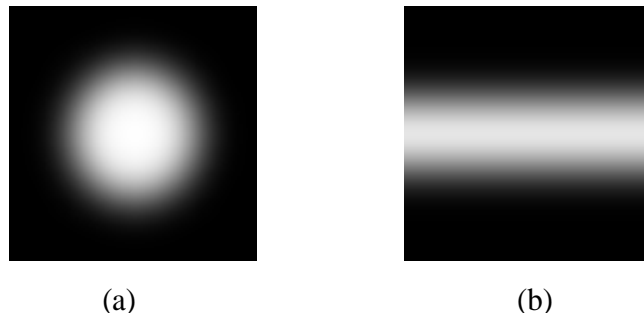


Fig. 3.2 An example of blob and ridge feature. (a) A bright blob; (b) A bright horizontal ridge

Blobs and ridges correspond respectively to circular and line-like regions that are either brighter or darker than their surroundings [104, 105]. Fig. 3.2(a) and (b) show a

bright blob and ridge. Mathematically, these features are more correlated to a second-order difference rather than a first-order one which measures edges. In this chapter I propose a novel second-order nonlocal difference (2^{nd} -order NLD) to detect blob and ridge features. By nonlocal difference I mean that the grayscale difference between two pixels is measured by two regions (patches) centred at the pixels instead of the pixels themselves. Each patch can be considered as a vector in a multidimensional feature space [51], so the proposed 2^{nd} -order NLD measures the second-order difference involving more than two vectors. The use of such nonlocal differences is inspired by the success of the popular NLM filter [53], in which the difference of two pixels is measured by the Euclidean distance of the grayscale values between two patches that are centred at these pixels. Such distance measurement has been used as a basis not only for image denoising [16, 51, 57, 58] reviewed in the previous chapter, but also for other machine vision tasks such as texture synthesis [106] and texture segmentation [107]. We further propose to form a new feature-preserving denoising method by incorporating the proposed 2^{nd} -order NLD in a nonlinear anisotropic diffusion model. Owing to a good performance of 2^{nd} -order NLD as a blob and ridge detector, our denoising method can preserve these features even though the edges that bound the blobs and ridges are partly lost or contaminated by severe noise. Experimental results demonstrate that our method can achieve a higher peak-signal-to-noise ratio (PSNR) [16] and higher mean similarity index (MSSIM) [108] when applied to both synthetic and real live-cell, fingerprint and natural images that contain blobs and ridges with various sizes, compared to traditional diffusion methods [9, 12], tensor-driven diffusion methods [13, 51, 52] and other popular denoising methods [16, 53, 58].

The remainder of this chapter is organized as follows. We first present the 2^{nd} -order NLD in Section 3.2. In Section 3.3, the 2^{nd} -order NLD is employed to form a feature-preserving nonlinear diffusion method. Experiments on both synthetic and real data are presented in Section 3.4. Finally, I conclude the main results of the paper in Section 3.5.

3.2 Second-order Nonlocal Difference

A simplest way to detect blobs and ridges is to apply the Laplacian operator [109] which, for one-dimensional (1-D) digital images, is usually approximated by a second-order difference of signal intensities of three adjacent pixels. However, noise in these images can lead to false detections because the pixel-level difference, as shown for the gradient image in Fig. 3.1(c), is prone to be corrupted by noise. We here introduce the concept of nonlocal difference which measures the dissimilarity between two local

regions, referred to as patches, rather than two pixels. The nonlocal difference between two patches was first introduced for textures synthesis by Efros and Leung [106] and then for image denoising in the work of NLM filter by Buades, et al. [53]. In this section, I apply the concept to develop a second-order nonlocal difference for robust detections of blobs and ridges. The difference will then be incorporated into a diffusion model for feature-preserved denoising.

3.2.1 Nonlocal Difference

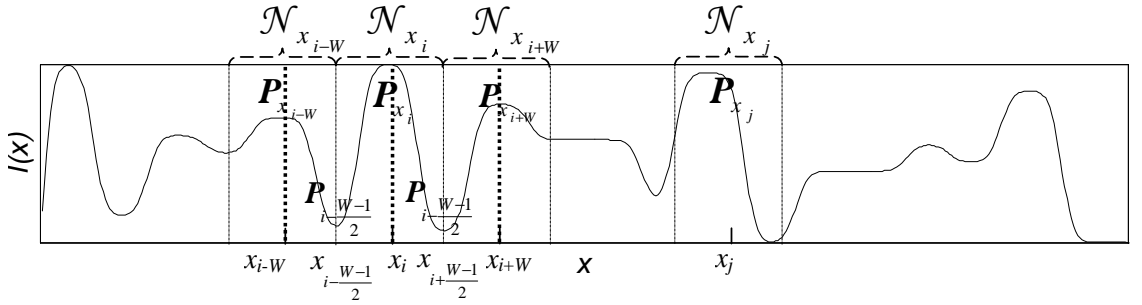


Fig. 3.3. A schematic showing nonlocal differences in one-dimensional space

We describe the concept of nonlocal difference in a 1-D signal. Extension to the 2-D case is straightforward and will be discussed later. Let $I : \Omega \subset \mathbb{R}^1 \rightarrow \mathbb{R}^1$ be a 1-D signal defined on the signal domain Ω and $x_i \in \Omega$ is the pixel position, $x_i = x_1, x_2, \dots, x_N$, as shown in Fig. 3.3. For each pixel, x_i , I define a neighbourhood region \mathcal{N}_{x_i} which comprises W pixels centred around x_i . We further define a patch \mathbf{P}_{x_i} , which is a vector comprising gray-level values of all pixels within the neighbourhood region \mathcal{N}_{x_i} [51]

$$\mathbf{P}_{x_i} = [I(x_{i-(W-1)/2}), I(x_{i-(W-1)/2+1}), \dots, I(x_i), \dots, I(x_{i+(W-1)/2})]^T, \quad (3.1)$$

where W is assumed to be an odd number for symmetry consideration. The nonlocal distance between two signal values, $I(x_i)$ and $I(x_j)$, can be measured as the Gaussian-weighted Euclidean difference [53],

$$\begin{aligned} d_{\text{NL}}(x_i, x_j) &= \left\| \mathbf{P}_{x_i} - \mathbf{P}_{x_j} \right\|_{2, \sigma} \\ &= \left[\frac{1}{C} \sum_{k=-(W-1)/2}^{(W-1)/2} G_{\sigma}(k) |I(x_{i+k}) - I(x_{j+k})|^2 \right]^{1/2} \end{aligned} \quad (3.2)$$

of the two vectors \mathbf{P}_{x_i} and \mathbf{P}_{x_j} in the W -dimensional space, where G_σ is a Gaussian kernel with Std σ and $C = \sum_{k=-(W-1)/2}^{(W-1)/2} G_\sigma(k)$ is the normalizing factor. The Std σ is often chosen as $1/3$ of the half of the patch width. For an image J that is the noisy observation of the image I , this nonlocal distance has been proven to provide a more reliable estimation for the unknown absolute intensity difference $|I(x_i) - I(x_j)|$, compared to estimation by using only the noisy samples $J(x_i)$ and $J(x_j)$ [97]. The distance Eq. (3.2) has also been used in the NLM filter for improving denoising performance of the traditional weighted averaging filter [14, 15, 53].

Based on the nonlocal distance, Eq. (3.2), and patch expression, Eq. (3.1), I can define a first-order nonlocal difference (1st-order NLD) when two patches, centred at x_i and $x_{i+(W+1)/2}$, are very close to each other,

$$\begin{aligned} \|\nabla_{\text{NL}} \mathbf{I}(x_i)\| &= \left\| \mathbf{P}_{x_{i-(W+1)/2}} - \mathbf{P}_{x_{i+(W+1)/2}} \right\|_{2,\sigma} \\ &= \left(\frac{1}{C} \sum_{k=-(W-1)/2}^{(W-1)/2} G_\sigma(k) \left(\mathbf{I}(x_{i-(W+1)/2+k}) - \mathbf{I}(x_{i+(W+1)/2-k}) \right)^2 \right)^{1/2}, \end{aligned} \quad (3.3)$$

where G_σ is a Gaussian kernel with Std σ . Eq. (3.3) involves the first-order difference between two adjacent patches $\mathbf{P}_{x_{i-(W+1)/2}}$ and $\mathbf{P}_{x_{i+(W+1)/2}}$. For the same reason given to Eq. (3.2), Eq. (3.3) is more reliable than the pixel-level gradient operator involving two pixels to measure edges under noise contamination.

One drawback of the nonlocal distance is its increased computational burden. To overcome this problem, an alternative solution [95] is to first transform the vector \mathbf{P}_{x_i} to another vector $\mathbf{F}_{x_i} = [\mathbf{F}_{x_i}(0), \dots, \mathbf{F}_{x_i}(W-1)]^T$ with an orthonormal transforming matrix \mathbf{A} derived by the principal components analysis (PCA). A simplified nonlocal distance $d_{\text{NLS}}(x_i, x_j)$ can then be measured by either all or parts of the components of the new vector \mathbf{F}_{x_i} . When all components of \mathbf{F}_{x_i} are considered, the simplified nonlocal distance is equivalent to Eq. (3.2) since $d_{\text{NLS}}(x_i, x_j) = \left\| \mathbf{F}_{x_i} - \mathbf{F}_{x_j} \right\|_{2,\sigma} = \left\| \mathbf{A}\mathbf{P}_{x_i} - \mathbf{A}\mathbf{P}_{x_j} \right\|_{2,\sigma} = \left\| \mathbf{P}_{x_i} - \mathbf{P}_{x_j} \right\|_{2,\sigma}$ [55]. In particular, when only the component $\mathbf{F}_{x_i}(0)$ of the vector \mathbf{F}_{x_i} is used, the simplified nonlocal distance $d_{\text{NLS}}(x_i, x_j)$ is given by

$$d_{\text{NLS}}(x_i, x_j) = \frac{G_\sigma(0) \left| \mathbf{F}_{x_i}(0) - \mathbf{F}_{x_j}(0) \right|}{C^{1/2}} = \frac{\left| \mathbf{F}_{x_i}(0) - \mathbf{F}_{x_j}(0) \right|}{C^{1/2}}, \quad (3.4)$$

which is simply the difference of two scalars divided by a constant. According the theory of PCA [55], the first component $\mathbf{F}_{x_i}(0)$ of \mathbf{F}_{x_i} , which is also the first principal component of the patch \mathbf{P}_{x_i} , can be seen as a mean value of the patch \mathbf{P}_{x_i} . As such, the edge detector $|\nabla(G_\sigma * I)(x_i)|$ that was introduced in Eq. (2.16) by Catté, et al. [12] can indeed be seen as a simplified case of the 1st-order NLD Eq. (3.3) since the edge detector in the discrete form

$$\begin{aligned} |\nabla(G_\sigma * I)(x_i)| &= \left| \sum_{k=-W}^W k G_\sigma(k) I(x_{i+k}) \right| \\ &= W \left| \sum_{k=-\frac{W-1}{2}}^{\frac{W-1}{2}} G_\sigma(k - (W+1)/2) I(x_{i+k-(W+1)/2}) \right. \\ &\quad \left. - \sum_{k=-\frac{W-1}{2}}^{\frac{W-1}{2}} G_\sigma(k - (W+1)/2) I(x_{i-k+(W+1)/2}) \right| \end{aligned} \quad (3.5)$$

also measures the difference between the Gaussian-weighted mean values of the two patches (vectors). In a recent study, Tasdizen [55] has shown that the PSNR obtained by a variation of NLM filter whose nonlocal differences are measured by the first principle components of the patches, i.e., in the similar fashion to Eq. (3.5), is much lower than that by the original NLM filter which uses Eq. (3.2) for the distance measurement. As such, using the full components of the patches for edge detection should perform better than that given by Eq. (3.5) that uses only the mean values of the patches.

3.2.2 Second-order Nonlocal Difference

Based on the definition of nonlocal difference in the last section, I now formulate a second-order nonlocal difference (2nd-order NLD) to be used for blob and ridge detection in the form of

$$\begin{aligned} \|\nabla_{\text{NL}}^2 \mathbf{I}(x_i)\|_{2,\sigma} &= \|2\mathbf{P}_{x_i} - \mathbf{P}_{x_{i-W}} - \mathbf{P}_{x_{i+W}}\|_{2,\sigma} \\ &= \left(\frac{1}{C} \sum_{k=-(W-1)/2}^{(W-1)/2} G_\sigma(k) (2\mathbf{I}(x_{i+k}) - \mathbf{I}(x_{i-W+k}) - \mathbf{I}(x_{i+W+k}))^2 \right)^{1/2}, \end{aligned} \quad (3.6)$$

where G_σ and C are the same as those in Eq. (3.2). Eq. (3.6) involves the second-order difference between a central patch \mathbf{P}_{x_i} and its two adjacent patches $\mathbf{P}_{x_{i-W}}$ and $\mathbf{P}_{x_{i+W}}$ shown in Fig. 3.3. A large $\|\nabla_{\text{NL}}^2 \mathbf{I}(x_i)\|_{2,\sigma}$ corresponds to a brighter (darker) central patch compared with its two neighbours, which indicates the presence of a blob or ridge. For a

similar reason as for Eq. (3.2) in the last section, Eq. (3.6) can provide a more reliable measurement than the pixel-level second-order difference, i.e. the Laplacian operator, for blob and ridge detection in the presence of noise.

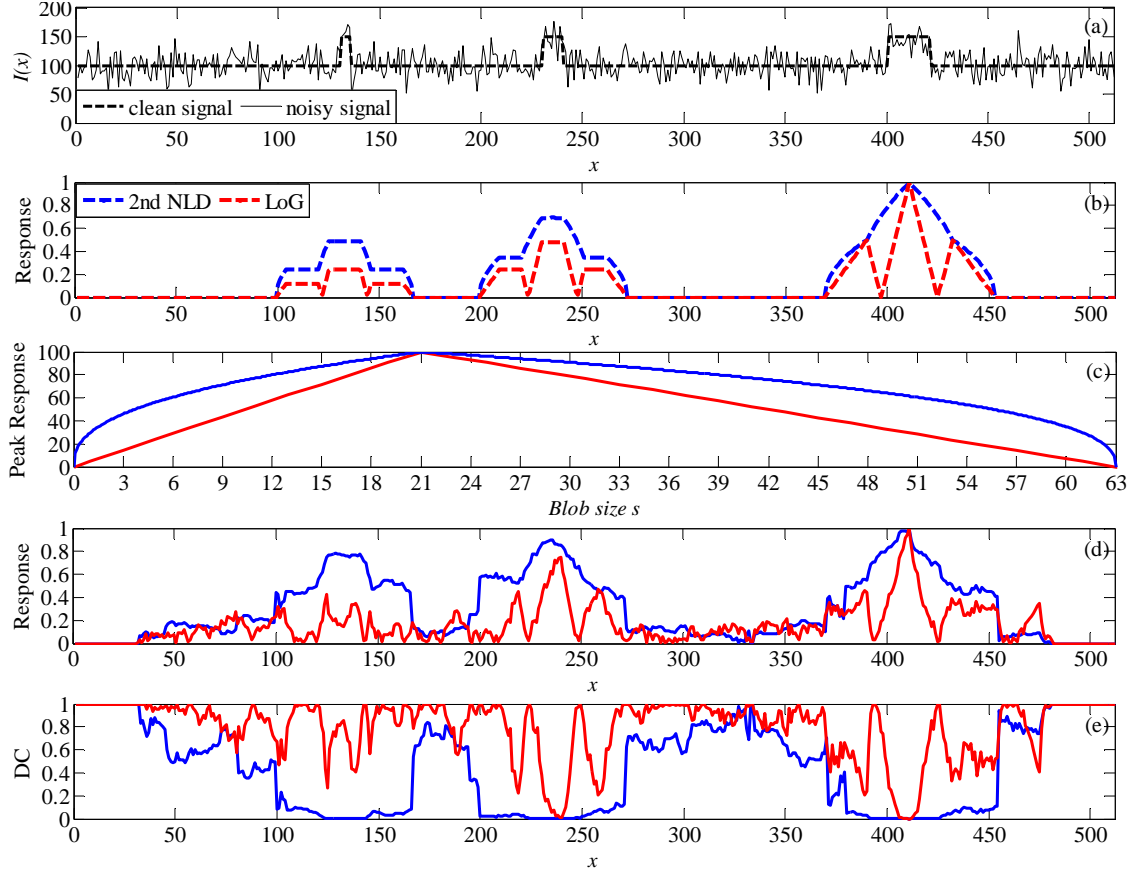


Fig. 3.4. (a) A 1-D noise-free signal containing three blobs and the corresponding signal corrupted by additive white Gaussian noise with a Std $\sigma_n = 20$; (b) The 2nd-order NLD and LoG response of the noise-free signal; (c) The peak response of the 2nd-order NLD for a blob at the blob centre versus the blob size s ; (d) The 2nd-order NLD and LoG response of the noisy signal; (e) The diffusion coefficient of 2nd-order NLD and LoG response on the noisy signal.

In order to illustrate the performance of 2nd-order NLD as a blob detector in the 1-D case, I study the behaviour of $\|\nabla_{NL}^2 \mathbf{I}(x_i)\|_{2,\sigma}$ on a 1-D 8-bit signal containing three blobs of size $s = 5, 11$ and 21 pixels without and with additive white Gaussian noise (AWGN) of a Std $\sigma_n = 20$, as shown in Fig. 3.4(a). Intensities of the blobs and backgrounds are set to be 150 and 100 respectively. The response of the 2nd-order NLD given by Eq. (3.6) on the noise-free image is plotted in Fig. 3.4(b), where the patch size

$W = 21$ is chosen, which corresponds to the largest blob size in the signal. The Std σ of the Gaussian function in Eq. (3.6) is set as $\sigma = (W - 1) / 6 = 10 / 3$, which is 1/3 of the half of the patch window [109]. As shown in Fig. 3.4(b), when the blob size equals the patch size, i.e., $s = W$ (rightmost blob in Fig. 3.4(b)), the response of 2nd-order NLD is unimodal and symmetric with the peak value at the centre of the blob with a limited non-zero spatial range. In the general cases of $s \neq W$, while the unimodal behaviour is gradually lost and the peak value decreases as the blob size s deviates from the patch size W , the maximum peaks remain at the centre of blobs and they are significantly higher than responses at other positions within blobs. The spatial dependence of the 2nd-order NLD is in general complex since Eq. (3.6) depends not only on the position x_i , but also the value of σ , blob size, contrasts, etc. However, it can be simplified considerably in a special case when a box window ($\sigma \rightarrow +\infty$) is used, the blob size equals the patch size, i. e., $s = W$, and the intensity of the blob is uniform. We can use this expression to explain the essential behaviour of the observed spatial characteristics of 2nd-order NLD. When $s = W$, $\sigma \rightarrow +\infty$, and the signal intensities inside and outside the blob region are unequal but respectively uniform, Eq. (3.6) can then be written explicitly as

$$\left\| \nabla_{\text{NL}}^2 \mathbf{I}(x_i, s = W) \right\|_{2,+\infty} = \begin{cases} M(4 - 3|x_i - x_{i_c}|/W)^{1/2} & \text{if } |x_i - x_{i_c}| \leq W \\ M(2 - |x_i - x_{i_c}|/W)^{1/2} & \text{if } W < |x_i - x_{i_c}| \leq 2W, \\ 0 & \text{otherwise} \end{cases} \quad (3.7)$$

where x_{i_c} is the central pixel of a blob and M is the intensity difference between the blob and its surrounding background. The response of 2nd-order NLD given by Eq. (3.7) is unimodal and symmetric with the peak value at the centre of the blob and a non-zero range of $x_i \in (-2W + x_{i_c}, 2W + x_{i_c})$. We further find in Fig. 3.4(b) that the peak value of the 2nd-order NLD for a blob decreases as the blob size s deviates from the patch size W . To quantify such decreasing, I express the peak value of the 2nd-order NLD as a function of the blob size s by simplifying Eq. (3.6) into

$$\left\| \nabla_{\text{NL}}^2 \mathbf{I}(x_i = x_{i_c}, s) \right\|_{2,+\infty} = \begin{cases} 2M(s/S_p)^{1/2} & \text{if } 0 \leq s \leq S_p \\ 2M[1 - (s/S_p - 1)/2]^{1/2} & \text{if } S_p < s \leq 3S_p, \\ 0 & \text{otherwise} \end{cases} \quad (3.8)$$

where M is the intensity difference between the blob and its surrounding background, S_p is the patch size : $S_p = W$ in the 1-D case. Eq. (3.8) is unimodal with a maximal peak

value of $2M$ when $s = W$ and monotonically decreases when the blob size s deviates the patch size S_P . Fig. 3.4(c) shows the plot of the peak value $\left\| \nabla_{\text{NL}}^2 \mathbf{I}(x_i = x_{i_c}, s) \right\|_{2,+\infty}$ versus the blob size s when $W = 21$ and the intensity difference $M = 50$. We can easily obtain from Eq. (3.8) that $\left\| \nabla_{\text{NL}}^2 \mathbf{I}(x_i = x_{i_c}, s) \right\|_{2,+\infty}$ stays above M (i.e., half of the maximal peak value $2M$) if the size of the blob is within a range $[W/4, 5W/2]$, which gives $[6, 52]$ for $W = 21$.

We have further tested the 2nd-order NLD on the noisy image in Fig. 3.4(a) and shown the results in Fig. 3.4(d). As seen, the main characteristics exhibited in the noisy response curves, i.e., the unimodality, non-zero spatial range (up to a small fluctuation due to noise) and the dependence of the peak values on the blob size remains essentially unchanged, indicating that the 2nd-order NLD is a viable operator for detecting blobs of different sizes in noisy images.

The performance of 2nd-order NLD can be compared to that of Laplacian of a Gaussian (LoG) [109], which has previously been used as an operator for blob detection [110], and also used in the Marr–Hildreth algorithm [] for edge detection. The detection response by LoG at pixel x_i in the same 1-D signal \mathbf{I} involves convolution of \mathbf{I} with the LoG operator

$$\left| \nabla_{\text{LoG},\sigma}^2 \mathbf{I}(x_i) \right| = \left| \sum_{k=-(3W-1)/2}^{(3W-1)/2} (k^2 - \sigma^2) G_\sigma(k) \mathbf{I}(x_{i+k}) \right|. \quad (3.9)$$

Similar to the discussions about the performance of 2nd-order NLD, I apply Eq. (3.9) to the noise-free 1-D signal Fig. 3.4(a) with the same patch size $W = 21$ and a Std $\sigma = 10/3$ so that nearly all values (99.73%) of the Gaussian kernel lie within the window of size $W = 21$ [109]. The response of LoG is shown in Fig. 3.4(b). We can prove through simple manipulations of Eq. (3.6) and Eq. (3.9) that the difference $\Delta(x_i) = \left\| \nabla_{\text{NL}}^2 \mathbf{I}(x_i) \right\|_{2,\sigma} - \left| \nabla_{\text{LoG},\sigma}^2 \mathbf{I}(x_i) \right| > 0$ in a blob region and $\Delta(x_i) \approx 0$ in the background regions. The 2nd-order NLD has therefore a higher response to blobs without increasing false detection in the background regions compared to LoG. Also seen from this figure, the response of LoG for a blob is triple-modal, each of which can be misinterpreted as three blobs due to three local maxima [109]. LoG hence is prone to false blob detections in images. Moreover, I plot the peak response curve of LoG at the centre pixel of a blob versus the blob size s in Fig. 3.4(c) for comparison. As seen, both the 2nd-order NLD and LoG achieve the same maximal peak value $2M$ at $s = W$ and decrease to zero at $s = 0$ and $3W$. However, the 2nd-order NLD decreases in a much

slower rate than LoG. Compared to the blob size range $[6, 52]$ obtained earlier for 2nd-order NLD, LoG possesses a narrower range, $[W/2, 2W] = [11, 42]$. As a result, 2nd-order NLD with a single patch size W (scale) has a higher sensitivity for detecting blobs with different sizes, compared to LoG with same parameters. This is also true for images with noise, as shown in Fig. 3.4(d).

3.2.3 Directional Second-order Nonlocal Difference in 2-D Images

We have formulated and studied the 2nd-order NLD in 1-D signals in the above subsection. In this subsection, I extend the 2nd-order NLD Eq. (3.6) to 2-D images in which both ridges and blobs can be directional features. The detection of these features should take their directions into consideration. Let $I : \Omega \subset \mathbb{R}^2 \rightarrow \mathbb{R}$ be a 2-D image defined on the image domain Ω and $\mathbf{x}_i = [x_i, y_i]^T \in \Omega$ is the pixel position, $\mathbf{x}_i = \mathbf{x}_1, \mathbf{x}_2, \dots, \mathbf{x}_N$. For each pixel, $\mathbf{x}_i = [x_i, y_i]$, the neighbourhood \mathcal{N}_{x_i, y_i} is then defined as a $W \times W$ square region [55] which comprises W^2 pixels centred around $\mathbf{x}_i = [x_i, y_i]^T$. The patch \mathbf{P}_{x_i, y_i} in the 2-D image is then defined as a vector comprising gray-level values of all pixels within the neighbourhood region \mathcal{N}_{x_i, y_i} [51] in the row-wise-concatenations form,

$$\mathbf{P}_{x_i, y_i} = [I(x_{i-(W-1)/2}, y_{i-(W-1)/2}), \dots, I(x_i, y_i), \dots, I(x_{i+(W-1)/2}, y_{i+(W-1)/2})]^T. \quad (3.10)$$

The neighbourhood \mathcal{N}_{x_i, y_i} is chosen as a square region for symmetric consideration [55, 110, 111]. Based on the patch definition Eq. (3.10), I define a 2-D directional 2nd-order NLD at a pixel $\mathbf{x}_i = [x_i, y_i]^T$ along a given direction θ as

$$\begin{aligned} \|\nabla_{\text{NL}}^2 I(\mathbf{x}_i, \theta)\|_{2, \sigma} &= \left\| 2\mathbf{P}_{x_i, y_i} - \mathbf{P}_{x_i - W \cos \theta, y_i - W \sin \theta} - \mathbf{P}_{x_i + W \cos \theta, y_i + W \sin \theta} \right\|_{2, \sigma} \\ &= \left(\frac{1}{C} \sum_{k=-\frac{W-1}{2}}^{\frac{W-1}{2}} \sum_{l=-\frac{W-1}{2}}^{\frac{W-1}{2}} G_{\sigma}(k, l) (2I(x_{i+k}, y_{i+l}) - I(x_{i-W \cos \theta + k}, y_{i-W \sin \theta + l}) - I(x_{i+W \cos \theta + k}, y_{i+W \sin \theta + l}))^2 \right)^{1/2}, \end{aligned} \quad (3.11)$$

where $C = \sum_{k=-\frac{W-1}{2}}^{\frac{W-1}{2}} \sum_{l=-\frac{W-1}{2}}^{\frac{W-1}{2}} G_{\sigma}(k, l)$ is a normalizing factor. As shown in Fig. 3.5(c), Eq.

(3.11) involves the difference between a central patch and two neighbors along a given direction. A large directional 2nd-order NLD $\|\nabla_{\text{NL}}^2 I(\mathbf{x}_i, \theta)\|_{2, \sigma}$ corresponds to a brighter (darker) patch compared with two neighbors along the direction θ , so indicating the presences of blobs and ridges whose principal directions are perpendicular to θ .

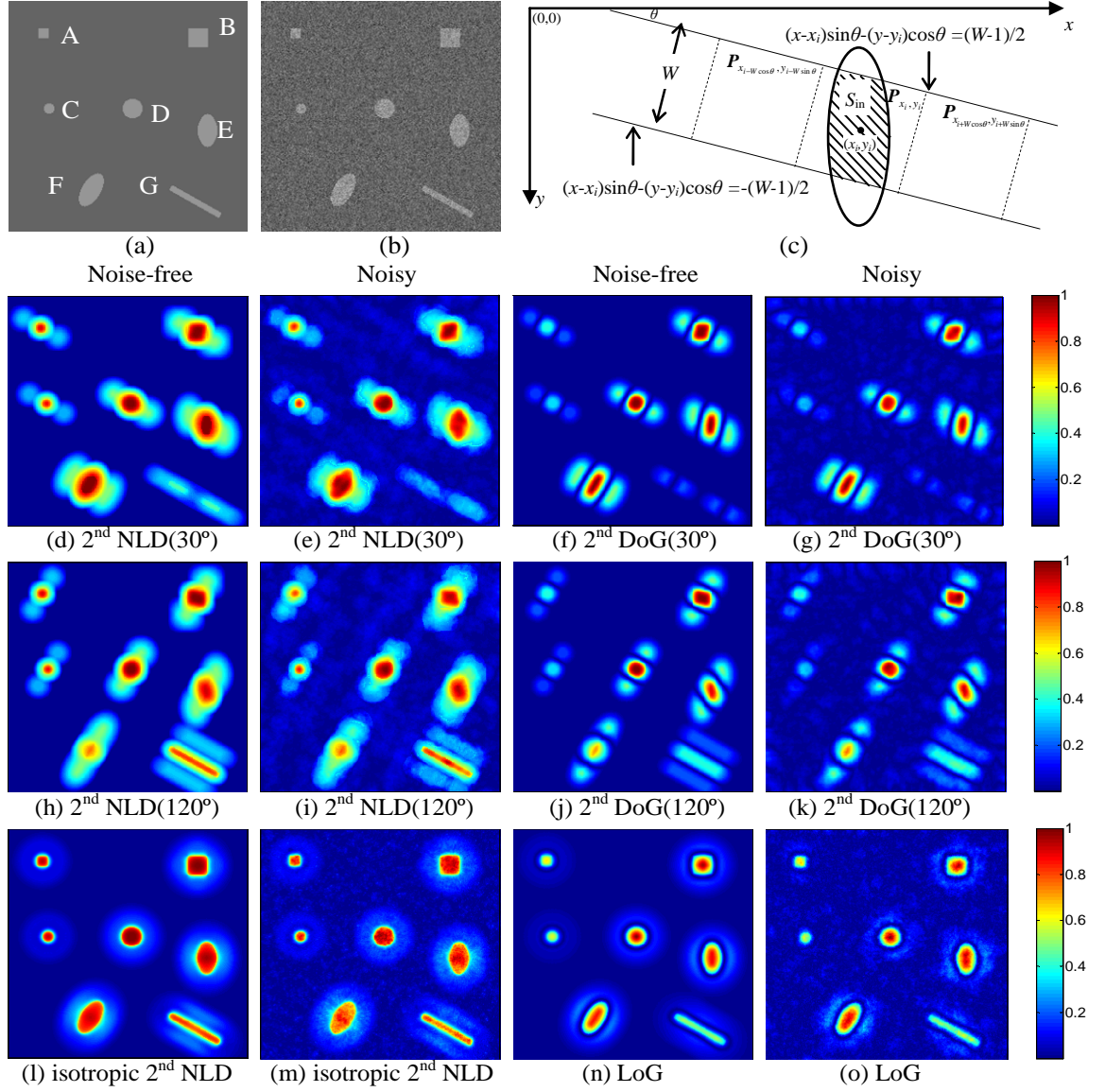


Fig. 3.5 Performance illustration of the 2nd-order NLD in 8-bit 2-D images. (a) A noise-free synthetic 8-bit image consists of blobs and ridges with various shapes, sizes and orientations; (b) A noisy observation corrupted by AWGN of Std $\sigma_n = 20$; (c) A schematic showing directional 2nd NLD in 2-D space; (d) – (g) Responses of directional 2nd-order NLD at 30° for noise-free and noisy image, and that of 2nd-order DoG at 30° on same images; (h) – (k) Responses of directional 2nd-order NLD at 120° for noise-free and noisy image, and that of 2nd-order DoG at 120° on same images; (l) – (o) Responses of isotropic 2nd-order NLD for noise-free and noisy image, and those of LoG on the two images.

To illustrate the performance of the 2nd-order directional NLD as a blob and ridge

detector, I study the behavior of $\|\nabla_{\text{NL}}^2 I(\mathbf{x}_i, \theta)\|_{2, \sigma}$ in an 8-bit 2-D image without and with AWGN of Std $\sigma_n = 20$, as shown in Fig. 3.5(a-b), which consist of blobs of dimensions 11×11 and 21×21 (pixels), two circular blobs of the diameters 11 and 21, two elliptical blobs with same major and minor diameters of 41 and 21 in two orientations at 90° and 120° , and a ridge of length 61 and width of 5 at 30° , respectively. Each of the features is marked with a letter. Intensities of the features and backgrounds are set to be 150 and 100 respectively, same as the setting of those in the 1-D experiment Fig. 3.4(a). We first apply the 2-D directional 2nd-order NLD Eq. (3.11) along two directions perpendicular to each other at $\theta = 30^\circ$ and 120° to the noise-free image. The responses are shown respectively in Fig. 3.5(d) and (h), where the patch height (width) $W = 21$ and $\sigma = 10/3$ are chosen, same as in the 1-D experiment. It is obvious that the responses are general directionally dependent. However, the essential behavior of the responses for the each given direction (here $\theta = 30^\circ$ and 120°), such as the peak locations, the symmetry, and the intensity profiles, are similar to the 1-D case. The peak values, similar to the 1-D case, still depend on the objects sizes. We can analytically explain easily this dependence for the case of $\sigma \rightarrow +\infty$ by simplifying Eq. (3.11) into the following form,

$$\|\nabla_{\text{NL}}^2 I(\mathbf{x}_i = x_{i_c}, s_\theta)\|_{2, +\infty} = \begin{cases} 2M (s_\theta / S_p)^{1/2} & \text{if } 0 \leq s_\theta \leq S_p \\ 2M [1 - (s_\theta / S_p - 1) / 2]^{1/2} & \text{if } S_p < s_\theta \leq 3S_p, \\ 0 & \text{otherwise} \end{cases} \quad (3.12)$$

where S_p is the patch size, s_θ is the size of blob and ridge region bounded between two lines $(x - x_{i_c}) \sin \theta - (y - y_{i_c}) \cos \theta = \pm \frac{W-1}{2}$ and θ is the angle of the directional 2nd-order NLD, as illustrated in Fig. 3.5(c). The parameter M is the intensity difference (feature contrast) between features and backgrounds. Eq. (3.12) has the same function expression as the peak value, Eq. (3.8), in the 1-D case, allowing same dependence for peak values of directional 2nd-order NLD on size ratio s_θ / S_p as that in the 1-D case, except now that s_θ / S_p is the 2-D area ratio which depends on both the size and orientation of the object. For example, for blob F, $\theta = 30^\circ$ and 120° correspond to directions perpendicular and parallel to the principal orientation of the blob and the area ratio for the two cases are $s_\theta / S_p \approx 1$ and $\pi/2$, respectively. Consequently the peak value for blob F at $\theta = 30^\circ$ (Fig. 3.5(d)) equals $2M$ and is much higher than that at $\theta = 120^\circ$ (Fig. 3.5 (h)) according to Eq. (3.12).

We have also tested the noisy image Fig. 3.5(b) by applying the 2nd-order NLD along the same directions at $\theta = 30^\circ$ and 120° , the results of which are shown respectively in Fig. 3.5(e) and (i). As seen, the responses of 2nd-order NLD are essentially the same as those to the noise-free image in the same directions, in a similar manner as the comparisons of characteristics in the 1-D case between the noisy-free Fig. 3.4(b) and noisy responses Fig. 3.4(d) of the 1-D 2nd-order NLD. Accordingly, the directional 2nd-order NLD Eq. (9), same as the 1-D 2nd-order NLD for feature detection in the 1-D noisy signals, is viable for detecting blobs and ridges with different sizes, shapes and orientations in the 2-D noisy images.

For completeness, I compare Eq. (9) with 2nd-order directional derivative of Gaussian (2nd-order DoG), which has previously been used for 2-D blob and ridge detection [111]. The detection response by 2nd DoG at pixel $\mathbf{x}_i = [x_i, y_i]^T$ along the orientation θ can be written as

$$\left| \nabla_{\text{DoG}, \sigma}^2 I(\mathbf{x}_i, \theta) \right| = \left| \sum_{k=-(3W-1)/2}^{(3W-1)/2} \sum_{l=-(3W-1)/2}^{(3W-1)/2} \left[(k \cos \theta - l \sin \theta)^2 - \sigma^2 \right] G_\sigma(k, l) I(x_{i+k}, y_{i+l}) \right|. \quad (3.13)$$

Similar to the performance comparison between 1-D 2nd-order NLD and 1-D LoG in our 1-D experiment in the previous subsection, I apply Eq. (3.13) to the noise-free and noisy images Fig. 3.5(a) and (b) along the same directions at $\theta = 30^\circ$ and 120° , the response of which are further shown in Fig. 3.5 (f), (g) and Fig. 3(j), (k) respectively, with the same patch height $W = 21$ and Std $\sigma = 10/3$. In general, the 2nd-order DoG $\left| \nabla_{\text{DoG}, \sigma}^2 I(\mathbf{x}_i, \theta) \right|$ can be seen as a 1-D LoG along a given direction θ , so potentially exhibiting the characteristics of 1-D LoG which I have analyzed for Eq. (3.9) in Section 3.2.2. This is hence no surprise that responses of 2nd-order DoG in Fig. 3.5(f), (g) and (j), (k) all show apparent triple-modal shapes and lower peak values, particularly for blob A, C and ridge G, compared to the results of 2nd-order NLD in Fig. 3(d), (e) and (h), (i), respectively. All of these are consistent with the observations of Fig. 3.4(b) and (d). In this sense, the conclusions obtained in 2-D images are consistent with those in the 1-D case.

3.2.4 Isotropic Second-order Nonlocal Difference in 2-D Images

As shown above, the responses of both directional 2nd-order NLD and DoG are directionally dependent. That is, for two features with same shapes, sizes and brightness

but varied orientations, the operator yields different values [112]. For example, the responses for two blobs E and F in Fig. 3.5(a), with same shapes, sizes and contrasts but varied orientations, are totally different in a same figure, such as Fig. 3.5(h) or (j). As such, the directions of the features should be known a priori when the operator is applied to the images for detection. However, the knowledge of the feature directions in most cases is unknown to us and thus has to be estimated by other methods. This may greatly increase the computational burden and decrease the detection sensitivity of the detectors if the directions are not estimated accurately. To overcome this problem, the Laplacian of Gaussian was proposed as [109]

$$\left| \nabla_{\text{LoG}, \sigma}^2 I(\mathbf{x}_i) \right| = \left| \nabla_{\text{DoG}, \sigma}^2 I(\mathbf{x}_i, 0) + \nabla_{\text{DoG}, \sigma}^2 I(\mathbf{x}_i, 90) \right| = \left| \sum_{k=-(3W-1)/2}^{(3W-1)/2} \sum_{l=-(3W-1)/2}^{(3W-1)/2} (k^2 + l^2 - 2\sigma^2) G_{\sigma}(k, l) I(x_{i+k}, y_{i+l}) \right|, \quad (3.14)$$

which is the isotropic sum of 2nd-order DoG in two dimensions and thus a rotationally invariant [109]. Following the same approach, I formulate an isotropic 2nd-order NLD as

$$\begin{aligned} \left\| \nabla_{\text{NL}}^2 I(\mathbf{x}_i) \right\|_{2, \sigma} &= \frac{1}{2} \left\| \nabla_{\text{NL}}^2 I(\mathbf{x}_i, 0) + \nabla_{\text{NL}}^2 I(\mathbf{x}_i, 90) \right\|_{2, \sigma} \\ &= \frac{1}{2} \left\| 4\mathbf{P}_{x_i, y_i} - \mathbf{P}_{x_i, y_i-W} - \mathbf{P}_{x_i, y_i+W} - \mathbf{P}_{x_i-W, y_i} - \mathbf{P}_{x_i+W, y_i} \right\|_{2, \sigma}. \end{aligned} \quad (3.15)$$

which is an isotropic (rotationally invariant) operator and can thus yield same responses to identical features oriented at different angles.

We illustrate the performance of the isotropic 2nd-order NLD by applying Eq. (3.15) respectively on the noise-free and noisy images Fig. 3.5(a) and (b), where patch height $W = 21$ and $\sigma \rightarrow +\infty$ are chosen, same as those in the previous subsection. Responses of the two images are shown in Fig. 3.5(l) and (m). As seen, profiles of isotropic 2nd-order NLD for all features are very close to the original ones. Also as seen from the two figures, the 2nd-order isotropic NLD operator provides the same responses to the two elliptical blobs E and F with the same shapes, sizes and brightness but varied orientations, indicating the rotational invariance of Eq. (3.15). By considering the computational speed and detection sensitivity, the isotropic 2nd-order NLD is thus a better operator independent of the feature directions than the directional one to detect the blob and ridge features in the 2-D images and thus more appropriate to derive the smoothing strength for a diffusion model in the next section, in which the strength should be independent of the feature directions and only derived by the contrasts of the features [9, 49].

To illustrate the consistent advantages of the 2nd-order NLD over the 2nd-order derivative of Gaussian, I apply the 2-D LoG Eq. (3.14) to Fig. 3.5(a) and (b) and show the two response images in Fig. 3.5(n) and (o). Obvious triple-modal behavior and lower peak values are again observed compared to the responses of the 2nd-order NLD. All the results and comparisons indicate that the 2nd-order NLD performs noticeably better than the LoG in 2-D case as a blob and ridge detector.

3.3 Feature-Preserving Diffusion

A diffusion coefficient (DC) in the traditional nonlinear diffusion model, such as the PM model Eq. (2.9) or (2.10) [9], is a decreasing function of the gradient of image I , the value of which is small in the vicinity of edges and relatively large in background areas, so giving rise to edge-preserving diffusion. In this section, I begin with a feature-preserving nonlinear diffusion (FP-ND) for the 1-D signal $I: \Omega \subset \mathbb{R} \rightarrow \mathbb{R}$ in the image domain Ω in the form,

$$\frac{\partial I(x, t)}{\partial t} = \text{div} \left[c \left(\left\| \nabla_{\text{NL}}^2 I(x, t) \right\|_{2, \sigma} \right) \cdot \nabla I(x, t) \right] \quad (3.16)$$

where the diffusion coefficient (DC),

$$c \left(\left\| \nabla_{\text{NL}}^2 I(x, t) \right\|_{2, \sigma} \right) = \exp \left(- \frac{\left\| \nabla_{\text{NL}}^2 I(x, t) \right\|_{2, \sigma}^2}{h^2} \right), \quad (3.17)$$

is a decreasing function of the 1-D 2nd-order NLD Eq. (3.6), $I(x, t=0) = J(x)$ is the initial noisy image, ∇ is the gradient operator, div is the divergence operator and h is the diffusion threshold. If $\left\| \nabla_{\text{NL}}^2 I(x, t) \right\|_{2, \sigma} \gg h$, $c \left(\left\| \nabla_{\text{NL}}^2 I(x, t) \right\|_{2, \sigma} \right) \rightarrow 0$ and the diffusion flux is suppressed; if $\left\| \nabla_{\text{NL}}^2 I(x, t) \right\|_{2, \sigma} \ll h$, $c \left(\left\| \nabla_{\text{NL}}^2 I(x, t) \right\|_{2, \sigma} \right) \rightarrow 1$ and the diffusion flux is encouraged. Thus the parameter h serves as a threshold to determine whether or not a smoothing behavior is encouraged. We employ the median absolute deviation (MAD) of the 2nd-order NLD to adaptively estimate h at each iteration step during diffusion process [47, 48] (see Section 3.4 for more details).

The DC Eq. (3.17) is unimodal of the 2nd-order NLD, which remains a one-to-one correspondence between the local minima and true blobs, and is lower in value in the vicinity of blob features than noisy background. Fig. 3.4(e) shows an example of the DC $c \left(\left\| \nabla_{\text{NL}}^2 I(x, t) \right\|_{2, \sigma} \right)$, corresponding to the 2nd-order NLD $\left\| \nabla_{\text{NL}}^2 I(x, t) \right\|_{2, \sigma}$ given in Fig. 3.4

(d), where the diffusion threshold h is chosen to be $h = 20$, same as the Std σ_n of the AWGN in the corrupted image. We will show through experiments in Section 3.4 that the FP-ND filter Eq. (3.17) can successfully smooth out noise and preserve the three blobs. For further comparisons, I also plot DC in the exponential form of LoG response in Fig. 3.4 (e), which exhibits the same triple-modal shape and has higher value in blob regions in comparison.

In 2-D images, ridges are line-like features with different orientations and blobs can be approximated by directional ellipses. To better preserve the geometric properties of the features, smoothing behaviour should be performed in directions parallel rather than perpendicular to the isophotes of the images [52]. We propose a feature-preserving nonlinear anisotropic diffusion (FP-NAD) that smooths along the direction of the image contours [49]. In this case, the diffusion model for a 2-D image $I : \Omega \subset \mathbb{R}^2 \rightarrow \mathbb{R}$ is not manipulated by the scalar DC in Eq. (3.16), but by a 2×2 diffusion tensor (DT) \mathbf{D} in the following form,

$$\frac{\partial I(\mathbf{x}, t)}{\partial t} = \text{div}[\mathbf{D}(\mathbf{x}, t) \nabla I(\mathbf{x}, t)], \quad (3.18)$$

where $\mathbf{x} = [x, y]^T \in \mathbb{R}^2$ is a pixel and $\nabla I(\mathbf{x}, t) \in \mathbb{R}^2$ is a vector whose elements are gradients at the pixel \mathbf{x} along x -axis and y -axis. As a symmetric and semi-positive-definite 2×2 matrix, \mathbf{D} can be expressed as [50],

$$\mathbf{D}(\mathbf{x}, t) = f_0(\mathbf{x}, t) \mathbf{V}_0 \mathbf{V}_0^T + f_1(\mathbf{x}, t) \mathbf{V}_1 \mathbf{V}_1^T \quad (3.19)$$

where the vectors $\mathbf{V}_0, \mathbf{V}_1$ and the scalars f_0, f_1 are the eigenvectors and eigenvalues of the DT \mathbf{D} , respectively. The vectors \mathbf{V}_0 and \mathbf{V}_1 determine the smoothing directions during the diffusion process and are commonly chosen to be the eigenvectors of the structure tensor $\mathbf{S} = G_\rho * \nabla(G_\sigma * I) \nabla(G_\sigma * I)^T$ [13, 49, 50, 52], pointing to the directions perpendicular and parallel to image isophotes. The eigenvalues f_0, f_1 in Eq. (3.19) determine the strengths of the local smoothing behaviour along the directions $\mathbf{V}_0, \mathbf{V}_1$ in a diffusion process. Therefore how to obtain the two values determines the performance of the diffusion Eq. (3.18). We find that when the edges are partly lost or contaminated by severe noise, high values of smoothing strengths f_0, f_1 will lead to oversmoothing of the blob and ridge features if the smoothing strengths are derived as decreasing functions of low amplitudes of gradient, as in previous studies [9, 12, 13, 46-52]. The problems can be overcome if the more robust 2nd-order NLD based operator is used. The smoothing strengths should be also independent of feature directions so two

identical objects with different orientations can be smoothed equally. We here propose the eigenvalues f_0, f_1 as decreasing functions

$$f_0(\nabla_{\text{NL}}^2 I(\mathbf{x})) = c\left(\|\nabla_{\text{NL}}^2 I(\mathbf{x}, t)\|_{2, \sigma}\right) \text{ and } f_1(\nabla_{\text{NL}, \sigma}^2 I(\mathbf{x}, t)) = \left[f_0(\nabla_{\text{NL}}^2 I(\mathbf{x}, t))\right]^{1/2} \quad (3.20)$$

of the isotropic 2nd-order NLD $\|\nabla_{\text{NL}}^2 I(\mathbf{x}, t)\|_{2, \sigma}$ Eq. (3.15), where the form of $c\left(\|\nabla_{\text{NL}}^2 I(\mathbf{x}, t)\|_{2, \sigma}\right)$ is same as Eq. (3.17). By constructing the diffusion tensor \mathbf{D} with Eq. (3.19) and Eq. (3.20), our diffusion model Eq. (3.18) can thus perform various smoothing behaviours for different regions: In background regions the 2nd-order NLD is small and $\lim_{\|\nabla_{\text{NL}}^2 I\|_{2, \sigma} \rightarrow 0} f_0 \approx \lim_{\|\nabla_{\text{NL}}^2 I\|_{2, \sigma} \rightarrow 0} f_1 = 1$, so smoothing behaviours in the direction θ_0 and θ_1 are encouraged at an equal level (isotropic smoothing). In the vicinity of blobs and ridges, since $\|\nabla_{\text{NL}}^2 I\|_{2, \sigma}$ is large, $\lim_{\|\nabla_{\text{NL}}^2 I\|_{2, \sigma} \rightarrow +\infty} f_0 = 0$ and $\lim_{\|\nabla_{\text{NL}}^2 I\|_{2, \sigma} \rightarrow +\infty} f_1 = 0$ and smoothing behaviours in the two directions are discouraged. Furthermore, both the eigenvalues f_0, f_1 are smaller than 1 and the latter is the square root of the former, giving rise to $\lim_{\|\nabla_{\text{NL}}^2 I\|_{2, \sigma} \rightarrow +\infty} \frac{f_0}{f_1} = 0$. As such, smoothing behaviours along the direction perpendicular to the intensity isophotes, regardless of whether isophotes are located around blobs or ridges, is discouraged at a higher order to better preserve the shapes of the features.

Our method, Eq. (3.18), is different from several previous tensor-driven methods [13, 49, 50, 52], in which the smoothing strengths (the eigenvalues f_0, f_1 of the tensor \mathbf{D}) are derived by the gradient, whereas in our method they are determined by a 2nd-order NLD. The latter allows better preservation of blob and ridge features, compared to other diffusion methods [13, 49, 50, 52], particularly under severe noise contamination. This will be demonstrated experimentally in the next section. Our method derives the smoothing directions in the same way as previous methods by using the eigenvectors of the structure tensor $\mathbf{S} = G_\rho * \nabla(G_\sigma * I) \nabla(G_\sigma * I)^T$. This is due to the fact that the directions of objects, such as blobs and ridges, are reinforced by the structure tensor through the use of the direction coherence of these features [50], even when edges that bound them are partly lost or broken due to noise contamination [13].

We further discuss the similarity and difference between our diffusion model Eq. (3.18)-(3.20) and the anisotropic diffusion in the space of patches (ADSP) [51]. Although the ADSP, at a first look, is similar to our method, the two methods are

essentially different. While both methods involve the concept of image patches in the formulation of diffusion models, the smoothing strengths and directions in the two methods are determined respectively by different operators and structure tensors: in ADSP they are derived respectively by the trace $\text{tr}[\mathbf{S}_{(P)}]$ and eigenvector of a new structure tensor $\mathbf{S}_{(P)} = \nabla \tilde{\mathbf{I}}_{(P)} \nabla \tilde{\mathbf{I}}_{(P)}^T$ constructed in a high-dimensional patch space [51], where $\tilde{\mathbf{I}}_{(P)}$ denotes the projection of image \mathbf{I} onto the patch space. The eigenvector $\tilde{\mathbf{u}}_{(P)}$ gives the orientation perpendicular to the isophotes of $\tilde{\mathbf{I}}_{(P)}$. The trace $\text{tr}[\mathbf{S}_{(P)}]$ is the Euclidean norm of the gradient in the patch space so the smoothing strength is reduced at locations with high patch-gradients. Technically ADSP is a diffusion method based on gradient (edge) measurement and an edge-based (enhancing) diffusion in the patch space. Such method has shown better denoising performance compared to NLM filter [51]. Our method, on the contrary, computes smoothing strengths by the 2nd-order NLD which measures the difference between several neighbouring 1st-order patch differences. Since the 2nd-order NLD has a higher response to blob and ridge features than the 1st-order difference (gradient), particularly when edges bounding features are partly lost or contaminated under severe noise, the smoothing strengths f_0 and f_1 Eq. (3.20) by the 2nd-order NLD obtained in our method is expected to perform better in the diffusion process for blob and ridge feature preserving and noise removing.

3.4 Experiments

In this section I present visual and numerical results obtained by using our diffusion method, first for a 1-D signal and subsequently 2-D images. It is common to terminate the diffusion after a fixed number of diffusion iterations. However, such a mechanism is not flexible and it is difficult to produce satisfactory results. Here, I utilize the mean squared difference-norm (MSDN) criterion [108] to stop the diffusion automatically. The MSDN between two adjacent diffusion steps can be written as,

$$\text{MSDN}(\mathbf{I}(t)) = \frac{1}{N} \sqrt{\sum_{i=1}^N (I(\mathbf{x}_i, t) - I(\mathbf{x}_i, t-1))^2}, \quad (3.21)$$

where N is the number of pixels and t denotes the iteration time. In the diffusion process, the MSDN value decreases exponentially with the number of iterations. The diffusion is terminated when the MSDN reaches to a certain small value. We set this value as 1% in all experiments of this section, implying that the diffusion process has sufficiently converged. Besides, in all tests the diffusion threshold h of Eq. (3.20) at each iteration

step during diffusion process is estimated by employing the median absolute deviation (MAD) [16, 47]

$$\begin{aligned} h &= 1.4826 \text{MAD}(\|\nabla_{\text{NL}}^2 I(x, t)\|_{2, \sigma}) \\ &= 1.4826 \text{median}\left\{\left\|\nabla_{\text{NL}}^2 I(x, t)\right\|_{2, \sigma} - \text{median}(\|\nabla_{\text{NL}}^2 I(x, t)\|_{2, \sigma})\right\} \end{aligned} \quad (3.22)$$

of the 2nd-order NLD. The mechanism of MAD operator has been discussed in detail in [47] and proven very effective in estimating the diffusion threshold [16, 47]. The parameter h varies adaptively and converges during the diffusion process, the value of which depends on the complexity of structures in the images.

We compare our results with those of existing methods, including PM¹ [9], Catté [12]¹, coherence-enhancing diffusion method (CED¹) [13], tensor-driven curvature-preserving diffusion (TDCPD²) [52], anisotropic diffusion in the space of patches (ADSP¹) [100], NLM filt³ [53], structure adaptive filter (SAFIR) [16] and block matching and 3-D collaborative filtering (BM3D⁴) [58]. The last method is considered to be the best denoising algorithm at present [96, 97].

¹ Using the code at http://visl.technion.ac.il/~gilboa/PDE-based_image_filtering.html

² Using the software provided by the author at <http://gmic.sourceforge.net/gimp.shtml>

³ Using the code at <http://www.mathworks.com/matlabcentral/fileexchange/13619>

⁴ Using the code provided by the author at <http://www.cs.tut.fi/~foi/GCF-BM3D/BM3D.zip>

3.4.1 1-D Signals

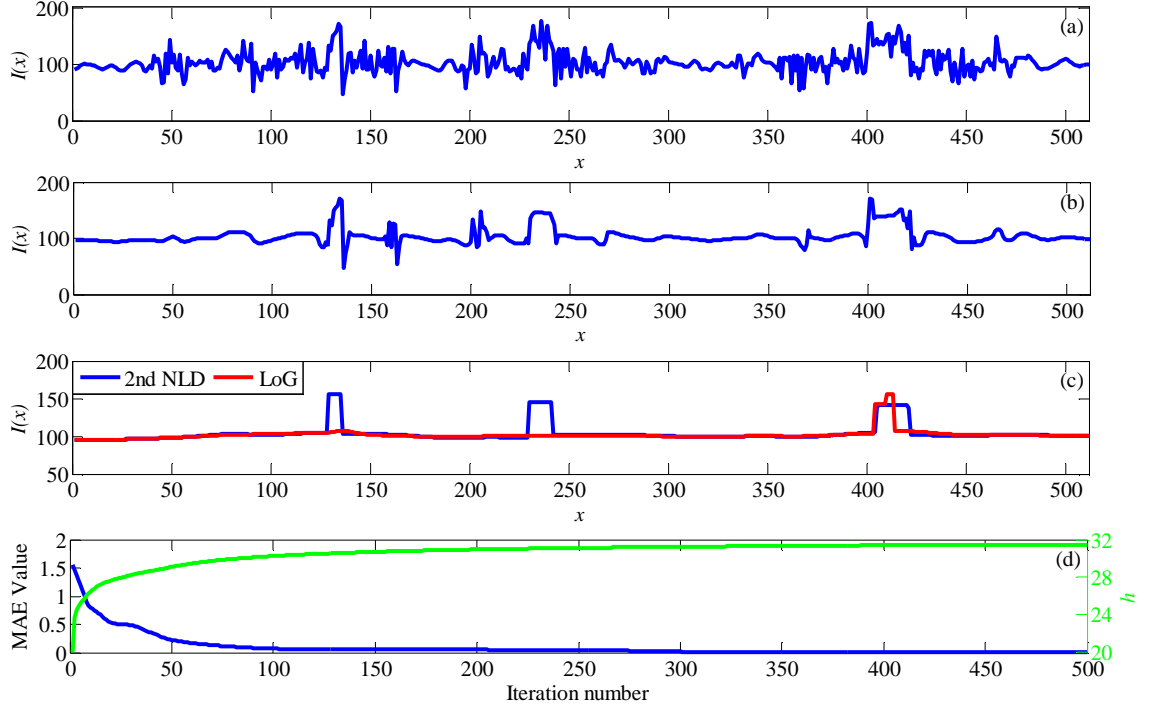


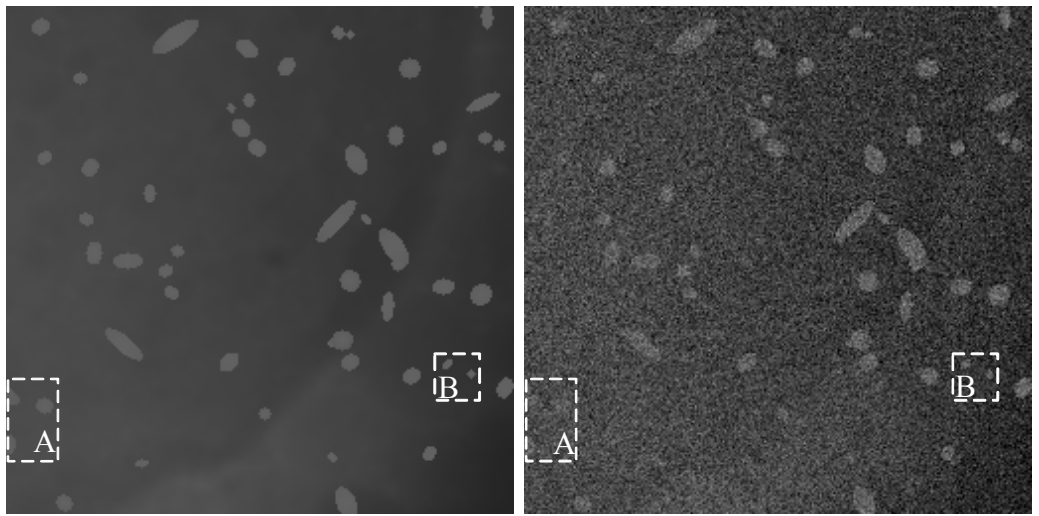
Fig. 3.6 Evolution of the 1-D noisy signal given in Fig. 3.4(a). (a) - (b) Results by FP-ND in two different stages; (c) The final denoised signal after 472 iterations. The same approach with DC using LoG response is also plotted for comparison; (d) MSDN values and the diffusion threshold h of FP-ND versus the iteration number.

We first test the FP-ND filter Eq. (3.16) on the 1-D noisy image Fig. 3.4(a). The patch size W is chosen as $W = 21$, same as the size of the largest blob. The initial value of the diffusion threshold h is set to be $h = 20$, same as the Std σ_n of the AWGN in the image, and is updated using the MAD operator Eq. (3.22) at each iteration. Fig. 3.6(a) - (c) illustrate the denoising results of the noisy image Fig. 3.4(a) at different stages during the diffusion process. As seen from Fig. 3.4(e), the DC is much higher in background regions far from three blobs than in the regions close to them. As such, FP-ND smooths more heavily on the former regions in the initial stage while leaves the regions in the vicinity of blobs essentially unchanged, as shown in Fig. 3.6(a). As the diffusion threshold h gradually increases during the evolution (Fig. 3.6(e)), the DC in the vicinity of blobs also gradually increases due to the characteristics of the exponential function in Eq. (3.17). The smoothing effect then “propagates” towards the blobs regions in the diffusion process as shown in Fig. 3.6(b). Background regions away from blobs continue to be smoothed during this period. As noise is gradually removed, the difference of the images between two adjacent iterations becomes increasingly smaller. The diffusion process stops when MSDN is reduced to 0.01. The final result is

plotted in Fig. 3.6(c), showing good preservation of the three blobs at different sizes compared to those in the noise-free image Fig. 3.4(a). The MSDN given in Fig. 3.6(d) is shown to decrease exponentially so the convergence of the diffusion filter can be guaranteed. The diffusion threshold h versus iteration number is also plotted in this figure, which increases monotonically during the diffusion process. For comparison, I also denoise the same noisy image in Fig. 3.4(a) by a nonlinear diffusion filter whose DC is calculated by the LoG response Eq. (3.9), the result of which is shown Fig. 3.6(c). As seen, the two smaller blobs are removed whereas the largest one is significantly distorted.

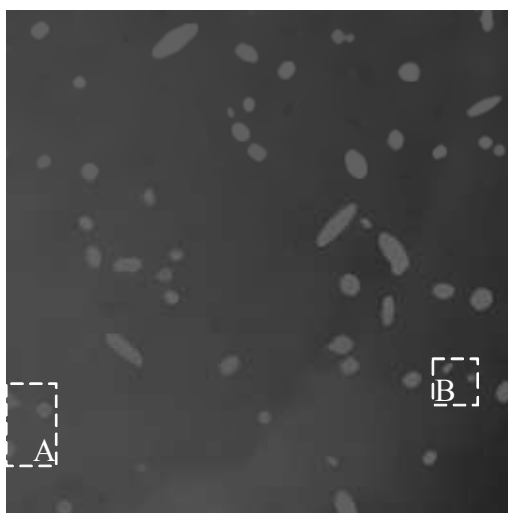
3.4.2 2-D Images

3.4.2.1 Denoising of a Synthetic Image Containing Blobs

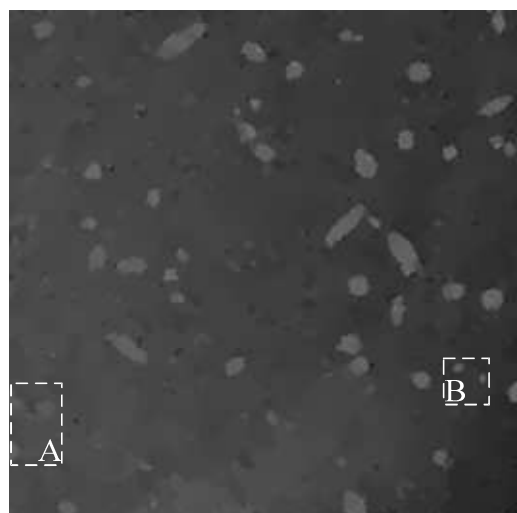


(a) Noise-free

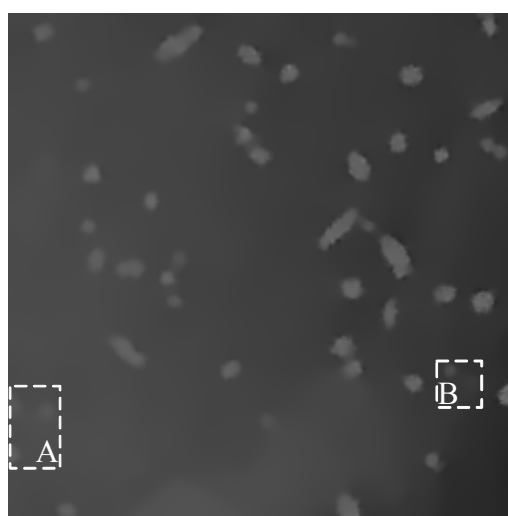
(b) Noisy



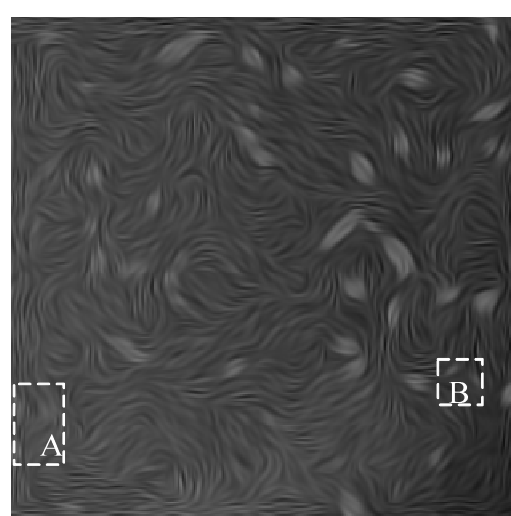
(c) My method



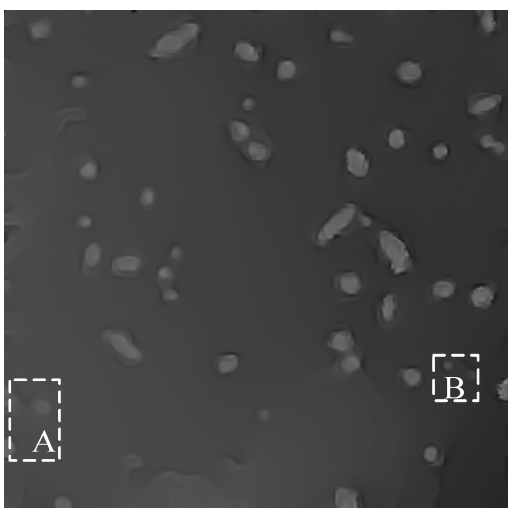
(d) PM



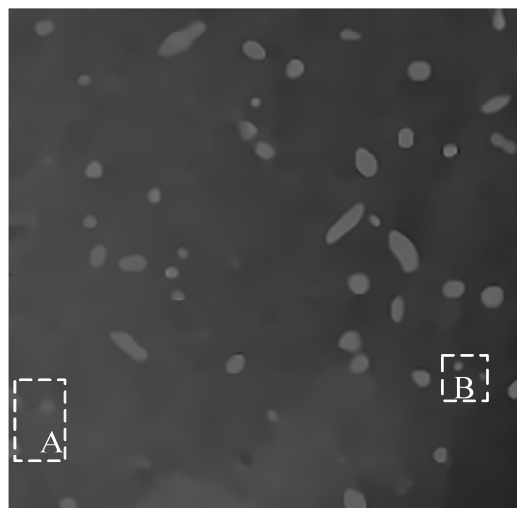
(e) Catté,



(f) CED



(g) TDCPD



(h) ADSP

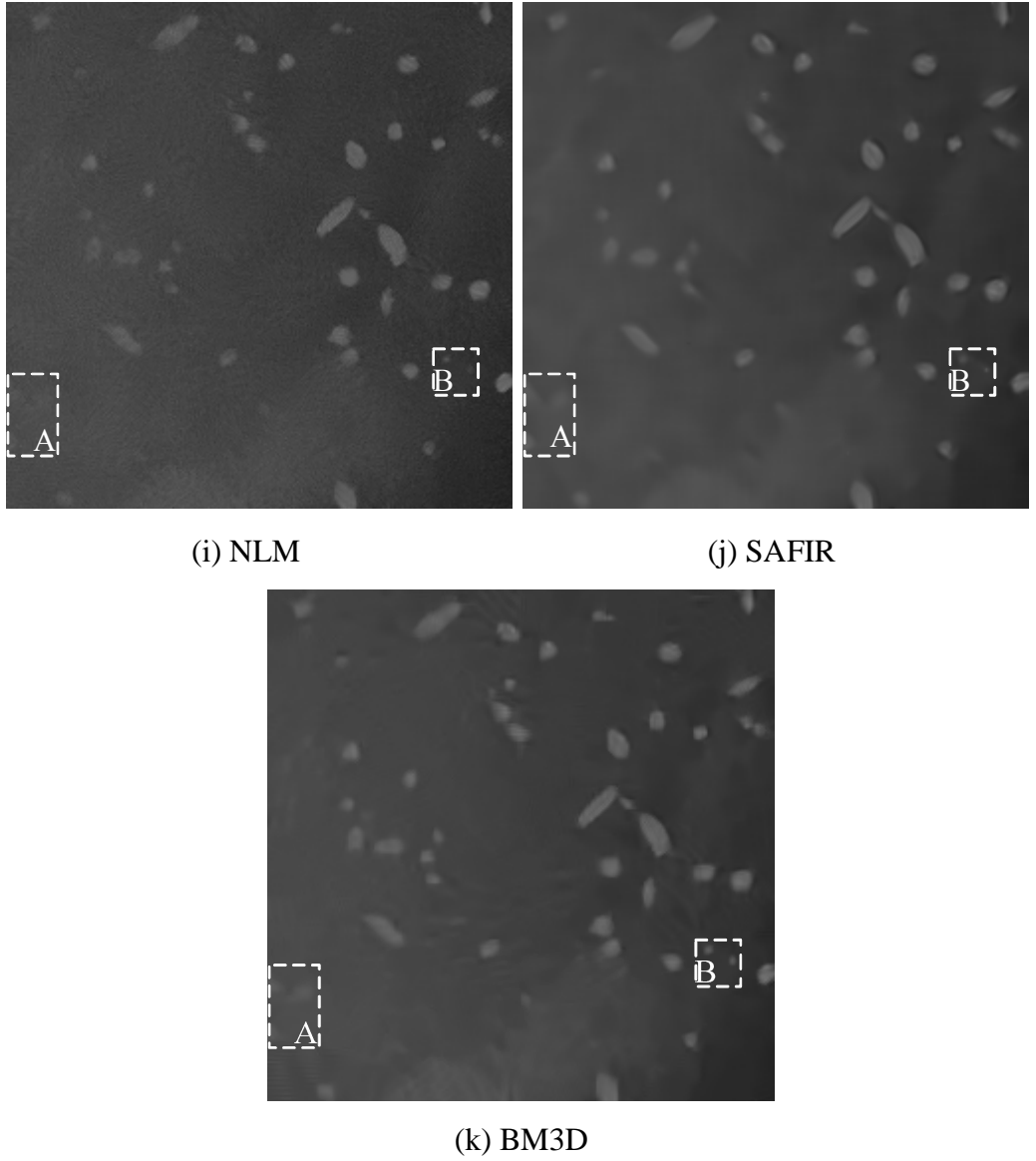


Fig. 3.7 Denoising results of a synthetic live-cell image. (a) Noise-free image. (b) Simulated noisy image with AWGN (Std $\sigma_n = 20$). (c) - (k) Denoised results by FP-NAD, PM, Catté, CED, TDCPD, ADSP, NLM filter, SAFIR and BM3D, respectively. Two boxes in each image are marked by A and B for detailed comparisons.

Table 3.1

PSNR and MSSIM results on the noise-free live-cell image Fig. 3.7(a) corrupted with AWGN of Std $\sigma_n = 20$ (Fig. 3.7(b)), 30 and 40, by our method, PM, Catté, CED, TDCPD, ADSP, NLM filter, SAFIR and BM3D, the visual results of which for $\sigma_n = 20$ have been shown in Fig. 3.7(c) – (k), respectively.

σ_n	PSNR value(dB)/MSSIM value									
	Noisy	Our	PM	Catté	CED	TDCPD	ADSP	NLM	SAFIR	BM3D
20	22.1/0.186	39.2/0.973	36.2/0.938	36.6/0.923	28.9/0.637	36.4/0.941	36.7/0.953	34.4/0.838	36.7/0.956	37.4/0.955
30	18.8/0.101	36.6/0.957	34.2/0.916	34.9/0.905	27.0/0.516	34.4/0.922	34.3/0.936	31.4/0.718	34.6/0.936	35.0/0.935
40	16.5/0.065	35.9/0.950	32.3/0.887	33.7/0.870	24.2/0.458	33.2/0.898	33.5/0.913	29.9/0.634	33.4/0.919	33.8/0.920

We first undertake experiments with an 8-bit 2-D image that simulates moving particles in live cells recorded by a microscope. The image is constructed by using a linear model [56] that comprises blobs, uneven background and AWGN with a Std $\sigma_n=20$. The noise-free and noisy images are shown in Fig. 3.7(a) and (b). As seen, the blobs are circular or ellipse regions with varying directions and intensities, the size of which can be estimated by two orthogonal axes of a blob, the shortest one is 5 pixels whilst the longest is 31 pixels.

We apply the feature-preserving nonlinear anisotropic diffusion (FP-NAD) filter Eq. (3.18) to the noisy image Fig. 3.7(b). The patch size for calculating 2nd-order NLD by Eq. (3.15) is set to be 15×15 pixels, between the shortest and longest axes of the blobs in the image. The parameter h is chosen initially to be $h=20$, equal to the Std σ_n of the noise, and is updated using the MAD operator at successive iterations. The diffusion process stops when the MSDN Eq. (3.21) is less than 0.01. The denoised result by the FP-NAD is shown in Fig. 3.7(c). As seen, all particles are correctly preserved by comparing to the noise-free image Fig. 3.7(a), including those which are very weak in region A and much smaller than the patch size in region B.

The denoised results of the same noisy image by PM, Catté, CED, TDCPD, ADSP, NLM filter, SAFIR and BM3D, are shown in Fig. 3.7(d)-(k). For PM and Catté, the time interval is set to be $\Delta t = 0.2$ and the processes stop when the MSDN Eq. (3.21) is less than 0.01. For NLM filter, the patch window and searching window are set to be 7×7 and 21×21 pixels, both of which follow the suggested values in [53]. The filtering parameter h of the NLM filter determines the weight of NLM filter, the value of which, according to ref [53], is chosen within the operation window of $h = \alpha \cdot \sigma_n$ with $\alpha \in [0.75, 1]$ for a high visual quality solution. Here I choose a middle value $h = 0.8\sigma_n$. In SAFIR, the patch window is set to be 9×9 , the maximum number of increments for the nested window size is 4, the critical parameters $\lambda_{0.01} = 113.5$ and $\rho = 3$. The reasons for choosing these parameter values are explained in an original paper [16]. The

parameters for BM3D used in all tests follow ‘Normal Profile’ in Table I in reference [58]. Note that since the parameters were not given explicitly in CED [13], TDCPD [52] and ADSP [100], I have varied the parameters used in these three methods exhaustively to obtain the best possible results with respect to PSNR.

By a visual comparison, Catté, TDCPD, NLM filter, SAFIR and BM3D result in over-smoothing of blobs when the image is strongly corrupted by noise, especially for the barely visible features in region A in the image and the small-size features in region B. CED distorts the blobs by elongating the shapes and produces several line-like artifacts in background regions because the method is designed especially for denoising images with repetitive flow-like patterns [13]. ADSP preserves blob features better than the above six methods because the smoothing strength is determined by using patch difference. Oversmoothing of blobs, however, can be still observed visually in region A of Fig. 3.7(h) for ADSP. This is because the algorithm derives the smoothing strength by using the first-order nonlocal differences, namely gradients in a space of patches [51], which still cannot effectively detect the edges of low contrast blobs in region A of the noisy image Fig. 3.7(b). Our FP-NAD overcomes this problem since the 2nd-order NLD characterize the blobs better than the first-order and thus has a high response to blob features under noise contamination. The strong feature preserving ability of our method can further be attributed to the unimodal shape of 2nd-order NLD and anisotropic diffusion along the orientation of the features. Moreover, our method performs isotropic diffusion in background regions so can reduce noise more effectively than the NLM filter and induce little artifacts, compared to PM and BM3D. We have quantified the image fidelity by calculating peak signal-to-noise ratio (PSNR) [56] and mean structure similarity index (MSSIM) [108] between original and denoised images. Higher PSNR and MSSIM imply better image restoration and structure preservation, respectively. We report in Table 3.1 the PSNR and MSSIM values of denoised results shown in Fig. 3.7 by our method, PM, Catté, CED, TDCPD, ADSP, NLM filter, SAFIR and BM3D. Table 3.1 also summarizes the PSNR and MSSIM for the denoised images by the above methods on Fig. 3.7(a) with AWGN of Std $\sigma_n = 30$ and 40. As seen, our method, for different levels of Gaussian noise, achieves the highest PSNR and MSSIM value among the nine algorithms.

3.4.2.2 Denoising of a Fingerprint Image Containing Ridges

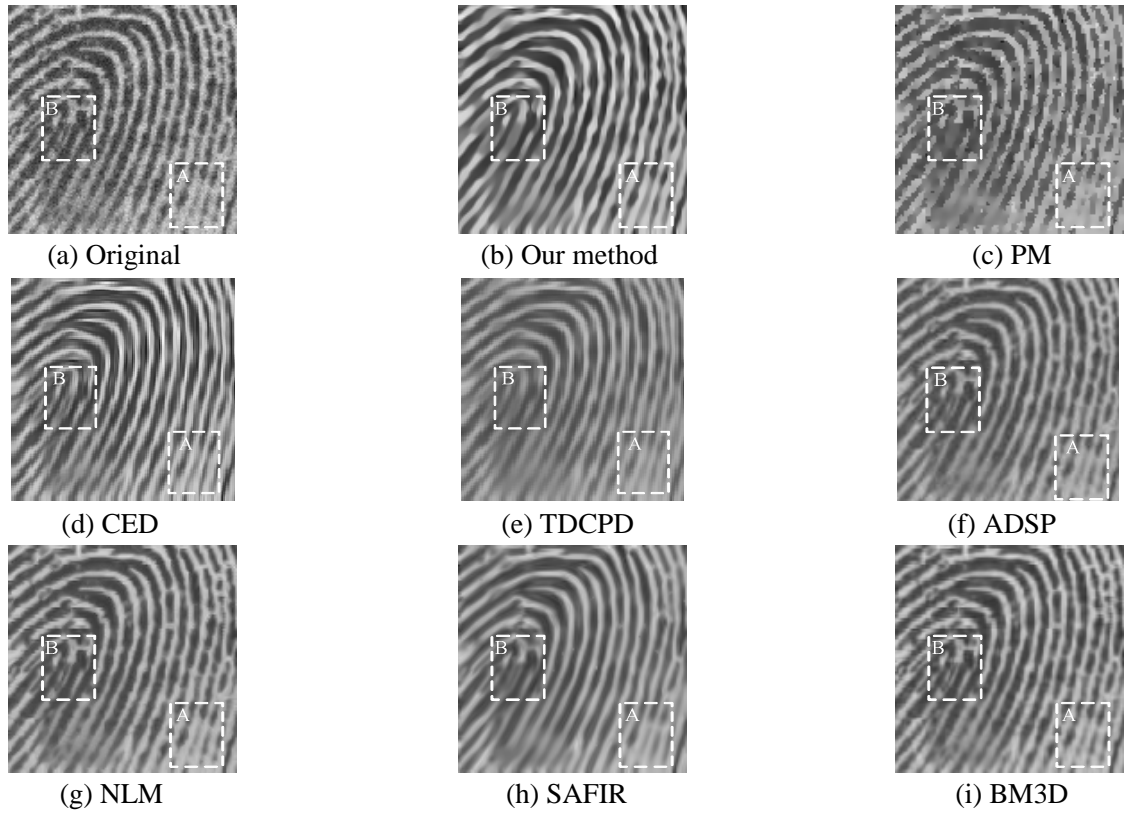


Fig. 3.8 Denoising of a fingerprint image and comparisons. (a) Original fingerprint image; (b) - (i) Denoised results by FP-NAD, PM, CED, TDCPD, ADSP, NLM filter, SAFIR and BM3D, respectively. In each image, region A and B are marked by two boxes.

This experiment is to illustrate that the FP-NAD filter can further be used to improve the quality of fingerprints containing ridge features. Fig. 3.8(a) shows an 8-bit fingerprint image from FVC 2004 in which ridges (dark lines) and valleys (bright lines) are main features. The image is corrupted by noise, breaks and smudges. An example of the latter is a short and light dark line between two ridges as shown in region B of Fig. 3.8(a). These adverse effects can seriously degrade the performance of a fingerprint recognition device. We show in Fig. 3.8(b) the result of the fingerprint image processed by the FP-NAD filter. The patch size for calculating 2nd-order NLD is 15×15 pixels, same as one used in the last test. As seen, Fig. 3.8(b) restores very well the ridges corrupted by smudges and breaks. We compare this result with those shown in Fig. 3.8(c)-(i) by PM, CED, TDCPD, ADSP, NLM filter, SAFIR and BM3D, respectively. Parameters used in the seven methods are all the same as those in the last test. As seen, while all the methods produce comparable noise-reduction, except for PM which creates speckle-like artifacts, their abilities for feature preservation vary. This can be best shown using the denoised images in the two regions marked by the boxes in Fig. 3.8.

From the original image Fig. 3.8(a), the breaks of ridges (region A) and smudges between parallel ridges (region B) result in the lost of edge information. As a result, PM and ADSP enlarges the breaks and smudges since their smoothing strengths are determined by the first-order differences in different spaces [9, 51], both of which cannot detect the lost edges due to breaks. TDCPD preserve ridges better than PM due to smoothing along the direction of ridges, but still over-smooth the features in region A since the smoothing strength is also determined by the first-order difference. The breaks and smudges also lead to lower contrast between ridges and valleys under noise contamination. NLM filter, SAFIR and BM3D hence blur the ridges in this region. The 2nd-order NLD, even when the edges of ridges are blurred or partly lost to a certain extent, can still detect them properly and therefore provides high responses in region A and B. Compared to other methods, the FP-NAD filter displays the best contrast enhancement and preservation of ridges with different widths both in region A and B. CED performs comparably with our method with respect to ridge preserving since it derives the smoothing strength by the coherence of structures in the image and the CED is therefore suited to fingerprints with repeating lines [13]. But the method gives rise to lower image contrasts than our method by comparison.

3.4.2.3 *Denoising of a Natural Image Containing Blobs and Ridges*

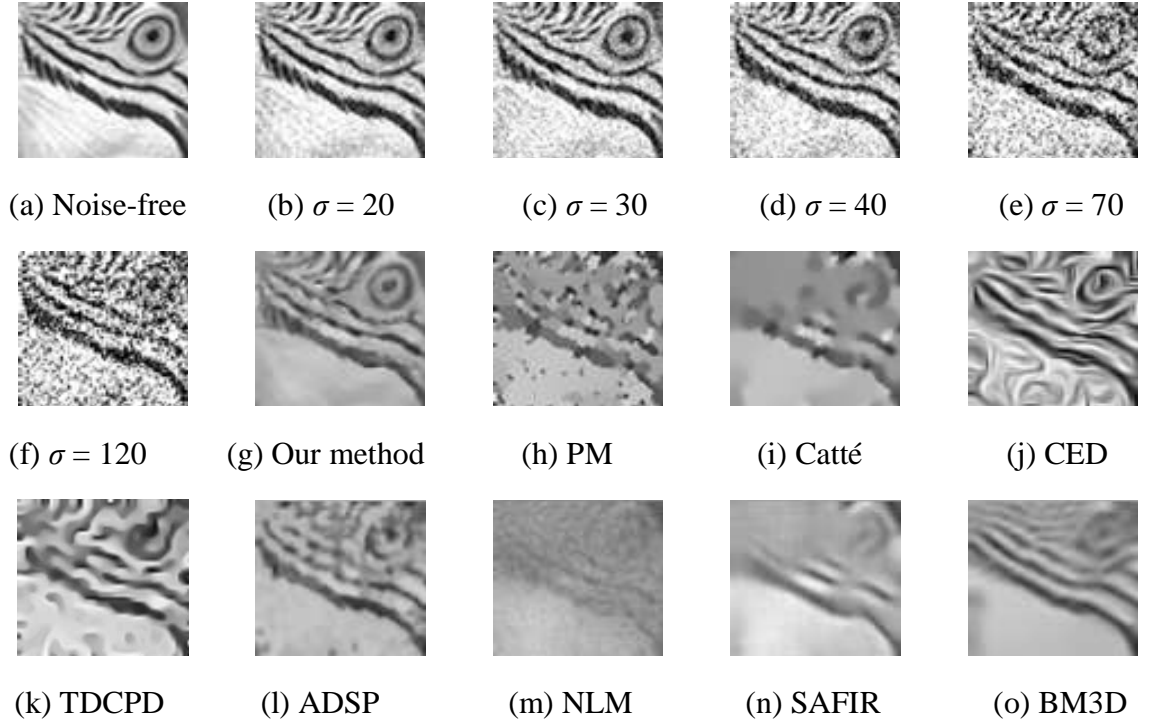


Fig. 3.9 Test on a fragment of a natural image, *Parrots*. (a) Noise-free image; (b) – (f) Images corrupted by additive white Gaussian noise with Std $\sigma = 20, 30, 40, 70$ and 120 , respectively; (g) - (o) Denoised images of (f) by our method, PM, Catté, CED, TDCPD, ADSP, NLM filter, SAFIR and BM3D on image (f), respectively.

Table 3.2

PSNR and MSSIM results on the noise-free *Parrot* image Fig. 7(a) corrupted with AWGN of Std $\sigma_n = 20, 30, 40, 70$ and 120 (Fig. 7(b) – (f)) by our method, PM, Catté, CED, TDCPD, ADSP, NLM filter, SAFIR and BM3D, the visual results of which for $\sigma_n = 120$ have been shown in Fig. 7(g) – (o), respectively.

σ_n	PSNR value (dB)/MSSIM value									
	Noisy	Our	PM	Catté	CED	TDCPD	ADSP	NLM	SAFIR	BM3D
20	22.6/0.835	26.6/0.973	24.3/0.880	24.7/0.861	24.7/0.835	24.6/0.881	24.8/0.884	23.5/0.856	26.3/0.872	26.5/0.907
30	19.3/0.729	24.2/0.957	22.3/0.813	22.4/0.784	22.6/0.827	23.14/0.831	22.7/0.841	20.4/0.762	23.5/0.801	24.0/0.852
40	17.3/0.655	22.1/0.850	19.2/0.746	19.4/0.716	19.8/0.767	19.9/0.785	20.4/0.790	18.6/0.693	21.8/0.733	21.9/0.808
70	12.9 /0.479	17.1/0.791	15.3/0.420	15.4/0.409	15.8 /0.563	15.8 /0.600	16.0 /0.612	14.6/0.367	15.5/0.415	16.0/0.537
120	8.4 /0.223	15.9/0.622	13.4/0.378	13.6/0.330	14.3 /0.507	14.8/0.497	14.8 /0.518	12.9/0.202	14.7/0.361	14.9/0.484

Finally, I test FP-NAD on a natural image that contains both blobs and ridges and are corrupted by AWGN of different noise levels. Fig. 3.9(a) shows a fragment of the noise-free benchmark image *Parrots* [101], in which the eye is of blob feature and the eye socket and stripes are ridges with different widths and orientations. The image is then corrupted by AWGN with Std $\sigma_n = 20, 30, 40, 70$, and 120 , as shown in Fig. 3.9 (b)–(f). Table 3.2 lists the PSNR and MSSIM values obtained on the denoised results of these images for different noise levels by our method, PM, Catté, CED, TDCPD, ADSP, NLM filter, SAFIR and BM3D NLM filter, SAFIR and BM3D. The parameters used are the same as those in the last test. As seen in Table 3.2, for lower noise levels ($\sigma_n = 20, 30$ and 40), our method performs slightly better than BM3D, the latter of which has higher PSNR and MSSIM values compared to the other methods. However, for higher noise levels ($\sigma_n = 70$ and 120), our method gives a noticeably better result, at least by 1dB in terms of PSNR and 0.1 in terms of MSSIM, compared to BM3D and ADSP, which for these two noise levels have highest PSNR and MSSIM values among all methods except ours, respectively. To visualize such improvement, I illustrate in Fig. 3.9 (g)–(o) the denoised images for the highest noise level ($\sigma_n = 120$). As seen, due to the severity of noise, edges in the image Fig. 3.9(f) are heavily broken, particularly in the eye region. It is therefore not surprising that PM (Fig. 3.9(h)) and Catté (Fig. 3.9(i)) are ineffective in restoring these features. PM also generates artifacts in flat regions. CED (Fig. 3.9(j)) and TDCPD (Fig. 3.9(k)) preserve stripes better than PM and Catté but noticeably distort the eye, eye sockets and stripes of parrot, and produce visually unpleasant artifacts in homogeneous regions of the parrot’s face. ADSP (Fig. 3.9(l)) preserves the eye and stripes better and introduce fewer artifacts, compared to CED and TDCPD. However, ADSP tends to spread the eye to the eye socket and break up ridges on the parrot face since it determines the smoothing strengths by the gradients, which, despite in a space of patches, can be also very low if the edges are heavily broken. The NLM filter (Fig. 3.9(m)) is the only non-iterative denoising method used here for comparison and does not seem to remove noise effectively. SAFIR (Fig. 3.9(n)), which can be seen as an iterative NLM filter with adaptive searching windows, over-smooths the whole image due to severe noise contamination. Visually, BM3D (Fig. 3.9(o)) are shown to restore the noisy image better without heavily distorting the features in the image, compared to PM, Catté, CED, ADSP and TDCPD, SAFIR and NLM filter. But it is still outperformed by the FP-NAD, as the eye, eye socket and face stripes are partly over-smoothed in comparison to the result by FP-NAD. The main reason behind the good performance of FP-NAD is again due to the good response of the 2nd-order NLD

to the features. Moreover, nonlinear anisotropic diffusion employed in our filter has the ability to effectively reconstruct the shapes of the features while remove noise.

3.5 Conclusion and Discussion

We have presented a new operator for blob and ridge feature detection and incorporated it into a diffusion model for improving denoising performance on images containing these features. We have further tested the new algorithm on synthetic live-cell images, fingerprint images and natural images and demonstrated good performance in preserving blobs and ridges, reducing background noise and minimizing artifacts.

For simplicity, I used the 2nd-order NLD operator with a single patch size (scale) to detect features with different sizes. While such a single scale 2nd-order NLD can detect blobs and ridges of different sizes around this scale, the blob size range that can be detected is limited. An improvement to our current method is to employ a multiscale feature detector that comprises several 2nd-order NLD operators with different patch sizes, in a way similar to Harr-like feature detector [113]. The number of the operators required is determined by the size range of the features under investigation. Since a single scale 2nd-order NLD operator can cover a fair wide blob size range as discussed earlier in this work, the number of 2nd-order NLD operators required in many applications should be small. For example, to cover a size range between $[10, 200]$ (in the unit of pixels), I need two 2nd-order NLD operators with patch size 21×21 and 42×42 . The implementation of the multiscale 2nd-order NLD operator is straightforward from the current model.

We note finally that the diffusion directions used in our method are the smoothed feature directions [51] determined by the eigenvectors of the popular traditional structure tensors [13, 49, 51, 100], which has shown to work well in most circumstances. It may not be sufficiently accurate for features whose directions change rapidly in space. A further improvement to our method can be made by developing the nonlocal difference concept for more robust estimation of the smoothing directions. ADSP [51] is such a method which determines the diffusion directions based on patch gradient in a high dimensional space and has shown improved PSNR compared to the NLM filter [53]. Combining ADSP with our operator is expected to further improve diffusion performance of our present method.

Chapter 4

A Generalized Feature-preserving Nonlinear Anisotropic Diffusion Method for Denoising Natural Images

Abstract: In the previous chapter, I have proposed a new diffusion method and shown its promising performance over other popular methods for denoising images containing blobs and ridge such as live-cell and fingerprint images in the biology and biometric applications. However, images captured in general environments may contain not only blob and ridge features, but also other types of features of interests, particularly in natural scenes. To denoise these natural images, in this chapter I extend our FP-NAD and propose a generalized feature-preserving nonlinear anisotropic diffusion for noise reduction and multiple feature preservation by combining first- and second-order differences for a nonlinear anisotropic diffusion model. Numerical experiments show that the new diffusion filter outperforms many popular filters for denoising natural images containing edges, blobs and ridges and textures made of these features.

4.1 Introduction

Since the edge is a fundamental feature that underlies more complicated features in the image, most of the existing diffusion methods [9, 46, 47, 114] incorporated the edge information in the diffusion process to reject diffusion at edges and permit smoothing in other places. Hence if edges cannot be distinguished due to severe noise, these methods may not be able to preserve features that are bounded by the edges. To overcome this problem, in the previous chapter I have proposed a new FP-NAD and demonstrated its promising performance over edge-preserving and other popular methods for denoising images containing blobs and ridge such as live-cell and fingerprint images in the biology and biometric applications.

Images in many other applications [115, 116] may contain not only blob and ridge, but also other features. For example, an image captured in the natural environment [117] usually consists of textures and complex patterns that are made of a combination of edges and blobs and ridges. Since the 2nd-order NLD is mathematically most correlated to blob and ridge feature, it can provide a good response only to these two features. To preserve simultaneously multiple features in the natural images, in this chapter I propose a new feature-preserving denoising method by combining the 1st- and 2nd-order NLD to form a new feature detector in a nonlinear diffusion model. By combining the 1st- and 2nd-order NLD, our new feature detector measures image intensity contrasts between neighbouring patches in a more sophisticated manner and can effectively capture fundamental features such as edges as well as blobs and ridges. We incorporate the new feature detector into a nonlinear diffusion model to form a generalized feature-preserving nonlinear anisotropic diffusion filter (GFP-NAD) for denoising the natural images. Experimental results demonstrate that the GFP-NAD can remove noise and preserve simultaneously multiple features in the natural images, compared to the FP-NAD. Experimental results also demonstrate that the GFP-NAD method can achieve a higher peak-signal-to-noise ratio (PSNR) [16] and higher mean similarity index (MSSIM) [108] than several commonly used algorithms when applied to natural images containing a range of features and textures.

4.2 A Combined Nonlocal Difference

We first define the combined nonlocal difference in a one-dimensional (1-D) signal. Extension to the two-dimensional (2-D) case is straightforward and will be discussed later. Let $I : \Omega \subset \mathbb{R}^1 \rightarrow \mathbb{R}^1$ be a 1-D scalar signal defined on the discrete domain Ω and $x_i \in \Omega$ is the pixel position, $x_i = x_1, x_2, \dots, x_N$. As discussed in the previous chapter, the edge feature is mathematically most correlated to the 1st-order difference whilst the blob and ridge features are most correlated to the 2nd-order one. Using either 1st- or 2nd-order difference may therefore not be able to provide good responses to both edge and blob/ridge features. To simultaneously detect both the edge and blob features, I define a combined nonlocal difference (CNLD) $\|\nabla_{\text{NL}}^{\text{C}} I(x_i)\|_{2,\sigma}$ in the form of

$$\|\nabla_{\text{NL}}^{\text{C}} I(x_i)\|_{2,\sigma} = w_1(x_i) \cdot \|\nabla_{\text{NL}} I(x_i)\|_{2,\sigma} + w_2(x_i) \cdot \|\nabla_{\text{NL}}^2 I(x_i)\|_{2,\sigma}, \quad (4.1)$$

where the 1st-order NLD, $\|\nabla_{\text{NL}} I(x_i)\|_{2,\sigma}$, and 2nd-order NLD, $\|\nabla_{\text{NL}}^2 I(x_i)\|_{2,\sigma}$, are given by Eq. (3.3) and (3.6), respectively. The Std σ of the Gaussian function used in Eq. (4.1) are same for the 1st- and 2nd-order NLD since the same patch size is applied for both NLDs, although the 2nd-order requires more patches than the 1st-order for differentiation. The weights $w_1(x_i)$ and $w_2(x_i)$ should be appropriately chosen for balancing the contributions of 1st-order NLD and 2nd-order NLD to the CNLD. We define $w_1(x_i)$ and $w_2(x_i)$ as functions of the 1st- and 2nd-order NLD in the form,

$$w_1(x_i) = \frac{\|\nabla_{\text{NL}} I(x_i)\|_{2,\sigma}}{\|\nabla_{\text{NL}} I(x_i)\|_{2,\sigma} + \|\nabla_{\text{NL}}^2 I(x_i)\|_{2,\sigma}}, w_2(x_i) = \frac{\|\nabla_{\text{NL}}^2 I(x_i)\|_{2,\sigma}}{\|\nabla_{\text{NL}} I(x_i)\|_{2,\sigma} + \|\nabla_{\text{NL}}^2 I(x_i)\|_{2,\sigma}}. \quad (4.2)$$

In the vicinity of an edge, $\|\nabla_{\text{NL}} I(x_i)\|_{2,\sigma} > \|\nabla_{\text{NL}}^2 I(x_i)\|_{2,\sigma}$, so $w_1(x_i) > w_2(x_i)$ and the 1st-order NLD contributes more to the DC; in the vicinity of a blob, $\|\nabla_{\text{NL}} I(x_i)\|_{2,\sigma} < \|\nabla_{\text{NL}}^2 I(x_i)\|_{2,\sigma}$, therefore $w_1(x_i) < w_2(x_i)$ and the 2nd-order NLD contributes more. As such, the CNLDs for the edge and blob features are dominated respectively by the 1st- and 2nd-order NLD. Since the 1st- and 2nd-order NLDs are mostly correlated respectively to the edge and blob features, the CNLD Eq. (4.1) can give rise to high responses to both features.

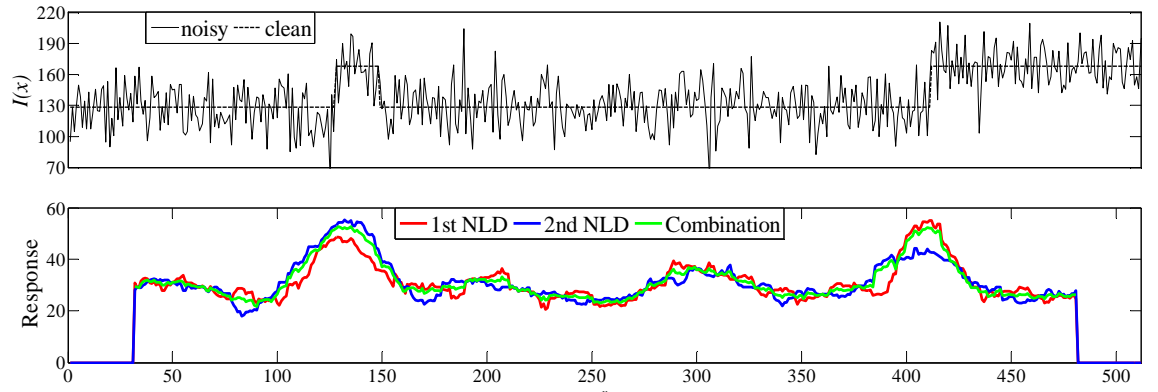


Fig. 4.1. (a) A noise-free and the noisy image corrupted by Gaussian noise; (b) The 1st- and 2nd-order NLDs and the CNLD. The 1st- and 2nd-order can give high responses to only one type of features whilst low responses to the other type. The CNLD gives high responses to the both edge and blob features.

In general, responses of the 1st-, 2nd-order NLD and CNLD to edges and blobs are complex, but the expressions can be simplified in a special case where the patch size equals the blob size, i.e., $W = s$. We use this case as an example to explain the

performance of the CNLD for detecting both edge and blob features. Fig. 4.1(a) shows a 1-D 8-bit image containing a step edge and a blob of size $s = 21$ pixels without and with additive white Gaussian noise (AWGN) of a Std $\sigma_n = 40$. Intensities of the blob and edge are set to be 160, against the background of 120. We apply Eq. (3.3), (3.4), and (4.1) on the noisy image and plot the responses in Fig. 4.1(b), where the Std of the Gaussian function is set as $\sigma \rightarrow +\infty$ so the patch window is a box one for simplicity. As seen from this figure, the responses of all NLDs to the edge contain only one obvious peak and nearly symmetric. For the step edge the peak values of the 1st-order NLD is entirely higher than that of the 2nd-order NLD, whereas for the blob the peak values of the 2nd-order NLD is higher than that of the 1st-order NLD. This is because 2nd-order NLD measures the difference of two neighbouring 1st-order NLDs. When one of 1st-order NLDs fails to detect one edge of the blob due to noise contamination, the 2nd-order NLD can still give a reasonable response if the other edge of the blob can be detected. The CNLD provides higher responses to both the edge and blob features, compared respectively to the 1st- and 2nd-order NLDs. This can be attributed to the weights $w_1(x_i)$ and $w_2(x_i)$ given in Eq.(4.2), which adaptively adjust the balance between the correlations of 1st- and 2nd-order NLD to multiple features base on the NLDs themselves that further enhance the correlations. Both edge and blob features can therefore be better identified by the new combination of the two NLDs than by the 1st- or 2nd-order NLD individually. Finally I note that in the general cases of $W \neq s$, the essential characteristics of CNLD as well as the 1st- and 2nd-order NLD for edge and blob detection remains unchanged.

4.3 Generalized Feature-Preserving Nonlinear Diffusion

Based on the CNLD Eq. (4.1) as a new feature detector, I form a novel feature-preserving nonlinear diffusion model,

$$\frac{\partial I(x, t)}{\partial t} = \text{div} \left[c \left(\left\| \nabla_{\text{NL}} I(x, t) \right\|_{2, \sigma}, \left\| \nabla_{\text{NL}}^2 I(x, t) \right\|_{2, \sigma} \right) \cdot \nabla I(x, t) \right], \quad (4.3)$$

where the diffusion coefficient (DC) $c \left(\left\| \nabla_{\text{NL}} I(x, t) \right\|_{2, \sigma}, \left\| \nabla_{\text{NL}}^2 I(x, t) \right\|_{2, \sigma} \right)$ is given as a decreasing function of the CNLD $\left\| \nabla_{\text{NL}}^{\text{C}} I(x, t) \right\|_{2, \sigma}$ in the form of

$$c\left(\left\|\nabla_{\text{NL}} I(x,t)\right\|_{2,\sigma}, \left\|\nabla_{\text{NL}}^2 I(x,t)\right\|_{2,\sigma}\right) = \exp\left[-\frac{\left(\left\|\nabla_{\text{NL}}^{\text{C}} I(x,t)\right\|_{2,\sigma}\right)^2}{h^2}\right], \quad (4.4)$$

the CNLD $\left\|\nabla_{\text{NL}}^{\text{C}} I(x,t)\right\|_{2,\sigma}$ is given by Eq. (4.1), $I(t=0) = J$ is the initial noisy image, ∇ is the gradient operator and div is the divergence operator. Since the CNLDs are high for the edge and blob features, the DCs are small in the vicinity of both features and high in the backgrounds. As such, the diffusion (smoothing) process will be discouraged considerably in feature regions and encouraged in background regions, leading to a generalized feature-preserving nonlinear diffusion (GFP-ND) method that preserves multiple features and removes noise in the background during the diffusion process. Compared to the GFP-ND Eq. (4.3), the FP-ND Eq. (3.16) proposed in the previous chapter can be seen as a special case of the GFP-ND when the weight $w_1(x,t) \equiv 0$ and $w_2(x,t) \equiv 1$ for any pixel x and time step t .

The threshold h serves as a parameter that determines whether a feature should be preserved in the diffusion process. A large h may oversmooth features whereas a small h can produce artefacts and unsatisfactory noise suppression. The choice of h should also reflect noise levels. Based on this rule, several researchers have proposed various strategies for the assignment of the h values, of which the MAD operator has been proved being the most effective one [16, 47]. In this thesis we employ the median absolute deviation (MAD) of CNLD $\left\|\nabla_{\text{NL}}^{\text{C}} I(x,t)\right\|_{2,\sigma}$ for a robust estimation of the diffusion threshold h [16, 47].

A simple way to terminate the diffusion process is by fixing the number of iterations. In this work I utilize the MSDN criterion given in Eq. (3.21) to stop the diffusion adaptively. The diffusion process stops only when the MSDN reaches to a pre-specified small value.

4.4 Experiments

In this section I present visual and numerical results obtained by using our diffusion method, first for a 1-D image and subsequently 2-D images. In the latter case I incorporate the orientation of the features into Eq. (4.3), leading to a GFP-nonlinear anisotropic diffusion (GFP-NAD) model. We test the GFP-NAD on 2-D natural images and compare the results with existing popular denoising methods, including PM anisotropic diffusion method [9], structure adaptive filter (SAFIR) [16] and block

matching and 3-D collaborative filtering (BM3D) [58]. The last method is considered to be the best denoising algorithm at present [18, 96, 118]. We have not included bilateral filter [11], which can be seen as a special case of SAFIR [16] when both the patch width and iteration number equal to 1, because reports [16, 119] have already shown that it underperforms SAFIR for denoising natural images.

4.4.1 1-D Signals

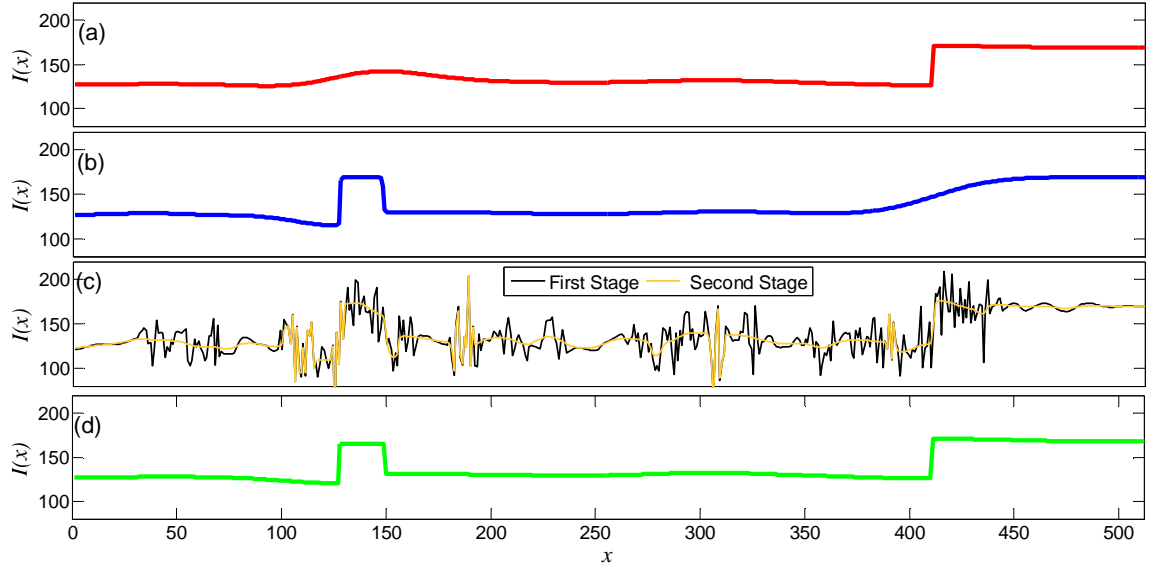


Fig. 4.2. Tests on the noisy image shown in Fig. 4.1(a). (a) Denoising result by an edge-preserving diffusion, which is a special case of the GFP-ND when $w_1(x_i, t) \equiv 1$ and $w_2(x_i, t) \equiv 0$ for any x_i and t ; (b) Denoising result by a blob-preserving diffusion, which is also a special case of the GFP-ND when $w_1(x_i, t) \equiv 0$ and $w_2(x_i, t) \equiv 1$ for any x_i and t ; (c) Results in two different stages of the diffusion process by GFP-ND, where $w_1(x_i, t)$ and $w_2(x_i, t)$ are calculated by Eq. (4.3); (d) The final denoised result by the GFP-ND.

We first test the GFP-ND filter Eq. (4.3) on the 1-D noisy image shown in Fig. 4.1(a) that has been used in Section 4.2. The patch size W is chosen as $W = 21$. The initial value of the diffusion threshold h is set to be $h = 40$, same as the Std σ_n of the AWGN in the image, and is updated using the MAD operator at each iteration. We first consider a special case of $w_1(x_i, t) \equiv 1$ and $w_2(x_i, t) \equiv 0$, for which the GFP-ND Eq. (4.3) is reduced to a conventional edge-preserving diffusion. Fig. 4.2(a) shows the results by this special case of the GFP-ND in which the step edge is preserved but the blob is

smoothed out. On the contrary, if I set $w_1(x_i, t) \equiv 0$ and $w_2(x_i, t) \equiv 1$, the GFP-ND Eq. (4.3) is reduced to the FP-ND model Eq. (3.16). Fig. 4.2(b) shows results by this method in which the blob is preserved but the step edge is filtered.

We now apply the GFP-ND to the noisy image and show the denoising results in three different stages during the diffusion process in Fig. 4.2(c) and (d). When w_1 and w_2 follow Eq. (4.2), the 1st-order and 2nd-order NLD play a dominating role respectively around edges and blobs in determining the DCs. As a result, for the initial noise image, the DCs are low in the vicinity of both features and high in backgrounds. As such, the GFP-ND smoothes more heavily on the former regions in the initial stage while leaves the regions in the vicinity of the edge and blob features essentially unchanged, as shown by the black curve in Fig. 4.2(c). As the image evolves during the diffusion process, the smoothing effect “propagates” towards the feature regions. Background regions away from the features continue to be smoothed during this period. The contrasts of the features thus become increasingly higher, giving rise to higher responses of the 1st-order and 2nd-order NLD around the edge and blob, respectively. Higher responses of 1st- and 2nd-order NLD imply higher w_1 and w_2 respectively, so the system performs in a positive feedback manner, leading to more effective noise reduction and feature preservation in the second stage, as shown in Fig. 4.2(c) (orange curve). As noise is gradually removed, the difference of the images between two adjacent iterations becomes increasingly smaller. The diffusion process stops when the MSDN is reduced to 0.01, indicating that the diffusion process has converged. As seen from Fig. 4.2(d), the final result shows good preservation of features and reduction of noise compared to the noise-free image in Fig. 4.1(a).

4.4.2 2-D Images

Edges and ridges can be directional features in 2-D images. To better preserve the geometric properties of these features, the orientations of features should be taken into account when I apply the GFP-ND filter to 2-D images. We therefore propose a spatially anisotropic nonlinear diffusion method, whereby smoothing behaviour is performed in directions parallel rather than perpendicular to the isophotes of images [52]. In this case, the scalar DC c in Eq. (4.3) should be replaced by a diffusion tensor (DT) \mathbf{D} , a symmetric and definite-positive matrix [50] and the diffusion model is formulated as

$$\frac{\partial I(\mathbf{x}_i, t)}{\partial t} = \text{div}[\mathbf{D} \nabla I(\mathbf{x}_i, t)], \quad (4.5)$$

where $\mathbf{x}_i = [x_i, y_i]^T \in \mathbb{R}^2$ is a pixel and $\nabla I(\mathbf{x}_i, t) = [\nabla_x I(\mathbf{x}_i, t), \nabla_y I(\mathbf{x}_i, t)]^T \in \mathbb{R}^2$ is a vector whose elements are gradients at the pixel \mathbf{x} along x -axis and y -axis. The DT \mathbf{D} is expressed as [50],

$$\mathbf{D}(\mathbf{x}_i, t) = \lambda_0(\mathbf{x}_i, t) \mathbf{V}_0 \mathbf{V}_0^T + \lambda_1(\mathbf{x}_i, t) \mathbf{V}_1 \mathbf{V}_1^T, \quad (4.6)$$

where the vectors $\mathbf{V}_0, \mathbf{V}_1$ and the scalars λ_0, λ_1 are the eigenvectors and eigenvalues of the DT \mathbf{D} , respectively. The vectors \mathbf{V}_0 and \mathbf{V}_1 are chosen to be the eigenvectors of the structure tensor $\mathbf{S} = G_\rho * \nabla(G_\sigma * I) \nabla(G_\sigma * I)^T$ [13, 49, 50, 52], in a same manner as that in Section 3.2.3 in the previous chapter, implying that the smoothing vector $\mathbf{D} \nabla I$ is decomposed onto one orthonormal basis with directions across and along the principal direction of features, respectively. The eigenvalues $\lambda_0(\mathbf{x}_i, t)$ and $\lambda_1(\mathbf{x}_i, t)$ of \mathbf{D} in Eq. (4.6) determine the strengths of the local smoothing behavior along the directions $\mathbf{V}_0, \mathbf{V}_1$ in a diffusion process. They are given as,

$$\lambda_0(\mathbf{x}_i, t) = c\left(\|\nabla_{\text{NL}} I(\mathbf{x}_i, t)\|_{2,\sigma}, \|\nabla_{\text{NL}}^2 I(\mathbf{x}_i, t)\|_{2,\sigma}\right) \text{ and } \lambda_1(\mathbf{x}_i, t) = \sqrt{\lambda_0(\mathbf{x}_i, t)}, \quad (4.7)$$

where the form of the dreasing function $c\left(\|\nabla_{\text{NL}} I(\mathbf{x}_i, t)\|_{2,\sigma}, \|\nabla_{\text{NL}}^2 I(\mathbf{x}_i, t)\|_{2,\sigma}\right)$ is the same as the DC in Eq. (4.4) except that the 1st- and 2nd-order NLD is now in the 2-D isotropic form of

$$\begin{aligned} \|\nabla_{\text{NL}} I(\mathbf{x}_i, t)\|_{2,\sigma} &= \sqrt{\left\| \mathbf{P}_{x_i, y_i} - \mathbf{P}_{x_i-W, y_i} \right\|_{2,\sigma}^2 + \left\| \mathbf{P}_{x_i, y_i} - \mathbf{P}_{x_i, y_i-W} \right\|_{2,\sigma}^2} \\ \|\nabla_{\text{NL}}^2 I(\mathbf{x}_i, t)\|_{2,\sigma} &= \left\| 4\mathbf{P}_{x_i, y_i} - \mathbf{P}_{x_i-W, y_i} - \mathbf{P}_{x_i+W, y_i} - \mathbf{P}_{x_i, y_i-W} - \mathbf{P}_{x_i, y_i+W} \right\|_{2,\sigma} / 4. \end{aligned} \quad (4.8)$$

The reason for designing the smoothing strength, Eq. (4.8), at different orientations follows the explanation for the FP-NAD, Eq. (3.18), in Section 3.3: In background regions Eq. (4.5) performs an isotropic smoothing due to the CNLD $\|\nabla_{\text{NL}}^{\text{C}} I\|_{2,\sigma}$ is small

and $\lim_{\|\nabla_{\text{NL}}^{\text{C}} I\|_{2,\sigma} \rightarrow 0} \lambda_0 \approx \lim_{\|\nabla_{\text{NL}}^{\text{C}} I\|_{2,\sigma} \rightarrow 0} \lambda_1 = 1$. In the vicinity of features both the smoothing

behaviours in the two directions are discouraged since $\|\nabla_{\text{NL}}^{\text{C}} I\|_{2,\sigma}$ is large. Smoothing behaviours along the direction perpendicular to the intensity isophotes is however discouraged at a higher order to better preserve the shapes of the features since

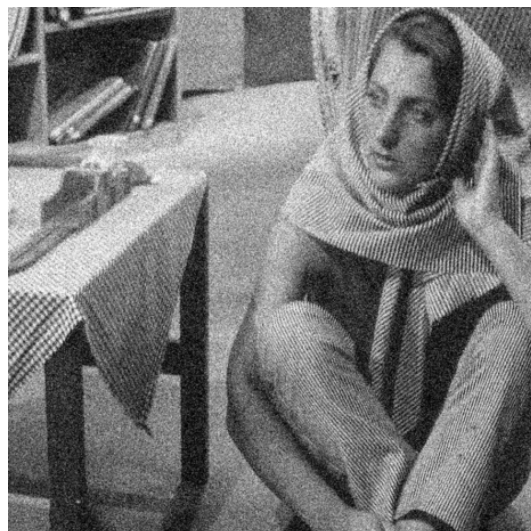
$\lim_{\|\nabla_{\text{NL}}^{\text{C}} I\|_{2,\sigma} \rightarrow +\infty} \frac{\lambda_0}{\lambda_1} = 0$. Eq. (4.5) therefore performs a nonlinear spatially anisotropic

smoothing during the diffusion process.

4.4.2.1 Denoising of a Natural Image Containing Multiple Features



(a) Noise-free image



(b) Noisy image



(c) GFP-NAD



(d) PM



(e) SAFIR



(f) BM3D



(g) FP-NAD

Fig. 4.3. A noise-free *Barbara* image; (b) The noisy image with AWGN of a Std $\sigma_n = 25$; (c) –(g) Denoised results by GFP-NAD, PM, SAFIR, BM3D and FP-NAD, respectively

We first undertake experiments on a classical image: *Barbara* (512x512). Fig. 4.3(a) and (b) shows respectively the noisy-free and noisy image with AWGN of a Std $\sigma_n = 25$. As seen, the image contains various features, including many edges, checkerboard-like and striped textures on the tablecloth and striped textures on the clothes.

We apply the generalized feature-preserving nonlinear anisotropic diffusion (GFP-NAD) filter Eq. (4.5) to the noisy image Fig. 4.3(b). The patch size for calculating 1st- and 2nd-order NLD by Eq. (4.8) is set to be 13×13 pixels, which is between the smallest and largest widths (7 to 17 pixels) of the ridges in the image. The parameter h is chosen initially to be $h = 25$, equal to the Std σ_n of the noise, and is updated using the MAD operator at successive iterations. The diffusion process stops when the MAE is less than 0.01. The denoised result by our GFP-NAD is shown in Fig. 4.3(c). As seen, all features in the image are correctly preserved by comparing to the noise-free image Fig. 4.3(a), including eyes of *Barbara*, weak striped textures on the clothes of *Barbara* and checkerboard-like textures on the tablecloth.

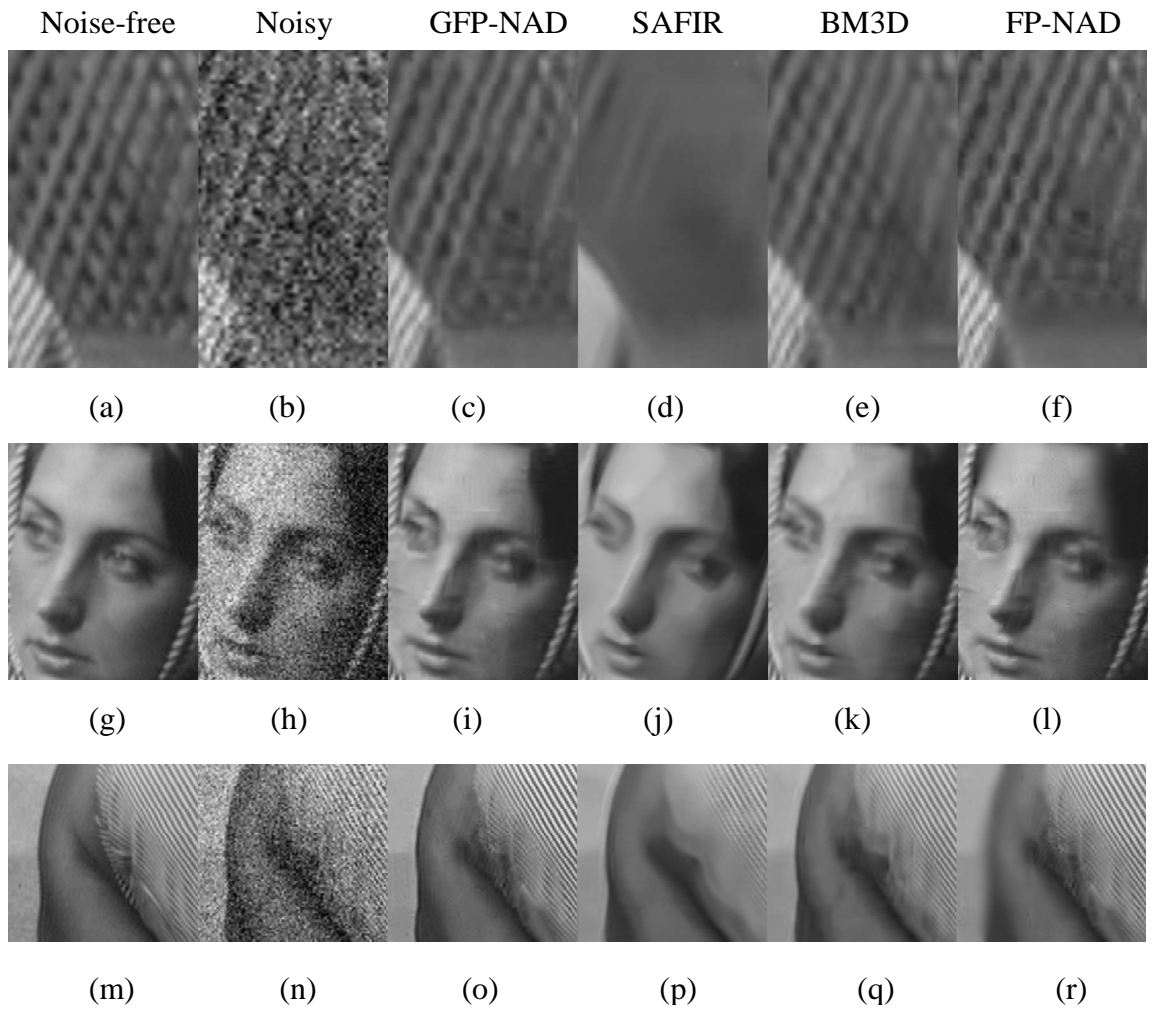


Fig. 4.4. Detail comparisons of the image *Barbara* in Fig. 4.3(a) among different denoising methods for. (a) –(f) Zoom-in images of the boxed region A for noise-free Fig. 4.3(a) and noisy image Fig. 4.3(b), and results by our method, SAFIR, BM3D and FP-NAD, respectively. (g) –(l) Zoom-in images of the boxed region B for the same noise-free and noisy image, and results by our method, SAFIR, BM3D and FP-NAD, respectively. (m) –(r) Zoom-in images of the boxed region B for the same noise-free and noisy image, and results by our method, SAFIR, BM3D and FP-NAD, respectively

The denoised results of the same image by PM, SAFIR and BM3D, are shown in Fig. 4.3(d)-(f). For PM, the time interval is set to be $\Delta t = 0.2$ and the processes stop when the MSDN is less than 0.01. In SAFIR, the patch window and the maximum number of increments for the nested window size are set respectively as 9×9 and 4 so that the highest PSNR values of the result can be obtained. The critical parameters $\lambda_{0.01} = 113.5$ is set so the ‘false alarm’ probability of terminating iterations cannot exceed 0.01. The threshold $\rho = 3$ is chosen to get a good accuracy for the point-wise estimator of the adaptive neighbouring size. More details about the parameter selection for SAFIR can

be referred to an original paper [16]. The parameters for BM3D used in all tests follow ‘Normal Profile’ in Table I in [58] .

By a visual comparison, PM significantly oversmooths the women’s face and wipes out almost all textures in the image, such as the weak striped patterns on the tablecloth and trousers. To better compare visually the denoised results, I choose three typical boxed regions of the image *Barbara* Fig. 4.3(a) and show in Fig. 4.4 respectively the zoomed-in regions of the noise-free and noisy image, the denoised results by our method, SAFIR and BM3D. As seen, SAFIR preserves the features on the trousers better than the PM, but still oversmooths the eyes of *Barbara* (compare Fig. 4.4(g) and (j)) and removes the textures on the basket (compare Fig. 4.4(a) and (d)) and trousers (compare Fig. 4.4(m) and (p)). Our GFP-NAD avoids this problem (see Fig. 4.4(c), (i) and (o)) since the CNLD provide high responses on these features under noise contamination. The strong feature preserving ability of our method is also attributed to the unimodal shape of the 1st- and 2nd-order NLD and anisotropic diffusion along the orientation of the features. Moreover, our method performs isotropic diffusion in background regions so remove noise and induce little artifacts, unlike the PM method. BM3D performs comparably with our GFP-NAD in terms of noise removal, but tends to slightly oversmooth the eyes (compare Fig. 4.4(k) and (i)) and stripes on the trousers (compare Fig. 4.4(o) and (q)) by comparison. Besides, I show in Fig. 4.3(g) the denoised result of the FP-NAD Eq. (3.16) proposed in the previous chapter, which can be seen as a special case of the GFP-NAD when the weight $w_1(\mathbf{x}, t) \equiv 0$ and $w_2(\mathbf{x}, t) \equiv 1$. The boxed-regions A, B and C of the denoised result by FP-NAD are further magnified and shown in Fig. 4.4(f), (l) and (r), respectively. By comparing Fig. 4.3(c) with Fig. 4.3(g), I find that both the GFP-NAD and FP-NAD perform well in removing noise and preserving blob and ridge features and textures made up by them. The latter, however, oversmooths most of the edge features in the image, including the boundaries between the basket and the land (Fig. 4.4(f)), the boundaries of the hairs on the woman’s face (Fig. 4.4(l)) and the boundaries of the arm (Fig. 4.4(r)). This is due to the fact that the FP-NAD uses only single feature detector (2nd-order NLD) for feature-preserving denoising. The GFP-NAD combines different feature detectors in the diffusion model, so preserves simultaneously all features in the natural images during the diffusion process. This result demonstrates that the GFP-NAD is indeed a more generalized approach for denoising the natural images, compared to the FP-NAD method.

We have quantified the image fidelity by calculating PSNR [16] and MSSIM [108] between original and denoised images. Higher PSNR and MSSIM imply better image restoration and structure preservation, respectively. We report in Table 4.1 the PSNR and MSSIM values of denoised results shown in Fig. 4.3 by GFP-NAD, PM, SAFIR, BM3D and FP-NAD. Table 4.1 also summarizes the PSNR and MSSIM for the denoised images by the above methods on Fig. 4.3(a) with AWGN of Stds $\sigma_n = 30$ and 40. As seen, our method, for different levels of AWGN, achieves the highest PSNR and MSSIM value among the five algorithms.

Table 4.1. Comparison of PSNR and MSSIM by GFP-NAD, PM, SAFIR, BM3D and FP-NAD. Three levels of AWGN with Stds $\sigma_n = 25, 30$ and 40 are tested.

σ_n	PSNR/MSSIM values					
	Noisy Image	GFP-NAD	PM	SAFIR	BM3D	FP-NAD
25	20.32 /0.406	31.22/0.901	24.47/0.71 0	27.78/0.79 0	30.73/0.88 7	27.12/0.813
30	18.79/ 0.346	30.37/0.89 2	24.03/0.63 5	26.39/0.74 8	29.76/0.86 4	25.97/0.784
40	16.49/ 0.264	28.85/0.84 3	22.16/0.51 4	24.30/0.67 4	28.07/0.82 4	23.49/0.701

4.4.2.2 Denoising of a Natural Image under Extremely Severe Noise Contamination

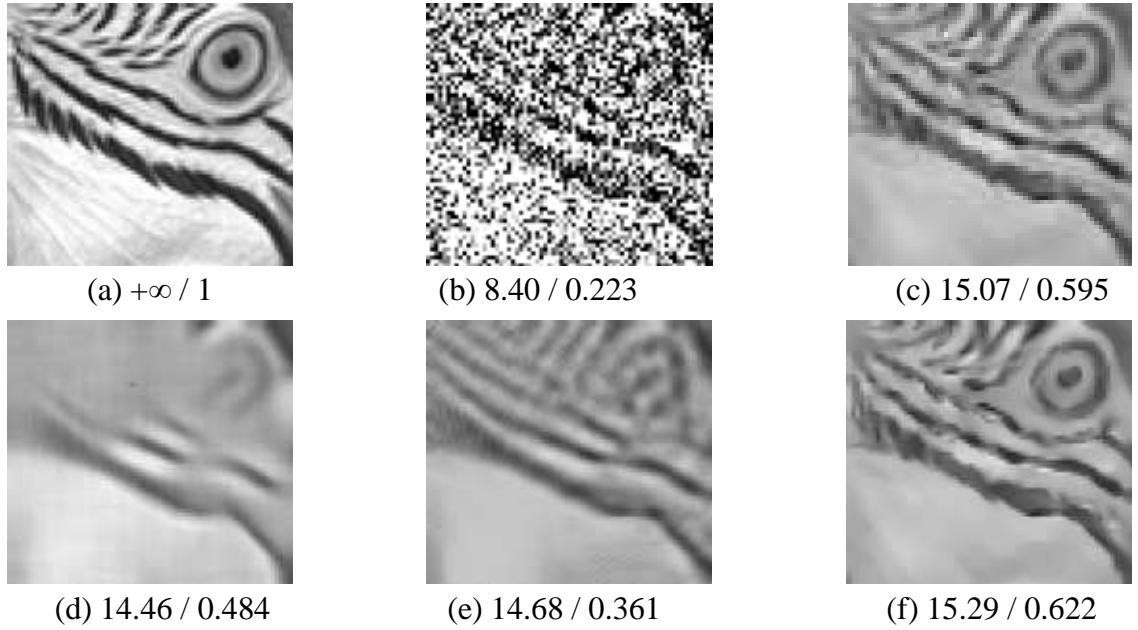


Fig. 4.5. Test on a fragment of a natural image, Parrots. (a) Noise-free image. (b) Noisy image ($\sigma_n = 120$). (c) - (f) Denoised results by GFP-NAD, SAFIR, BM3D and FP-NAD, respectively. Two numbers under each image are the corresponding PSNR and MSSIM values.

We further test the FP-NAD filter on a natural image under severe noise contamination. Fig. 4.5(a) and (b) show a fragment of a noise-free and noisy image *Parrots* [101] that has been used for testing the FP-NAD Eq. (3.16) in Section 3.4.2.3 of the previous chapter. Extremely high-level AWGN ($\sigma_n = 120$) again is used in order to test the performance limit of the GFP-NAD filter on extremely low-PSNR images. Parameters of GFP-NAD, SAFIR and BM3D are the same as those in the last test. The denoising result is shown in Fig. 4.5(c) - (e), the two numbers under each figure are the corresponding PSNR and MSSIM values, respectively. As seen, due to the severity of noise, edges in the image Fig. 4.5(b) are heavily broken, particularly in the eye region. As such, SAFIR (Fig. 4.5(d)) is ineffective in restoring these features. Visually, BM3D (Fig. 4.5(e)) are shown to preserve features better than SAFIR, but are still outperformed by the GFP-NAD (Fig. 4.5(c)), as the eye, eye socket and face stripes are partly oversmoothed in comparison to the result by GFP-NAD. The main reason behind the good performance of our GFP-NAD is again due to the combination of two feature detectors. Besides, I also show in Fig. 4.5(f) the denoised result of FP-NAD for comparison. As seen by comparing Fig. 4.5(c) with Fig. 4.5(f), I find that the GFP-NAD performs comparably with FP-NAD in terms of feature preserving and noise removing, though the PSNR and SSIM values suggest that the latter is slightly better. This is not

surprising since this image comprises predominantly blob and ridge features that can be best preserved by the FP-NAD. However, even under this situation the GFP-NAD as a general method still perform very well. This result indicates that the GFP-NAD method can be also tailored to denoise images containing mainly blob and ridge features.

4.5 Conclusions and Discussion

We have presented a generalized feature-preserving nonlinear anisotropic diffusion method in which the diffusion coefficient is constructed by not only single detector but a combination of two different feature detectors. We have tested the new algorithm on 1-D and 2-D images and demonstrated good performance in preserving multiple features and textures. It can also effectively reduce the background noise and create minimal artifacts.

A key issue in our GFP-NAD filter is the formation of DC by using two combined NLDs, which provides improved detection performance on edge, blob and ridge features. The NAD process controlled by this DC can therefore smooth out noise while preserve simultaneously multiple features in the natural images. The GFP-NAD filter are therefore a more generalized denoising method, compared to the FP-NAD that can only preserve blob and ridge features in the denoising process. We note that our work can be further extended by combining multiple feature detectors into the diffusion model. A range of choices of these detectors are already available in the fields of image processing and computer vision [110, 120-123]. These operators can therefore be used for the feature-preserving denoising in a wide range of applications.

Part II

**Super-Resolution in Fluorescence
Microscopy**

Chapter 5

Super-Resolution Fluorescence Microscopy for Cell Imaging

Abstract: I have studied a simple degradation case, noise contamination, in the first part of the thesis. In the second part, I study a more complex degradation in which the original image I is not only contaminated with noise, but also blurred due to the light diffraction and thus loses resolution during the imaging process (Fig. 1.1) in fluorescence microscopy. In such a case, the resolution of the observed image J is diffraction-limited. To break the barrier of the diffraction limit in the fluorescence cell microscope images, several modern fluorescence microscopy techniques have been proposed and currently are still being developed. In this chapter, I provide an overview of some of these modern SR microscopy techniques. Our original work for increasing the image resolution will be discussed in the next chapter.

5.1 Introduction

For century, light microscopy has revolutionized biologists' understanding of how cells function. In fact, entire fields of biology have emerged from images acquired under light microscopes [124]. With the recent development of fluorescent probes and new high-resolution microscopes, biological imaging has entered a new era and is presently having a profound impact on the way research is being conducted in the life sciences. Biologists are depending more and more on imaging; they can now visualize cellular components and processes *in vivo* both structurally and functionally;

observations can be made in two or three dimensions at different wavelengths, possibly with time-lapse imaging to investigate cellular dynamics. However, the application of fluorescence microscopy for many areas of biology is still hindered by its moderate resolution of several hundred nanometers. This resolution is approximately the size of an intracellular organelle, thus inadequate for exploring the inner architecture of many intracellular structures [125].

In general, the resolution of the fluorescence microscopy is limited by the diffraction of the light wave when it passes through a small aperture or is focused to a tiny spot. Because this property is directly related to the wavelength of light at different energies, breaking the diffraction limit of fluorescence microscopy was deemed impossible for a long time, particularly for the visible light with wavelengths ranging from 400 nm to 700 nm. However, such limitations have not deterred a small group of scientists from pursuing super-resolution (SR) fluorescence microscopy that images beyond this seemingly impenetrable limit. In the remainder of this chapter, I will briefly summarize the technological advances of these scientists in the field of super-resolution fluorescence microscopy. We will also give a short conclusion to analyze some drawbacks of these SR techniques.

5.2 Super-Resolution in Fluorescence Microscopy

When light is focused by the objective of a microscope, the notion of light rays converging to an infinitely sharp “focal point” does not happen. Instead, the light wave forms a blurry focal spot due to diffraction. This blurring spot has a finite size that depends on the wavelength of the light and the angle at which the light wave converges; the latter is, in turn, determined by the numerical aperture of the objective. As such, the width of the spot W is calculated as $W \approx 0.6\lambda / \text{NA}$, where λ is the wavelength of the light and NA is the numerical aperture of the lens. Similarly, a point emitter, such as a single fluorescent molecule also appears as a blurry spot with a finite size when imaged through a microscope. The intensity profile of this spot, which defines the point spread function (PSF) of the microscope, has approximately the same width as that of the focal spot described above. The resolution of the fluorescence microscopy is then defined by these widths, which are also called diffraction-limited resolution.

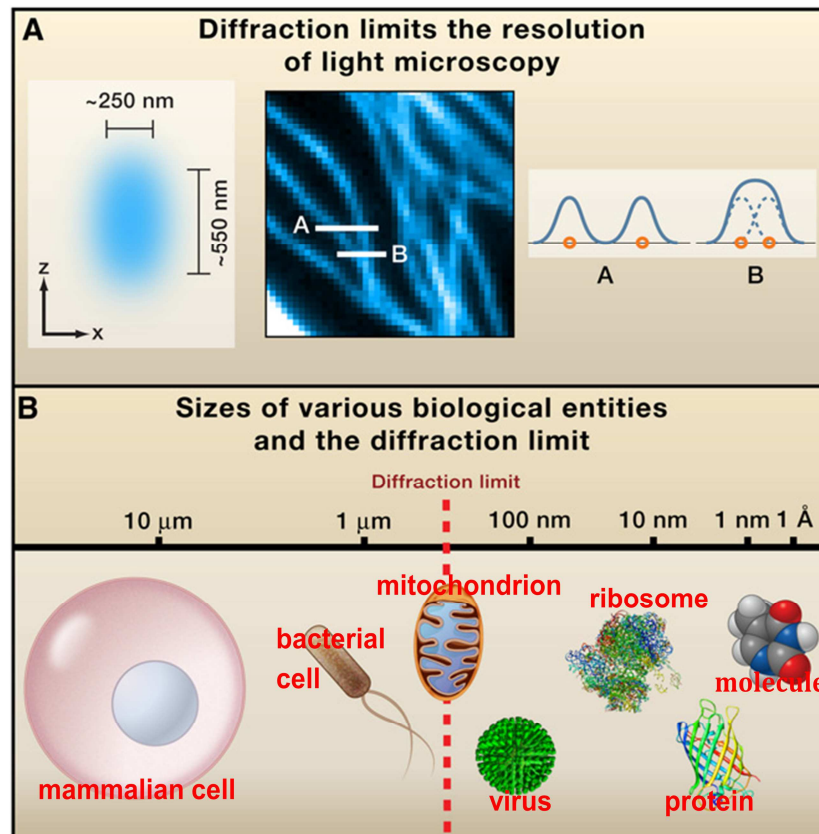


Fig. 5.1. Diffraction-limited resolution of the conventional fluorescence microscopy. (a) Left panel: for visible lights, the diffraction limit of microscopes with high NAs is ~ 250 nm in the lateral directions and ~ 550 nm in the axial directions. Middle panel: a LR microtubule image captured by a conventional fluorescence microscope. Right panel: intensity curves of the two cross sections at the corresponding positions indicated by white lines A and B in the image of the middle panel. (b) Sizes of various biological structures in comparison with the diffraction-limited resolution. From left to right: a mammalian cell, a bacterial cell, a mitochondrion, an influenza virus, a ribosome, the green fluorescent protein, and a small molecule (thymine).

The diffraction limit of the resolution was firstly recognized by Abbe [24] about 150 years ago, and is also called the Abbe limit. For a visible light, the diffraction-limited image resolution of an objective len with a high numerical aperture is ~ 250 nm perpendicular to the direction of light propagation (i.e., in the lateral dimensions) and ~ 550 nm parallel to the direction of light propagation (i.e., in the axial dimension), as shown in the left panel of Fig. 5.1(a). Consequently, two identical emitters separated by a distance less than the width of the PSF will appear as a single object, making them

appear as a single entity (i.e., unresolvable). Such case is illustrated in the middle panel of Fig. 5.1(a), which shows a LR microtubule image captured by a conventional fluorescence microscope. We mark two white lines on two microtubules in the image and plot in the right panel two cross sections of the microtubules at positions indicated by the white lines in the LR image. As seen, the two nearby microtubules in the curve A locate farther than the diffraction limit and can be discriminated. In the curve B they are however too close to be resolved. Fig. 5.1(b) shows comparisons between the diffraction-limited resolution and sizes of various biological structures, including a mammalian cell, a bacterial cell, a mitochondrion, an influenza virus, a ribosome, the green fluorescent protein, and a thymine, the last five of which are intracellular structures that attract biologists' broad attention. As seen, these intracellular structures are smaller than these resolution limits and thus cannot be observed by conventional fluorescence microscopes. Super-resolution (SR) imaging, therefore, refers to imaging that exceeds the resolution limit to resolve these intracellular structures in the fluorescence microscopy.

5.3 Current Super-Resolution Fluorescence Microscopy Techniques

For many years, several imaging techniques have pushed the boundary of the diffraction limit of fluorescence microscopy. Among these methods, confocal microscopy and multi-photon fluorescence microscopy not only enhance the image resolution, but also reduce the out-of-focus fluorescence background, allowing optical sectioning and thus three-dimensional imaging. In addition, infrared light experiences a lower amount of scattering from tissues, allowing deep tissue imaging with two-photon microscopy [126]. 4π microscopy and I^5M use two opposing objective lenses to increase the effective numerical aperture of the microscope and thereby improve the image resolution [127-129]. Although these methods significantly improve the resolution, they are still fundamentally limited by diffraction and have, in practice, achieved resolutions of ~ 150 nm in all three dimensions [128].

The diffraction-limited resolution applies only to light that has propagated for a distance substantially larger than its wavelength (i.e., in the far field). Therefore, one route to bypass this constraint is to place the excitation source or detection probe (usually an optical fiber, a metal tip, or simply a small aperture) near the sample (i.e., in the near field) [130]. Indeed, near-field microscopy has achieved resolution substantially below 100 nm [131-133]. However, the requirement that the excitation

source or detection probe be physically close to the target object (often within tens of nanometers) has made it difficult to look into a cell or a piece of tissue with near field microscopy, limiting the applications of this technique in biology.

It was not until recently that several novel fluorescence microscopy approaches completely go beyond the diffraction limit of image resolution in the far field. In general, all of these approaches generate SR images by using the physical properties of fluorescent probes to distinguish emissions from two nearby molecules within a diffraction-limited region. These super-resolution approaches can be divided into two primary categories. The first category is hardware-based, aiming to reduce the point spread function (PSF) by employing optical patterning of the excitation and a nonlinear response of the sample. This category includes stimulated emission depletion (STED) microscopy [134, 135] and the related RESOLFT technology [136], as well as saturated structured illumination microscopy (SSIM) [137]. The second category takes advantages of single-molecule imaging, using photoswitching or other mechanisms to stochastically image single PSFs separated in time, calculating the positions of the single molecules to give rise to the signals with a precision substantially better than the diffraction limit. This second class includes stochastic optical reconstruction microscopy (STORM) [138], photoactivated localization microscopy (PALM) [139] and fluorescence photoactivation localization microscopy (FPALM) [140].

5.3.1 Hardware-based SR Fluorescence Microscopy

In the hardware-based approach, a patterned field of light is applied to the sample to manipulate its fluorescence emission. This spatial modulation can be implemented either in a positive or negative manner. In the positive case, the light field that is used to excite the sample and generate fluorescence is directly patterned. In contrast, the negative patterning approach seeks the help of an additional patterned light field to suppress the population of molecules that can fluoresce in the sample. In both approaches, the spatial information encoded into the illumination pattern allows neighboring fluorophores to be distinguished from each other, leading to enhanced spatial resolution.

5.3.1.1 Negative Patterning: STED Microscopy

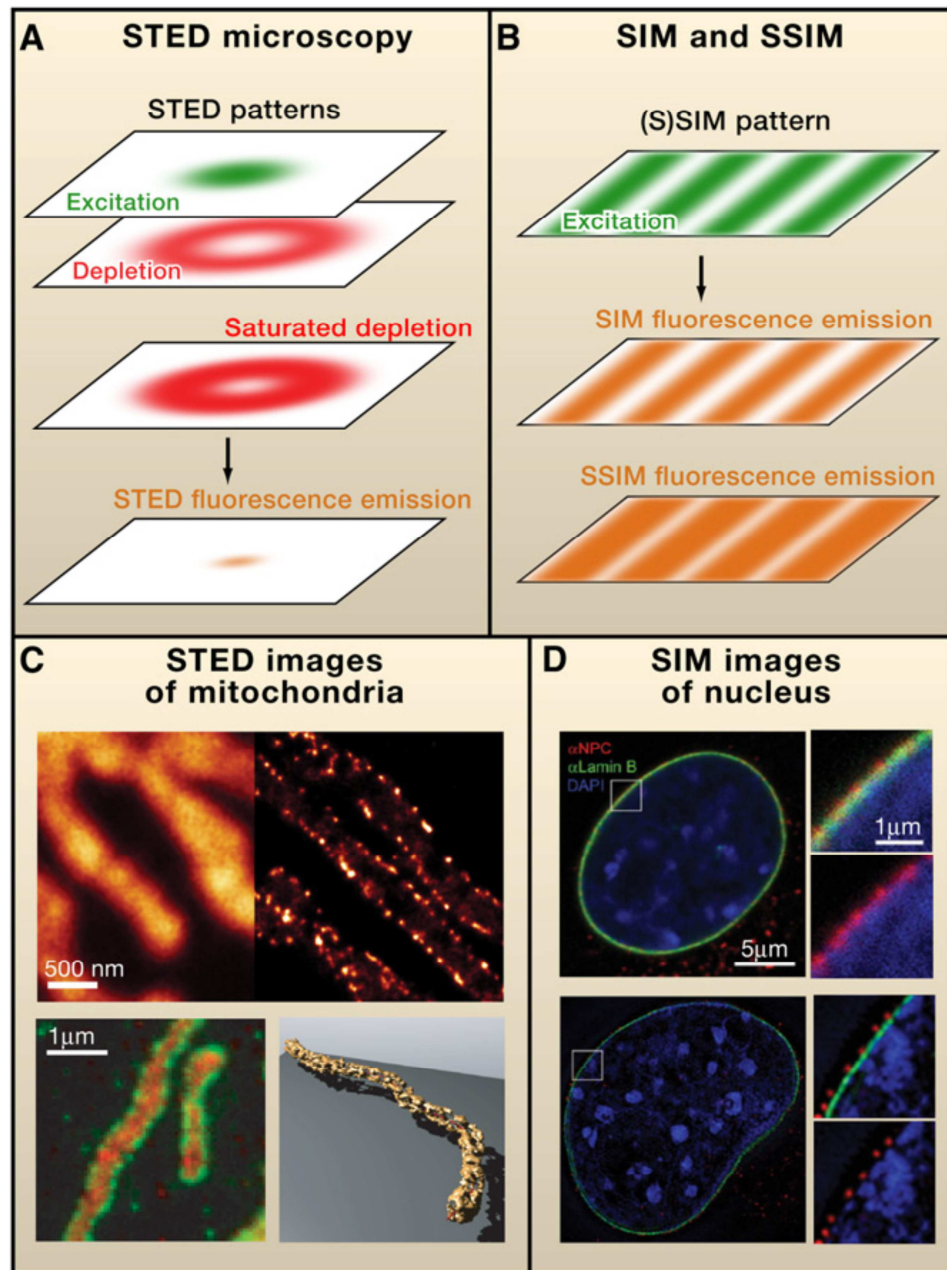


Fig. 5.2. (a) A systematic schema of stimulated emission depletion (STED) microscopy, which reduces the size of the fluorescent spot (orange, bottom layer) and improves the image resolution. (b) A systematic schema of structured illumination microscopy (SIM) and saturated SIM (SSIM), which use patterned illumination to excite the sample and saturate the fluorescence, providing spatial information substantially beyond the diffraction limit. (c) Examples of STED images. Top panel: comparison between confocal (left) and STED (right) images of the outer membrane of mitochondria that is immunolabeled against the protein TOM20 [141]. Bottom-left panel: two-color isoSTED image of TOM20 (green) and the matrix protein HSP70 (red). Bottom-right panel: three-dimensional rendering of an isoSTED image of TOM20 [142]. (D) Examples of 3D SIM images [143]. Top panel: a central cross-section of a confocal

image of the nucleus stained for DNA (blue), lamin B (green), and the nuclear pore complex (red). Bottom panel: 3D SIM images of a similarly stained nucleus.

In STED microscopy, the patterned illumination prevents fluorophores from emitting light [134, 135, 144]. This suppression is achieved by the stimulated emission, a process in which a light source, called the depletion light (the second layer of Fig. 5.2(a)), brings an excited fluorophore (the top layer of Fig. 5.2(a)) down to the lowest energy state (i.e., the ground state) before it can emit fluorescence signal. STED microscopy takes advantage of the saturated response of fluorophores: once the depletion laser intensity is above the saturation level, the number of fluorophores remaining in the excited state (and thus capable of generating fluorescence) approaches zero. Thus, when a ring-shaped depletion light pattern with peak intensity significantly above the saturation level is applied to the sample, only the molecules within a small region near the center of the ring can generate fluorescence (bottom panel of Fig. 5.2(a)), giving rise to a sharpen PSF for a SR image. The full-width-at-half maximum (FWHM) of PSF, and thus the resolution of the microscope, scales approximately with the inverse square root of the intensity of the depletion light [144].

Theoretically, STED could produce unlimited resolution improvement if an infinitely strong depletion light source is given. In practice, however, a number of factors influence the resolution of STED microscopy, including aberrations in the optics, scattering from the sample, and the photostability of the fluorophores. STED microscopy has reached a remarkable resolution of 6 nm using strong depletion intensity to image fluorescent defects in diamonds, which almost never photobleach [145]. In biological applications, STED imaging has achieved a resolution of 20 nm when using organic dyes and 50–70 nm resolution when using fluorescent proteins [146]. The upper panel of Fig. 5.2(c) shows a comparison between a confocal and a two-color STED image of the mitochondrial outer-membrane protein TOM20 and matrix protein HSP70 [141].

The STED microscopy is also used for 3-D imaging. Since a ring-shaped pattern light in the XY plane improves the lateral resolution, a pattern having two maxima along the z axis improves the axial resolution [128]. Overlaying these two patterns improves the resolution in both lateral and axial directions [147], allowing 3D SR imaging with a axial resolution ~ 2.5 times the lateral one. The lower panel in Fig. 5.2(c) [142] shows a 3-D SR image of mitochondria acquired by using isoSTED [142] with the 4π configuration, achieving a resolution of ~ 30 nm in all three dimensions.

In addition to stimulated emission, other saturable optical transitions that send the molecule to dark states can also be used to shrink the area of molecules that fluoresce in a focal spot [136]. This extension of the STED approach, called reversible saturable optically linear fluorescence transitions (RESOLFT) microscopy, allows super resolution to be implemented with a substantially lower-depletion light intensity, causing less damage to delicate biological samples [144].

5.3.1.2 Positive Patterning: Structured Illumination Microscopy

Structured illumination microscopy (SIM) improves image resolution by using positive patterning of the excitation light [27], which is typically a sinusoidal pattern created by combining (i.e., interfering) two light beams. As a result, an image snapshot of the sample becomes the product of the sample structure and this excitation pattern, as shown in Fig. 5.2(b). A final image is then computationally reconstructed from multiple snapshots collected by scanning and rotating the pattern. In this process, the additional spatial modulation from the excitation pattern brings enhanced spatial resolution into the reconstructed image [148]. However, the illumination pattern created by interference is also limited by diffraction. Therefore, when the fluorescence signal scales linearly with the intensity of the excitation light, SIM results only in a doubling of spatial resolution (Fig. 5.2(b)), which is ~100 nm in the lateral dimensions [148]. Fig. 5.2(d) shows respectively a three-color confocal and SIM image of the nucleus containing DNA (blue), lamin B (green), and the nuclear pore complex (red) [143].

Like with the STED approach, the saturating response of the fluorophore can also be exploited here to further enhance the resolution [137, 149]. With sufficiently strong excitation, the fluorescence emission from a fluorophore will saturate. Saturated SIM (SSIM) utilizes this phenomenon to create sharp dark regions where the excitation pattern has zero intensity, providing image resolution significantly beyond the diffraction limit, as shown in the lowest panel of Fig. 5.2(b). With this approach, a resolution of ~50 nm has been obtained for imaging fluorescence microspheres [137].

5.3.2 Single Molecule Localization Microscopy

After 20 years of development in the field of single-molecule imaging [150], single fluorophores are now routinely detected in a variety of imaging modalities, such as epifluorescence, total-internal-reflection, confocal, and multiphoton microscopies. Once each fluorescent probe in a sample can be imaged individually, its positions can be

determined to a high precision by finding the center of the single-molecule image [151, 152]. The uncertainty in determining the molecule's position (i.e., the localization precision) scales approximately with the inverse square root of the number of photons detected from the molecule. For bright fluorescent dyes, about one million photons can be detected from a single molecule, leading to a localization precision of ≤ 1 nm [151, 153].

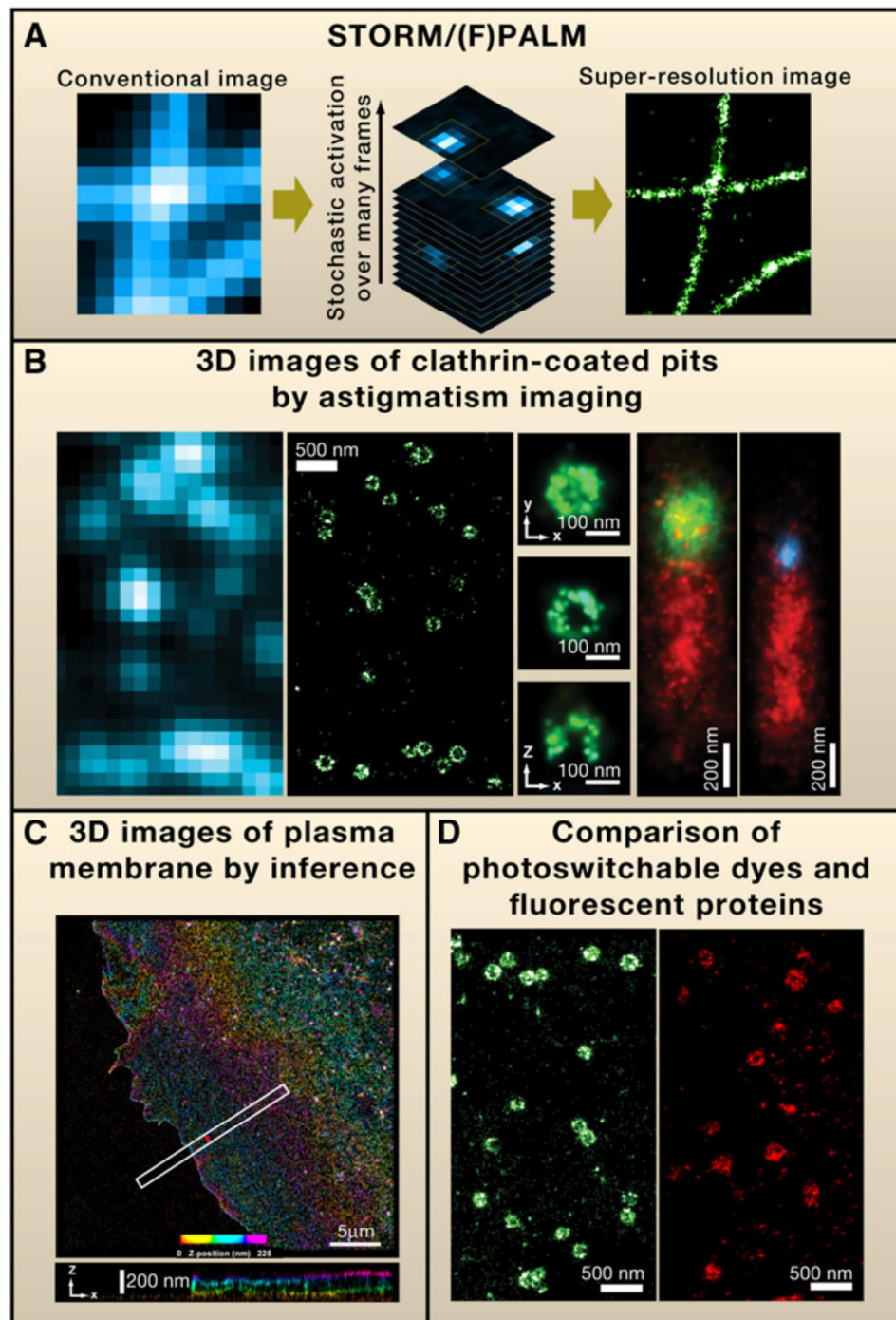


Fig. 5.3 (a) A systematic schema of STORM/(F)PALM. (b) 3D super-resolution images taken using an astigmatism approach with cylindrical lens [154, 155]. Two left panels: a

a conventional LR image of clathrin-coated pits and the corresponding 3-D SR image showing an XY cross section near the plasma membrane. Middle panel: magnified SR images of a single clathrin-coated with an XY projection (top), an XY cross-section at the lower portion of the pit (middle), and an XZ cross section cutting through the middle of the pit (bottom). Two right panels: multicolor 3-D image of clathrin (green), dynamin (cyan), and an F-BAR domain protein FBP17 (red) in the cell-free system. (c) 3-D SR images taken using an interferometry approach with apposing objectives [156]. Top: XY projection of the plasmamembrane of a cell, where the color encodes their Z coordinates. Bottom: XZ cross section of the boxed region in the top panel. (D) Comparison of STORM/(F)PALM images [155] of clathrin-coated pits immunostained with the photoswitchable Alexa647 dye (green) or tagged with the mEos2 fluorescent protein (red).

However, being able to localize a single molecule cannot directly generate super-resolution imaging of a biological sample, which can contain thousands of fluorophores inside of the diffraction-limited region. At first sight, it might seem impossible to distinguish these molecules individually. However, if the fluorescence emissions from these molecules are controlled so that only one molecule is emitting at one time, individual molecules can then be imaged and localized. This is the idea behind a recently developed super-resolution imaging technique called single molecule localization microscopy (SMLM), including STORM [138], PALM [139], and FPALM [140]. In this technique, photoswitchable (or photoactivatable) fluorophores are used to achieve temporal control of the emission. These fluorophores can be converted between a fluorescent (or “on”) state and a dark (or “off”) state or states that fluoresce at different wavelengths. Therefore, when activation light of a sufficiently low intensity is applied to the sample, only a random, sparse subset of fluorophores is activated to the on state at any time, allowing these molecules to be imaged individually, precisely localized, and then deactivated by switching to a reversible dark state or permanent bleaching. Iterating this process then allows the locations of many fluorophores to be mapped and a super-resolution image constructed from these localizations, either with synchronized activation [138-140] or with asynchronous activation [157]. Fig. 5.3(a) shows a systematic schema of SMLM. The image resolution is then no longer limited by diffraction but instead by how precisely each fluorophore is localized. Using this approach, a lateral image resolution as high as ~20 nm has been achieved [138].

By determining the position of individual molecules in all three dimensions, SMLM can be extended to 3-D imaging. The first implementation of this approach uses a simple optical design that takes advantage of astigmatism in which light propagating in perpendicular planes has different focal points. Specifically, a cylindrical lens is inserted in the imaging path, such that the shape of a single-molecule image becomes elliptical. This makes it possible to determine the axial position of the molecule from the ellipticity and the lateral position from the center position of the image [155]. Fig. 5.3(b) shows 3D images of clathrin-coated pits taken with this approach, resolving the nanomorphology of these structures [155]. Other implementations have utilized a variety of 3D localization methods, such as capturing defocused images at two different focal planes [158], engineering a PSF with a double-helical shape [159], and using a mirror to project the axial view to the lateral direction [160]. Axial resolutions of 40–70 nm have been reported using these methods. The highest axial resolution is achieved by interferometry using two opposing objectives in a similar fashion to 4π microscopy and I^5M [156]. Fig. 5.3(c) shows the clear separation of the ventral and dorsal plasma membrane in a thin protrusion of the cell using this method, demonstrating an axial resolution of 10 nm [156]. The imaging depth of this approach is relatively small compared to the PSF-fitting approaches described for the other 3-D SMLMs.

An important issue in SMLM is the choice of fluorescence probes. SMLM often uses fluorescent proteins to label the cell samples. However, for some specific experiments, the decision of whether to use dyes or fluorescent proteins for labeling depends on a variety of factors. In terms of labeling, fluorescent proteins are genetically encodable, allowing proteins in living cells to be readily labeled with fluorescent proteins. However, dyes are more versatile for labeling different molecular species, including proteins, nucleic acids, oligosaccharides, and even small molecules. In terms of the optical properties, dyes generally have a significantly higher photon output, allowing higher image resolution than fluorescent proteins. Fig. 5.3(d) shows a comparison of STORM images of clathrin-coated pits immunostained with the photoswitchable Alexa647 dye (green) and tagged with the mEos2 fluorescent protein (red) [155].

5.4 Summary

SR fluorescence microscopy has shown great promise for studying biological structures and processes from the cellular to macromolecular scale. Images obtained

from new SR imaging approaches enable scientists to directly visualize biological samples at the nanometer scale and complement the insights obtained through traditional molecular and cell biology approaches. In this chapter I have outlined some of most important SR fluorescence microscopy techniques, which can be categorized as hardware-based one and SMLM. Although these two categories of methods use different approaches to accomplish sub-diffraction resolution, these techniques share important commonalities. In both cases, a physical or chemical property of the fluorophore is used to maintain neighboring molecules in different states (i.e., “on” and “off”), enabling them to be resolved from each other [144].

Although having achieved remarkable performance in sub-diffraction-limit imaging, these SR fluorescence techniques have their limits, which include not only high cost, instrumental complexity and tardy commercialisation, but also the fact that each method has its own practical disadvantages. STED microscopy requires the use of special fluorophores and sophisticated multi-wavelength laser sources. The resolution that STED has achieved for biological samples is typically 50 to 100 nm. PALM needs the specimen to be frozen through many cycles, each cycle consisting of activation and then imaging to the full bleaching of a subset of photo-protein molecules. Stochastic methods such as STORM and SIM are slow and computationally intensive and do not provide as large an improvement in resolution as the previous methods, at least with the available linear optics. There is currently still no ideal system that offers user-friendly, high-speed, 3-D and multicolor imaging with nanometer-level spatial resolution.

Chapter 6

Feature-Preserving Super-Resolution Restoration for Fluorescence Microscopy

Abstract: In the previous chapter, I have reviewed several current SR techniques in the fluorescence microscopy for cell imaging. All of these approaches use the properties of the fluorophore to make certain special and complex imaging arrangements to achieve super resolution. In this chapter I propose an alternative approach, HR image restoration, to increase image resolution beyond the diffraction limit. It is a post image acquisition computational technique, which restores a HR image by using multiple LR observation through an inverse process. A major advantage of HR restoration method is minimal hardware modification to standard microscopes and therefore low cost. The method can also apply to many circumstances where access of specialist SR imaging devices is not possible. Commonly used HR restoration methods incorporate the edge information in the inverse process to achieve a good balance between noise removal and resolution recovery of features in the image. However, such methods have a limited effect in modelling complex features in fluorescence cell images and may not be able to restore these features and therefore restore the desired image resolution. To overcome this problem, I propose a new feature-preserving HR restoration method by incorporating the combined nonlocal difference (NLD), which has been proven effective for feature preserving in our work on image denoising, into the process of resolution restoration. Experimental results demonstrate that our method outperforms several popular HR restoration methods for noise removing and feature preserving (and resolution restoring) when applied to both synthetic and real natural images. When implemented with conventional microscopes, our method results in a ~ 7 -fold increase in the lateral spatial

resolution in noisy biological environments, delivering multi-colour image resolution of ~30 nm.

6.1 Introduction

Image resolution in the biological fluorescence microscopy, as discussed in the previous chapter, is often hindered by the standard diffraction limit. Two main approaches have been developed for breaking this limit in fluorescence microscopy and achieved remarkable resolution improvement. SR imaging devices such as STED usually involves complex optical and chemical design and therefore high costs.

An alternative approach for SR imaging is to apply image processing techniques to restore a high resolution image or sequence from a set of low-resolution observations, referred to as HR image restoration [20]. As discussed earlier in Chapter 1, the LR observations can be considered the outcomes of a degrading process of the HR images due to blurring and noise effects, as shown in Fig. 1.1 and formulated by Eq. (1.1), when the blurring matrix \mathbf{P} is no longer unitary. Compared to the image denoising, HR restoration is a more complicated inverse problem which is required to not only remove noise but also restore fine structures that are lost in the image degrading process. It is a post-acquisition method that does not depend on imaging systems by which the LR observations are recorded. However, the relative position (correspondence) between these observations must be known.

As a cost-effective method for increasing image resolution, researchers over the last decades have devoted substantial efforts to develop effective algorithms, ranging from optical flow HR restoration [23], transform-domain HR restoration [161, 162], projection onto convex sets HR [163], adaptive filtering HR [22, 164], to MCMC-blind HR [165] and so on, in order to solve the HR restoration as an inverse problem. The HR restoration approach has already been applied to many applications, such as space imaging [33], security surveillance [166] and mobile cameras [167], where the images are usually captured in a high-SNR condition. In biometrics, it has significantly improved the performance of face and iris recognition [168]. Recently, there have been increasing research activities of HR restoration methods to produce SR medical imaging, such as functional magnetic resonance imaging (fMRI) [169, 170] and positron emission tomography (PET) [171]. When applied in fluorescence microscopy, in which the resolution limitation is mainly due to light diffraction, HR restoration means SR restoration.

Medical imaging usually uses highly controlled illumination sources to avoid tissue or organ damages to a human object. Moreover, image acquisition duration has to be restricted in order to release patient discomfort and minimize imaging artifacts due to the uncontrolled patient movement. The low level of light flux leads to limited signal to noise (SNR) images. Removal of noise is therefore indispensable and critically important to the performance of HR restoration in medical imaging [172]; otherwise the noise may be amplified during the HR restoration, giving rise to unpleasant artifacts in the restored images. However, there exists a tradeoff between noise removal and feature preservation (and resolution restoration); over-smoothing can impede on image resolution that can be restored and lead to artifacts in the restored images. Hence a successful HR restoration method must comprise a built-in feature-preserving noise reduction algorithm. This is often achieved by incorporating a prior model or function, which detects the features of interests, into the inverse process. Similar to image denoising problem, previous methods for SR restoration problem usually employs a prior model based on edge-preservation concept in medical and other applications [173]; features are restored as long as all the edges are preserved in the inverse process. Particularly in medical imaging, several prior models [162, 174, 175] using gradient operators were employed for simultaneously removing noise and preserving features.

To the best of our knowledge, the HR restoration approach has not been developed for SR fluorescence microscopy in biological applications. In microscopy imaging there always exists a compromise between image quality and cell viability. Excitation of fluorescent probes causes photo-bleaching and photo-toxicity, which limit the light intensity and exposure times that can be used. The requirement to image fast and in multiple dimensions to capture dynamic intracellular events also constrains illumination and exposure regimes and requires fast camera readout. All these lead to low-SNR fluorescence imaging as in medical imaging. Compared to medical imaging however, biological images are more challenging in terms of image complexity and feature size compared to medical images. The latter usually contain data describing tissues with simpler structures and larger size compared to the former, typically 2-3 times smaller than the resolution limit of the images [176]. Fluorescence images of intracellular structures often contain abundant, heterogeneous blob and ridge-like features, complex sub-cellular structures, potentially 10 times smaller than the resolution limit [37]. In general, edges embedded in small and complex features, as having been demonstrated by the poor performance of the edge-based denoising methods [177, 178] in Chapter 3

and Chapter 4, are rather prone to noise contamination. As such, HR restoration based on edge-preservation may not perform well in fluorescence microscopy.

In Chapter 4, I have demonstrated the excellent performance for image denoising by using the GFP-NAD method that combines 1st- and 2nd-order NLDs as a feature detector [178]. Inspired by the success of NLDs in image denoising that can be seen as a simplified case of SR restoration with the unitary blurring matrix \mathbf{P} in Eq. (1.1), I in this chapter propose a new prior model that combines the 1st- and 2nd-order NLDs. The new prior function is then incorporated into an energy function to invert the imaging process by using optimization algorithms to form a feature-preserving SR restoration (FP-SR) method. When I apply the FP-SR in fluorescence microscopy, the LR images are acquired by a conventional fluorescence microscope whilst translating the microscopes in the XY plane. We refer to the combination of such a multiple LR image acquisition modality with our SR restoration method as translation microscopy (TRAM) for super-resolution imaging, which can be in principle operated in any standard microscopes with few hardware modifications. Experimental results on synthetic images demonstrate that our method can achieve a higher PSNR compared to several popular SR restoration methods [174, 179, 180]. When tested to the real fluorescence microscopic images, our method achieves a ~7-fold increase in lateral spatial resolution in noisy biological environments, delivering multi-colour image resolution of ~30 nm.

6.2 Feature-Preserving SR Restoration

6.2.1 SR Restoration by Optimization of an Energy Function

A low resolution (LR) image, \mathbf{J}_l , can be considered as the outcome of an original high resolution (HR) image, \mathbf{I}_l , after an image-degrading process involving blurring and noise contamination, where l denotes image index. This process has been illustrated in Fig. 1.1 and can be formulated by the image capturing model [179, 181],

$$\mathbf{J}_l = \mathbf{P}_l \mathbf{I}_l + \mathbf{N}_l, \quad (6.1)$$

where the column vectors \mathbf{J}_l and \mathbf{I}_l comprise respectively row-wise concatenations of the LR and HR images, \mathbf{P}_l is a blurring matrix determined by the PSF of the imaging system and \mathbf{N}_l represents additive white Gaussian noise (AWGN). Given Eq. (6.1), SR restoration aims to recover the HR image \mathbf{I}_l beyond the diffraction limit from the LR

observation \mathbf{J}_l . Theoretically, by multiplying the inverse \mathbf{P}^{-1} of the matrix \mathbf{P} on both sides of Eq. (6.1), the HR image \mathbf{I}_l can be easily and uniquely determined. However, for a fluorescence microscopy where the PSF of each pixel is almost identical, the blurring matrix \mathbf{P} cannot have a full rank and is not invertible [173]. Hence \mathbf{I}_l cannot be uniquely determined by directly inverting \mathbf{P} . Instead, it can be estimated by adapting an optimization approach by minimizing a pre-defined energy function [181],

$$\begin{aligned} \mathbf{I}_l &= \arg \min_{\mathbf{I}_l} E(\mathbf{I}_l), \\ E(\mathbf{I}_l) &= \phi\left(\|\mathbf{J}_l - \mathbf{P}_l \mathbf{I}_l\|_2^2\right) + \lambda_{I_l} R(\mathbf{I}_l) \end{aligned} \quad (6.2)$$

where the first term in the energy function $E(\mathbf{I}_l)$ measures the difference between the LR observation and predicted data in a ℓ^2 -norm form and $\phi(\cdot)$ is a robust function. The robust function is a class of symmetric, positive-definite functions with a unique minimum at zero, and less increasing than the quadratic function, $f(x) = x^2$. The goal of such a robust function is to decrease the influence of so-called outliers, i.e. large values of the ℓ^2 -norm $\|\mathbf{J}_l - \mathbf{P}_l \mathbf{I}_l\|_2^2$ so that the energy function more likely reaches a global minimum [182].

Unfortunately, the estimation of \mathbf{I}_l still cannot be uniquely determined from Eq. (6.2) since the size of the image \mathbf{I}_l is always no smaller than that of the blurring kernel, which also equals to the rank of the matrix \mathbf{P}_l . SR restoration from single LR image Eq. (6.2) therefore turns into an ill-posed problem [183]. To make Eq. (6.2) well-posed, multiple LR observations, $\{\mathbf{J}_k\}_{k=1,\dots,l,\dots,M}$ of the HR images $\{\mathbf{I}_k\}_{k=1,\dots,l,\dots,M}$ that represent different ‘looks’ of the same scene \mathbf{I}_l , are therefore needed to provide additional information for SR restoration [20, 23, 33, 167, 179, 181]. The relation between the two HR images, \mathbf{I}_l and \mathbf{I}_k , is measured by a matrix \mathbf{C}_{kl} that gives the pixel-level correspondence of the two HR images. The minimization problem Eq. (6.2) can then be written as

$$\begin{aligned} \mathbf{I}_l &= \arg \min_{\mathbf{I}_l} E(\mathbf{I}_l), \\ E(\mathbf{I}_l) &= \sum_{k=1}^M \phi\left(\|\mathbf{J}_k - \mathbf{P}_k \mathbf{C}_{kl} \mathbf{I}_l\|_1^2\right) + \lambda_{I_l} R(\mathbf{I}_l) \end{aligned} \quad (6.3)$$

In practice, the correspondence matrix \mathbf{C}_{kl} is unknown to the observer but is assumed to be unchanged during the degrading process. As such, the matrix can be determined by the correspondence between LR images [181]. The first term of the energy function $E(\mathbf{I}_l)$ in Eq. (6.3) therefore measures the sum of multiple differences that provides more constraints for estimating the \mathbf{I}_l , compared to that by using single constraint in Eq. (6.2).

Provided that \mathbf{I}_l and \mathbf{I}_k are different looks of the same scene, the matrix \mathbf{C}_{kl} is then not unitary and thus the rank of matrix $\mathbf{P}_k \mathbf{C}_{kl}$ is no longer less than that of the HR image \mathbf{I}_l , resulting in a unique solution of \mathbf{I}_l from Eq. (6.3) [20, 165, 173, 179, 181].

In general, the performance of a SR restoration algorithm depends on three factors: the estimation accuracy of the blurring kernel \mathbf{P}_k and the correlations \mathbf{C}_{kl} among multiple LR observations, and the ability of noise removal [167, 173, 176, 179, 181]. In applications such as space imaging [33], surveillance [166] and mobile cameras [167], the former two often vary from observations to observations during the capturing process. An accurate and robust estimation of them is thus a key for the SR restoration. Compared to these two factors, the removal of noise is not essential since images are often acquired under strong illumination energy, which often results in high-SNR images. On the contrary, in other applications such as medical imaging [4, 171, 172, 176] where imaging environments can be perfectly controlled in laboratories, the former two factors can be known during image acquisition or their estimation can be obtained very accurately. The noise contamination in the medical imaging process, however, can be rather high due to low dosages of illumination radiation and short durations of data acquisition to release patients' discomfort. The performance of SR restoration in medical imaging then largely depends on a good removal of noise. For the application of biological florescent microscopy, the imaging environment is quite similar as that in medical imaging where the motion and blurring parameters can be known as priors or estimated accurately in an easy way. As such, when I try to apply SR restoration in biological microscopy imaging, the problem of noise removal is the key factor to determine the performance of resolution recovery. Such problem will be solved in the next section, where I propose a new prior model, $R(\mathbf{I}_l)$, and incorporate it in the energy function to $E(\mathbf{I}_l)$ in Eq. (6.3) for noise removing during the inverse process of resolution restoration.

6.2.2 A New Prior Model

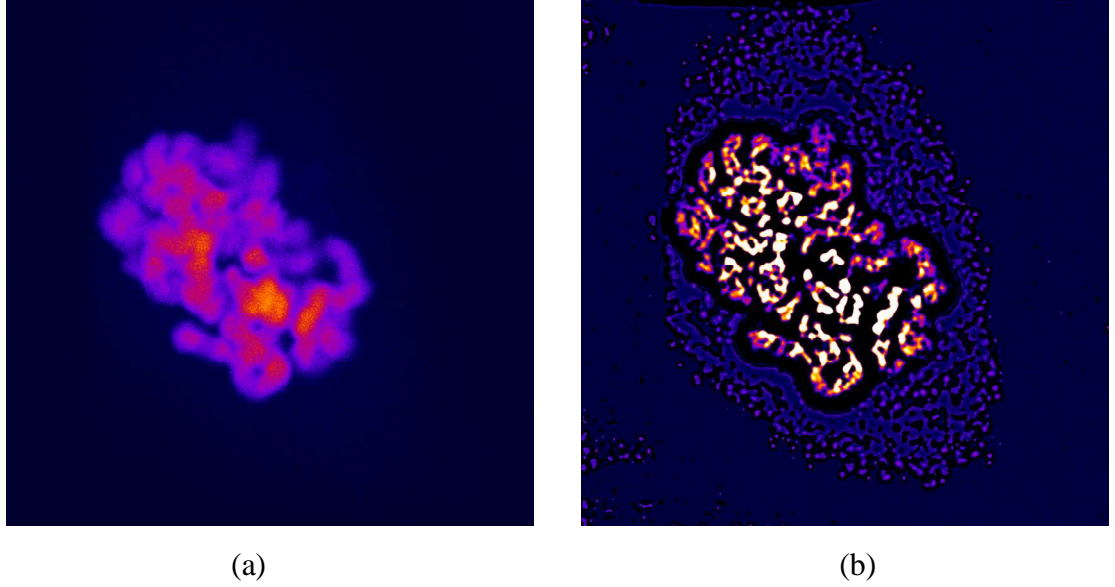


Fig. 6.1 An example of SR restoration without noise removal. (a) An LR DAPI image. (b) The HR image restored by SR restoration without noise removal. The image contains several spurious structures around the nuclei.

In practice, the contamination of noise N_l is inevitable in the imaging process, Eq. (6.1), of fluorescence microscopy even in a high-SNR imaging condition since quantization errors can also introduce noises [23]. If the noise is not suppressed or removed during the inverse process, such random errors will be falsely recognized as structures and thus be amplified by a resolution enhancing behaviour induced by the inverse process Eq. (6.3). Fig. 6.1 shows an example of SR restoration result without noise removal. As seen, the random noises in the LR image (Fig. 6.1(a)) are falsely enhanced as artifacts, namely spurious structures (Fig. 6.1(b)), which may significantly mislead the analysis of biologists both visually and quantitatively. A prior model, $R(I_l)$, should therefore be included in the energy function $E(I_l)$ to regularize the minimization process for noise removal, as given in the second term of $E(I_l)$ in the second equation of Eq. (6.3).

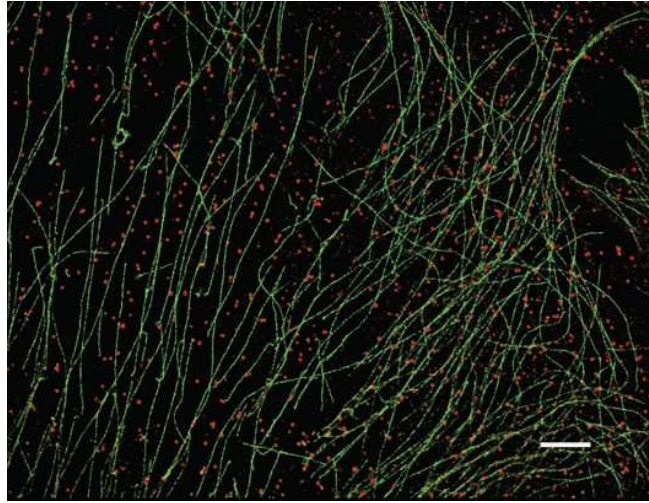


Fig. 6.2 A BS-C-1 cell image contains abundant filaments (green) and clathrin-coated pits and vesicles (red). Scale bar, 3 μm [37].

In general, noise removal is often achieved by smoothing. However, there is a tradeoff between smoothing and feature preservation (and restoration); over-smoothing can introduce blurring effects to features can thus impede image resolution that can be restored [174]. As such, the prior model should be designed to remove noise while preserving key features of interests during the inverse process of SR restoration. The parameter, λ_t , is to balance noise removal and resolution restoration. In general, an edge is a fundamental feature that underlies more complicated features or structures in an image, so the latter can be preserved as long as edges are preserved [177]. Since edges can be characterised by a first-order difference (gradient), many SR restoration methods in medical imaging have applied gradient operators to build the prior model [162, 165-167, 169, 171, 174, 175] and achieved impressive performances in fMRI and PET [170]. However, the gradient-based prior model does not work well when applied to biological fluorescence microscopy. Fluorescence biological microscopy data are usually made up by vesicles, filaments, microtubules and their complex networks, as shown in a cell image Fig. 6.2, which are more complicated than medical images of organs or tissues. Spatial scales of the structures in the two type of images are also very different, the ratio of the full-width-at-half maximum (FWHM) of a microtubule to the PSF of an optical microscope is typically 10 times [37] while the size of a lung lesion to the resolution limitation of PET is usually 2 to 3 times [171]. Since edges embedded in small and complex structures, as demonstrated in our work of image denoising, are prone to noise contamination [177, 178], the gradient-based operators in the fluorescence microscopic images may not be able to robustly detect edges under severe

noise contamination. SR restoration using the gradient-based prior models may therefore fail to preserve these complex structures and restore image resolution during the inverse process.

We here present a new prior model that is capable of characterizing complex fluorescence cell structures to avoid over-smoothing for restoring the resolution of low-SNR images during the inverse process. The model is based on our observations in Chapter 3-4 in bio-imaging denoising that diverse biological structures such as vesicles, filaments, microtubules and their complex networks are made primarily of two basic features, blob and ridge, which are circular and line-like regions either brighter or darker than their surroundings [105, 184], as shown in Fig. 3.2. They are better correlated with a second-order difference rather than a first-order one which measures edges. Inspired by the success of NLDs in image denoising that is a special case of SR restoration in unitary the blurring matrix, I propose a new prior model by combining the 1st- and 2nd-order NLDs in the form,

$$R(\mathbf{I}_l) = \sum_{x=1}^N \phi \left(w_1(x) \left\| \nabla_{\text{NL}} \mathbf{I}_l(x) \right\|_{2,\sigma}^2 + w_2(x) \left\| \nabla_{\text{NL}}^2 \mathbf{I}_l(x) \right\|_{2,\sigma}^2 \right) \quad (6.4)$$

where N is the pixel number of the HR images, $\left\| \nabla_{\text{NL}} \mathbf{I}_l(x) \right\|_{2,\sigma}$ and $\left\| \nabla_{\text{NL}}^2 \mathbf{I}_l(x) \right\|_{2,\sigma}$ are the 1st- and 2nd-order NLDs at the pixel position x given by Eq. (3.2), (3.6) and Eq. (4.8). The coefficients $w_1(x)$ and $w_2(x)$ are weights that balance the contributions of the two NLDs in the forms of

$$w_1(x) = \frac{\left\| \nabla_{\text{NL}} \mathbf{I}_l(x) \right\|_{2,\sigma}^2}{\left\| \nabla_{\text{NL}} \mathbf{I}_l(x) \right\|_{2,\sigma}^2 + \left\| \nabla_{\text{NL}}^2 \mathbf{I}_l(x) \right\|_{2,\sigma}^2}, w_2(x) = \frac{\left\| \nabla_{\text{NL}}^2 \mathbf{I}_l(x) \right\|_{2,\sigma}^2}{\left\| \nabla_{\text{NL}} \mathbf{I}_l(x) \right\|_{2,\sigma}^2 + \left\| \nabla_{\text{NL}}^2 \mathbf{I}_l(x) \right\|_{2,\sigma}^2}. \quad (6.5)$$

Since $\left\| \nabla_{\text{NL}} \mathbf{I}_l(x) \right\|_{2,\sigma} > \left\| \nabla_{\text{NL}}^2 \mathbf{I}_l(x) \right\|_{2,\sigma}$ in the vicinity of edges, $w_1 > w_2$ and the 1st-order NLD dominates the prior model in this region. On the contrary, in the vicinity of blob and ridge features $\left\| \nabla_{\text{NL}} \mathbf{I}_l(x) \right\|_{2,\sigma} < \left\| \nabla_{\text{NL}}^2 \mathbf{I}_l(x) \right\|_{2,\sigma}$, $w_1 < w_2$ and the 2nd-order NLD dominates the prior model. As such, the combination $w_1(x) \left\| \nabla_{\text{NL}} \mathbf{I}_l(x) \right\|_{2,\sigma} + w_2(x) \left\| \nabla_{\text{NL}}^2 \mathbf{I}_l(x) \right\|_{2,\sigma}$ provides well-balanced responses for all edge, blob and ridge features and complex structures made up by them.

6.2.3 Energy Minimization

By combining Eq. (6.3) and Eq. (6.4), I propose to estimate the HR image \mathbf{I}_l by solving the optimization problem,

$$\mathbf{I}_l = \arg \min_{\mathbf{I}_l} \left(\sum_{k=1}^M \phi \left(\left\| \mathbf{J}_k - \mathbf{P}_k \mathbf{C}_{kl} \mathbf{I}_l \right\|_2^2 \right) + \lambda_{I_l} \sum_{x=1}^N \phi \left(w_1(x) \left\| \nabla_{\text{NL}} \mathbf{I}_l(x) \right\|_{2,\sigma}^2 + w_2(x) \left\| \nabla_{\text{NL}}^2 \mathbf{I}_l(x) \right\|_{2,\sigma}^2 \right) \right), \quad (6.6)$$

where the robust function $\phi(\bullet)$ is chosen in the form of

$$\phi(x) = \frac{x}{1+x} \quad (6.7)$$

since it is differentiable so the close-form solution of the estimation \mathbf{I}_l Eq. (6.6) can be easily obtained. Another reason for choosing the form, Eq. (6.7), is the strong ability of Eq. (6.7) to reduce considerably, or even eliminate completely, the influence of large errors for $\left\| \mathbf{J}_k - \mathbf{P}_k \mathbf{C}_{kl} \mathbf{I}_l \right\|_2^2$ due to the inaccurate estimation of \mathbf{P}_k and \mathbf{C}_{kl} , compared to other forms of the robust function [182].

The optimization problem Eq. (6.6) can be solved by finding the solution \mathbf{I}_l so that $\frac{dE(\mathbf{I}_l)}{d\mathbf{I}_l} = 0$, which leads to the following equation

$$\begin{aligned} & \left(\lambda_{I_l} \mathbf{D}_1^T \mathbf{A}_{\text{NL1}} \mathbf{D}_1 + \lambda_{I_l} \mathbf{D}_2^T \mathbf{A}_{\text{NL2}} \mathbf{D}_2 + \sum_{k=1}^M \mathbf{C}_{kl}^T \mathbf{P}_k^T \mathbf{A}_k \mathbf{P}_k \mathbf{C}_{kl} \right) \mathbf{I}_l \\ & = \sum_{k=1}^M \mathbf{C}_{kl}^T \mathbf{P}_k^T \mathbf{A}_k \mathbf{J}_k \end{aligned} \quad (6.8)$$

where the matrices \mathbf{D}_1 and \mathbf{D}_2 correspond to 1st- and 2nd-order NLDs, \mathbf{A}_{NL} and \mathbf{A}_{NL2} are $N \times N$ diagonal matrices whose elements are the derivatives of the robust function $\phi(\cdot)$ in each pixel and N is the pixel number in the image. Details of deriving Eq. (6.8) from Eq. (6.6), as well as definitions of \mathbf{D}_1 , \mathbf{D}_2 , \mathbf{A}_{NL} and \mathbf{A}_{NL2} , can be found in the Appendix section. Eq. (6.8) is a nonlinear equation of \mathbf{I}_l because \mathbf{A}_{NL1} , \mathbf{A}_{NL2} and \mathbf{A}_k also involve the variable \mathbf{I}_l , so may have multiple solutions that correspond to local and global minima of the energy function $E(\mathbf{I}_l)$. We here apply the iterative reweighted least squares (IRLS) method, which has been proven to be effective in non-convex optimization problems [185]. Experimental results have shown that IRLS can at least lead to a local optimum solution that is most close to the global optimum among all local solutions [185]. To solve Eq. (6.8), I assume the initial solution as $\mathbf{I}_l = \mathbf{J}_l$. The solution then evolves iteratively while the energy function is gradually minimized by IRLS. The rate of the evolution is adjusted at each iteration step based on the difference

of HR solutions between the present and previous steps; the rate is usually highly in the beginning and become slower as the energy function gets closer to the global minimum. The parameter λ_{t_i} is also updated at each iteration step according to the residual noise contained in the current HR image estimation [173]. When the difference of the HR image estimations between two adjacent iterations is below a pre-set threshold, the iteration stops and the solution is considered to be the restored HR image. More details about the process of minimizing energy function Eq. (6.6) are given in Appendix..

6.2.4 Translation Microscopy (TRAM)

Based on information theory [21], the LR observations to be used to recover a HR image via the proposed inverse process must be correlated but not identical. For biological microscopy applications, the easiest way to obtain a set of (related) LR images of the same object is to record these images while the microscope or specimen is translated in the XY plane. The correspondence matrix in this case can be easily determined from motion vectors of the two LR images given by the relative positions between the camera and specimen. The PSF matrix in laboratory environment is the same for each LR image and is readily available from the manufacturers of the microscopes or can be accurately estimated using images such as bead or quantum dot samples. We refer to the combination of such a multiple LR image acquisition modality with our SR restoration method as translation microscopy (TRAM) for super-resolution imaging. Compared with other SR imaging techniques such as SIM, STED, STORM, etc., TRAM can be implemented simply on conventional microscopes with no hardware modifications. TRAM can be also operated with other image systems capable of acquiring multiple translational images, including SR facilities to achieve even higher spatial resolutions.

6.3 Experiments

We apply our SR restoration method to a number of synthetic data sets and real fluorescence microscopic data. We first use a simple 1-D test to explain why our prior model works better than the edge-based method by analyzing the inverse process in detail. We further test our method on a 2-D standard resolution chart and a synthetic biological image containing blobs and ridges of varying sizes and orientations. An experiment on human face is also carried out and the results show that our method

works well for natural images. Finally I apply our method to the real fluorescence microscopic images. In all the tests the SR restoration process is measured by the mean squared difference-norm (MSDN) of the restored images between two adjacent iterations given in Eq. (3.21). When the MSDN reaches to a certain small value, the inverse process is terminated.

We have implemented our algorithm by using Matlab R2012b. The computational time of the Matlab code depends on the parameter settings. On a recent Intel i7 3820 3.80 Ghz CPU with 32Gb physical memory, it takes for instance 10h to restore a 256×256 HR image from 32 LR observations with patch size $W = 21$ and 640 iterations. We believe that our algorithm can be largely accelerated by using different optimization strategies such as parallel computing.

6.3.1 Validation on Synthetic Data

We first test our method on 1-D, 2-D synthetic images and compare the results with existing methods, including the robust SR method in [180] (denoted by ZMT), which is based on back projection with median filtering, the robust SR method in [179] (denoted by RSR), which is based on bilateral TV priors, and variational Bayesian SR in [174] (denoted by ALG), which uses Bayesian framework and TV priors. The last method is considered to be the best multi-frame SR restoration algorithm at present [186].

6.3.1.1 Validation on 1-D Signals

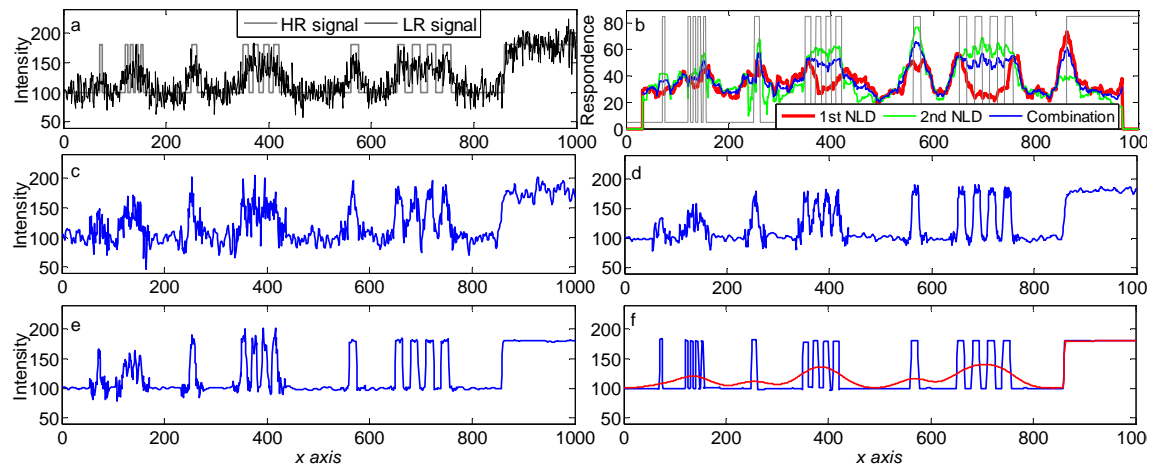


Fig. 6.3. Test on a 1-D signal. (a) A 1-D HR and LR signal containing one step edge, three blobs and strips made of these blobs. (b) Responses of 1st-, 2nd- order NLDs and their combination to the LR signal in (a); (c) – (e) The evolution process leading to HR

restoration by my method; (f) The restored HR signals by our method and by a similar method using an edge-preserving prior model.

Fig. 6.3(a) shows one of the 64 1-D 8-bit HR and LR signals containing one step edge, three single blobs of widths $s = 5, 11$ and 21 pixels and strips made of these blobs in multiple packs, the latter was PSF blurred (Std $\sigma_{\text{PSF}} = 10$ pixel) and noise contaminated (AWGN Std $\sigma_n = 20$) of the former under the general model Eq. (6.1). Fig. 6.3(b) plots the responses of the 1st-, 2nd-order NLDs and their combination to the noisy LR signal; the value of the 1st-order NLD is relatively large in the vicinity of the edge but small in the neighbourhood of the blobs and stripe. On the contrary, the 2nd-order NLD responds better to blobs and stripes than edges. Consequently, a combination of the two, $w_1(x)\|\nabla_{\text{NL}}\mathbf{I}_k(x)\|_{2,\sigma}^2 + w_2(x)\|\nabla_{\text{NL}}^2\mathbf{I}_k(x)\|_{2,\sigma}^2$, gives rise to a well-balanced response to all the features and low response to the background, as shown in Fig. 6.3(b). As such, background regions are smoothed heavily in the initial stage while features are being restored, as shown in Fig. 6.3(c). As the signal evolves during the inverse process, the smoothing effect “propagates” towards the feature regions, which leads to higher contrast between feature and background and therefore increased responses of the 1st- and 2nd-order NLD to the features. The system performs in such a positive feedback manner, leading to more effective noise reduction and resolution improvement in the second stage, as shown in Fig. 6.3(d-e). The iteration process completes when the differences of signals between two adjacent iterations is below a pre-defined threshold. The final result in Fig. 6.3(f) shows good restoration of features and reduction of noise compared to the noise-free image in Fig. 6.3(a). For comparison, I also restore the same set of LR frames by setting our method with $w_1 \equiv 1$ and $w_2 \equiv 0$ in Eq. (6.4), corresponding to the edge-preserving prior model. As seen from the red curve in Fig. 6.3(f), the edge is preserved but the blobs and stripes are smoothed out by using this method.

6.3.1.2 Validation on 2-D Standard Resolution Chart Images

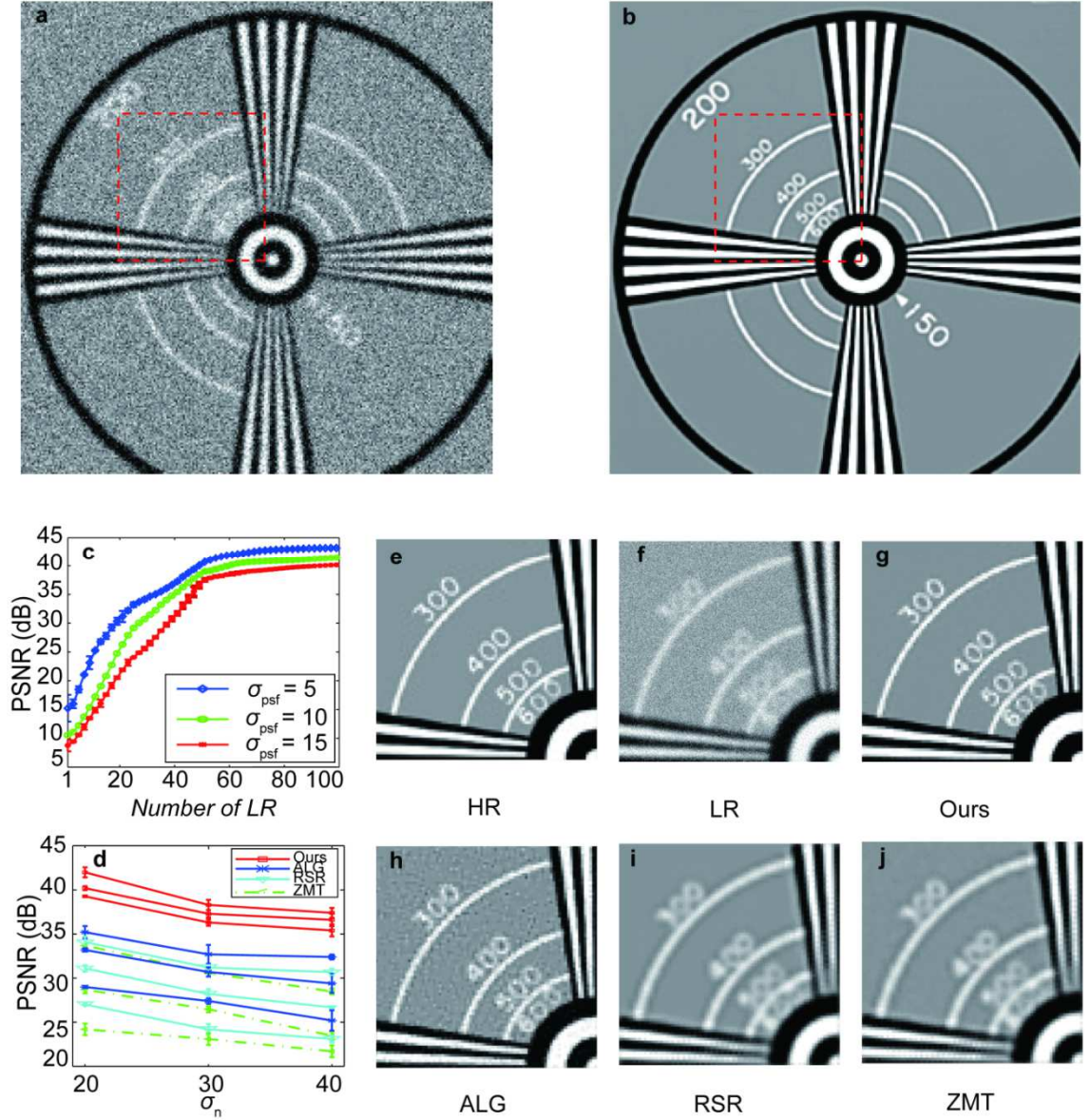


Fig. 6.4. Test results on a 2-D 8-bit resolution chart. (a-b): A resolution chart corrupted by a Gaussian-shaped PSF with Std $\sigma_{PSF} = 5$ (pixels) and an AWGN with Std $\sigma_n = 20$, and the restored result by our method. (c) The mean PSNR of our method versus the frame number of LR images for noise Std $\sigma_n = 20$ and PSF Stds $\sigma_{PSF} = 5, 10, 15$ pixels, respectively. (d): A comparison among the mean PSNR of our method, ALG, RSR and ZMT versus the Noise Std when the PSF Stds $\sigma_{PSF} = 5, 10, 15$, respectively. (e): A close-up region marked by a red box in (a); (f): One frame of LR images generated from (e) by Gaussian-shape PSF with Std $\sigma_{PSF} = 10$ and AWGN with Std $\sigma_n = 20$; (g) – (j): Restoration results by our method, ALG, RSR and ZMT, respectively.

Next I tested on an 8-bit LR resolution chart, as shown in Fig. 6.4(a), which contains blobs and ridges with varying sizes and orientations and is commonly used for a

standard evaluation of SR restoration [187]. The image is corrupted by a Gaussian-shaped PSF with Std $\sigma_{\text{PSF}} = 5$ (pixels) and an AWGN with Std $\sigma_n = 20$. We first apply our method on a set of 64 LR sequences corrupted by a Gaussian-shaped PSF with Std $\sigma_{\text{psf}} = 5$ (pixels) and an AWGN with Std $\sigma_n = 20$. The restored result is shown in Fig. 6.4(b). As seen by comparing Fig. 6.4(a), our result restore very well all features in the resolution chart, including the stripes, curve lines and numbers in the chart image. To quantify the performance, I plot PSNR of our result versus the number of LR frames under same noise situation (Std $\sigma_n = 20$) but three different blurring (Stds $\sigma_{\text{PSF}} = 5, 10, 15$) in Fig. 6.4(c). As seen, all three curves show a monotonic increase of the FWHM ratio on increasing the number of LR observations and begin to saturate at 50 LR images, the latter depends on the noise level in the LR observations. There is however a shift among the three curves because of different severities of PSF blurring; worse image restoration for higher level of PSF blurring for a fixed number of LR images and, for higher blurring levels, more LR observations are required to achieve a same restoration level compared to lower blurring cases.

We also compared our method with three popular existing SR methods, ZMT [180], RSR [179], and ALG [174]. Fig. 6.4(e-j) show respectively the magnified HR, LR and restored images of the boxed region in Fig. 6.4(a) by the four methods using 64 LR frames. As seen, the other three methods either produce severe artifacts (ALG) or fail to restore the image resolution by smooth out numbers and ridges in their results (RSR, ZMT). In contrast, our result shows visually a superior resolution enhancement without artifacts, compared to the original HR one in Fig. 6.4(a). For quantitative comparison, Fig. 6.4(d) plots the PSNRs of the restored results by the four methods on the 64 LR frames for different degradation cases with various noise and PSF levels. As seen, our method for all cases performs noticeably better than the other methods, at least by 5dB in terms of PSNR.

6.3.1.3 Validation on Synthetic Cell Data

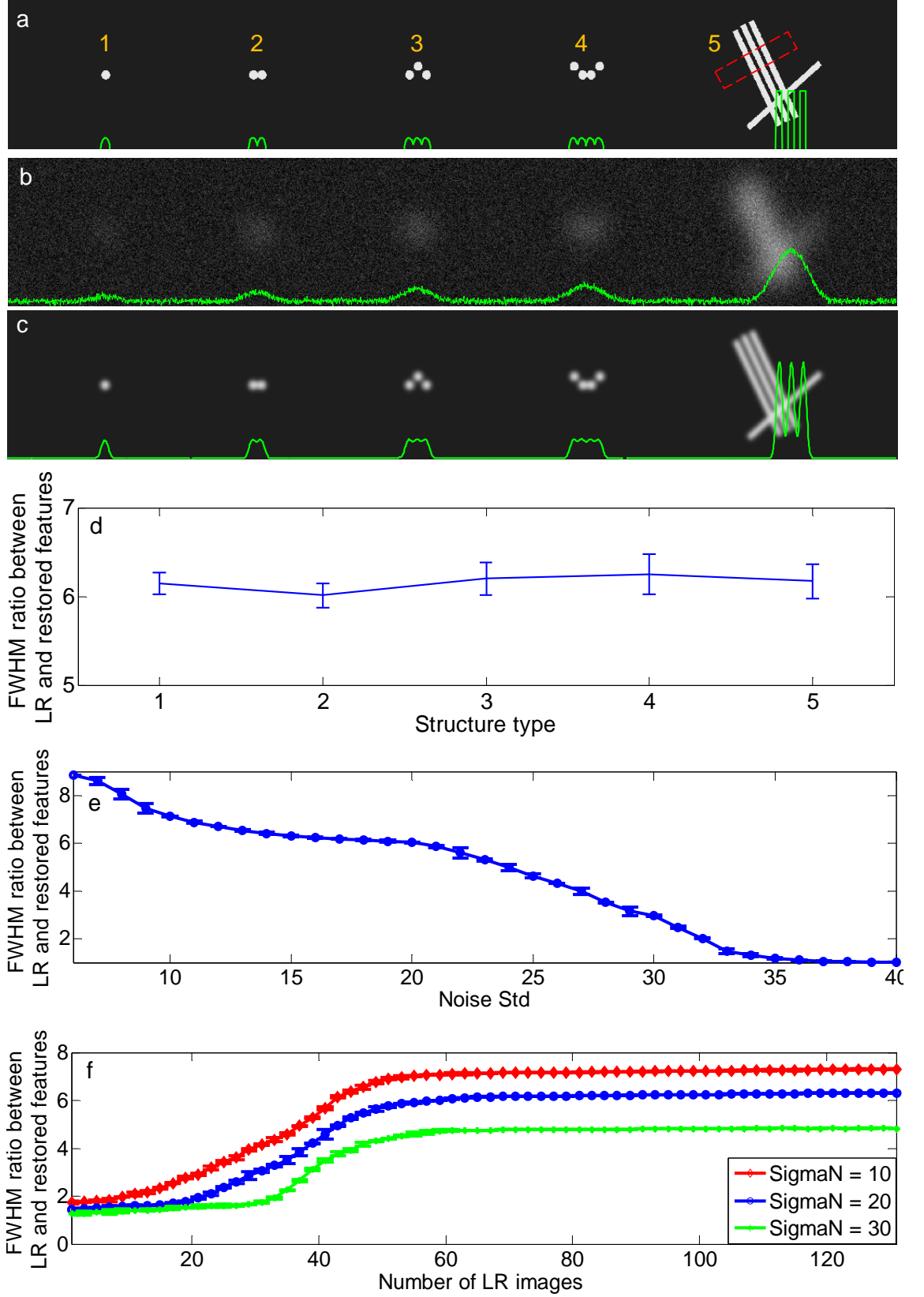


Fig. 6.5 Test results on 2-D synthetic cell data. (a - b) A synthetic HR cell image and its LR observation corrupted with noise contamination of Std $\sigma_n = 20$ and PSF blurring of Std $\sigma_{psf} = 31$ (pixels). 1-D intensity profiles of the five structures LR image are also

plotted as green curves in the two figures. (c) Restored image by our method and the intensity profile in a green curve. (d) FWHM ratio between the LR and restored images for the five types of structures, respectively. (e) FWHM ratio between the LR and restored structures versus the Std of the input noise. The number of LR frames and PSF Std are fixed to be 64 and $\sigma_{\text{PSF}} = 31$ (pixels), respectively. (f) FWHM ratio between the LR and restored structures versus the number of LR images for different input noise levels of Std $\sigma_n = 10, 20$ and 30 , respectively. The Std of PSF is set to be $\sigma_{\text{PSF}} = 31$ (pixels).

Fig. 6.5(a) shows an 8-bit synthetic HR cell image ($2312 \text{ pixel} \times 384 \text{ pixel}$) containing blobs and ridges that mimic the key features of transport particle and microtubules in intracellular structures. The blobs have a diameter of 21 pixels and a centre distance of 21 pixels between the two adjacent ones. The ridges have the FWHM of 10 pixels and a centre-line distance of 32 pixels. The 1-D vertical profiles for the four types of particle arrangements and a cross-sectional profile for the three microtubules are plotted (green curves) in this figure. A set of 64 LR frames are obtained under the TRAM procedure with an AWGN of Std $\sigma_n = 20$ and Gaussian-shaped PSF of Std $\sigma_{\text{PSF}} = 31$ pixels, the latter gives rise to the diffraction limit of 91 pixels [25]. If such diffraction limit equals to the standard one, $\sim 200 \text{ nm}$, for visible lights, the pixel size would be $\sim 2.2 \text{ nm}$. As such, the resolution improvement in this experiment can be measured in a high precision. Fig. 6.5(b) shows a LR observation and corresponding intensity profiles of the HR image in Fig. 6.5(a). As seen, all of structures in this image are diffraction unresolved. Fig. 6.5(c) plots the restored image, showing a remarkable resolution improvement. The resolution improvement is measured to be around 6.3 times for each structure in terms of the FWHM ratio (Fig. 6.5(d)), demonstrating the robustness of our method for different structures. The resolution in the restored image is now ~ 14 pixels (28.4 nm) and is smaller than the distances between the adjacent particles and parallel microtubules. Consequently, all structures are resolved as shown in Fig. 6.5(c).

We further illustrate in Fig. 6.5(e) the resolution improvement of our method on different noise levels for fixed PSF (PSF of Std $\sigma_{\text{psf}} = 31$ pixels) and LR frames (64 frames). As seen, the decrease of the FWHM ratio on increasing noise level can be divided into three stages. In the first stage where the noise contamination is low (noise Std up to 10), the FWHM ratio decreases rapidly, which is consistent with a previous study by Liu and Sun [23] that even low-noise contamination can greatly reduce the

resolution that can be restored. In the final stage where the noise is high (noise Std 20-40), the ratio decreases rapidly again and approaches to 1. This may be attributed to the severity of noise contamination, which makes the capability of resolution restoration decline faster, compared to that in the second stage.

We finally illustrate the dependence of the resolution improvement on the numbers of LR observations for different levels of noise. Fig. 6.5(f) plots the FWHM ratio of our result versus the number of LR frames under same PSF blurring (Std $\sigma_{\text{PSF}} = 21$) but different noise contamination (Stds $\sigma_n = 10, 20, 30$). As seen, the FWHM ratios for all levels of noise contamination show a monotonic increase on increasing the number of LR observations and begin to saturate at 50 LR images. There is however a shift among the three curves because of different severities of noise contamination; less resolution improvement for higher level of noise contamination for a fixed number of LR images and, for higher noise levels, more LR observations are required to achieve a same resolution improvement compared to lower noise cases. As such, the dependence of FWHM ratio on different noise levels behaves similarly to that of PSNR on different blurring levels for the chart image shown in Fig. 6.4(c).

6.3.2 Validation on Face Data



(a)



(b)



(c)



(d)



(e)

Fig. 6.6. Tests on a real face data set. (a) One frame of LR image sequence; (b - e) Reconstruction results by our method, ALG, RSR and ZMT, respectively. It is apparent that our method (b) provides a better recovery, including the eyes, eye bows, nose and hair. Also thanks to the new prior model, our method is also very effective in suppressing noise without introducing artifacts. In comparisons, RSR (d) and ZMT (e) do not effectively restore the HR resolution since the gradient-based prior function over-smoothes the features during the inverse process. ALG (c) recovers the resolution better than RSR and ZMT but results in severe zigzag artifacts around the edges.

Our method can also apply to natural images taken by commercial cameras. The original data cannot be obtained in this case since the observations are not generated

synthetically but taken directly from the imaging devices. For this, I report an experiment performed on a human portrait provided by UCSC [187]. The algorithm ALG, ZMT and RSR are used again for comparisons. Fig. 6.6 (a) shows a LR and restored images by our method, ALG, RSR and ZMT. By comparing Fig. 6.6(b) with Fig. 6.6(c-e), it is apparent that our method provides a better recovery, including the eyes, eye bows, nose and hair. Also thanks to the new prior model, our method is also very effective in suppressing noise without introducing artifacts. In comparisons, RSR and ZMT do not effectively restore the HR resolution since the gradient-based prior function over-smoothes the features during the inverse process. ALG recovers the resolution better than RSR and ZMT but results in severe zigzag artifacts around the edges.

6.3.3 *Validation on Fluorescence Microscopy Data*

We finally test our method on two exemplar datasets of biological interest, the quantum dot (QD) and the cell data samples. The QD data (Invitrogen QDot 625) was diluted 1:1,000,000 in phosphate buffered saline (PBS). Coverslips were coated with CellTak (BD Biosciences) according to the manufacturer's instructions. Diluted quantum dots were incubated on the coated coverslips for one hour prior to imaging in PBS. The cell samples were acquired using the FluoCells pre-prepared slide #2 (Invitrogen) which contains bovine pulmonary artery endothelial cells (BPAEC) stained with Texas Red-X phalloidin, anti-bovine α -tubulin and BODIPY FL labelled secondary antibody, and DAPIthe.

After the samples were prepared, they were acquired by different microscopes. Quantum dot calibration data was acquired on an inverted IX81 microscope (Olympus) using a 150X 1.45 NA objective. Illumination was provided by a fully motorized four laser TIRF combiner coupled to a 405 nm 100W laser under widefield illumination. The sample was laterally translated using a motorized stage (ASI). Image data was collected using an Orce-Flash 4.0s CMOS camera (Hamamatsu) which in combination with a 1.6 \times magnifier in the image path provided an effective pixel size of 27×27 nm. Ten frames were acquired at each position before translation of the stage to the next position. Fixed cell data was acquired on an SP5 SMD laser scanning confocal microscope (Leica) using a 60X 1.4 NA objective. Images 4096×4096 were acquired with a pixel size of $6 \text{ nm} \times 6 \text{ nm}$. A single frame in each channel was acquired before translation of the stage to the next position.

6.3.3.1 Validation on Quantum Dots

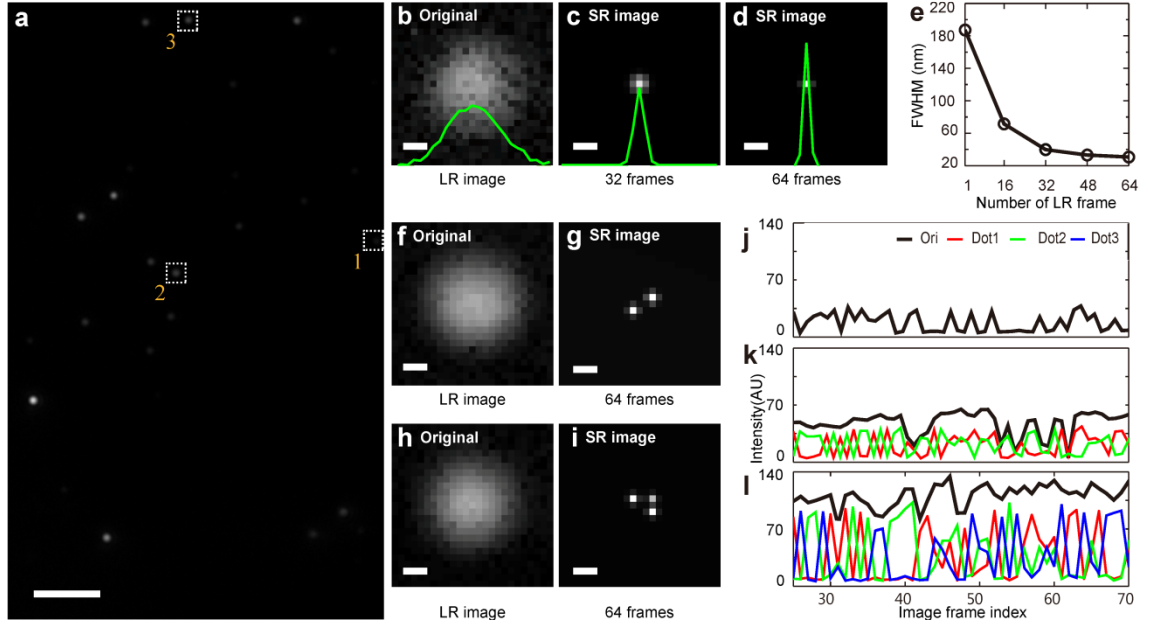


Fig. 6.7. Tests on quantum dot data. (a) A single frame of QDs (diameter: 16 nm) from a series of LR images taken with translation between frames. (b) A close-up LR image of region 1 containing a bright signal corresponding to a single QD, where the green curve is the intensity profile in the horizontal direction. (c-d) Restored SR images using 32 and 64 LR observations respectively, with overlaid intensity profiles. (e) The observed FWHM of the restored quantum dot versus the number of LR observations. (f-g) Close-up LR and SR images of region 2 in (a), where two QDs are resolved. (h-i) Close-up LR and SR images of region 3 in (a), which show 3 QDs. (j) Intensity fluctuations over time in region 1 between bright and dark states (k) Intensity fluctuations of region 2, which are the sum of the intensities of the two resolved QDs in the SR image. (l) Intensity fluctuations of in region 3, which are made of the sum of the intensities of the three resolved QDs in the SR image. Scale bars, 3 μm (a) and 100 nm (b-d,f-i). AU, arbitrary units.

We first test on the quantum dots (QD) images acquired with excitation at 405 nm wavelength on a widefield microscope equipped with a 150X 1.45 NA objective. This gives the diffraction limit 228 nm (thus PSF of 194 nm at FWHM), which in turn determines the convolving matrix, \mathbf{P}_l . A set of LR images was acquired whilst translating the sample along the y-axis in steps of 100 nm, from which the correspondence matrices \mathbf{C}_{kl} in Eq. (6.3) were determined. Fig. 6.7(a) shows a 16-bit LR

image containing several bright spots, with measured noise levels of Std $\sigma_n = 11.2$. As seen, the image contains several bright blobs, each of which can be made up by either single or multiple QDs with vary intensities. Fig. 6.7(b) shows a zoomed image of region 1, where the intensity profile is indeed Airy-disk shape of the FWHM of 194 nm (Gaussian fitting), in agreement with the theoretical value. A green curve is also plotted in this figure as the 1-D intensity profile in the horizontal direction. Fig. 6.7(c) and (d) shows restored SR images resulting from 32 and 64 LR observations, giving measured FWHM of 39.7 and 30.6 nm respectively; an exponential decrease on increasing LR frames is observed as shown in Fig. 6.7(e), showing a resolution improvement of ~ 3 -fold for 16 observations and up to 7-fold for 64 observations. The results are fully consistent with the experiment on synthetic cell data in the last subsection. Our method can also identify multiple diffraction-unresolved QDs in Fig. 6.7(a), as demonstrated indeed for regions 2 and 3 that are magnified and shown in Fig. 6.7(f) and (h), respectively. SR results of the two regions are shown respectively in Fig. 6.7(g) and (i), where 2 and 3 adjacent QDs are separated in the restored images.

To verify the results, a true original SR image should be known. However, since the QDs in the sample are randomly distributed, the numbers and locations of QDs are unknown to observers. In the lack of ground truth for comparison, I investigate QD intensity fluctuations over time for verification, taking advantage of the quantum blinking effect of single QDs [188]. In general, if a bright spot in the LR image contains a single dot, its intensity varies quantally between bright and dark states, as shown in Fig. 6.7(j). However, if a spot contains two QDs, the signal is the sum of those of the two dots, consequently the “off” state appears less frequently, as shown in Fig. 6.7(k). This characteristic becomes more prominent when there are more QD signals in a spot. Fig. 6.7(j-l) plots the intensity variation over time for the three spots in Fig. 6.7(b), (f) and (h), respectively. By a visual comparison among Fig. 6.7(j-l), I find that the intensity variations of the three spots in three boxed regions of Fig. 6.7(a) are consistent with the theory: the black curve in Fig. 6.7(k) is smoother than that of Fig. 6.7(j) and the curve in Fig. 6.7(j) tends to be averaged out by random blinks of all the individual dots in the region. Thus, deconvolving the intensity fluctuations over time alongside our image restoration provides a ‘ground truth’ for TRAM: our restoration can indeed separate single particles from diffraction-unresolved data.

6.3.3.2 Validation on Cell Images

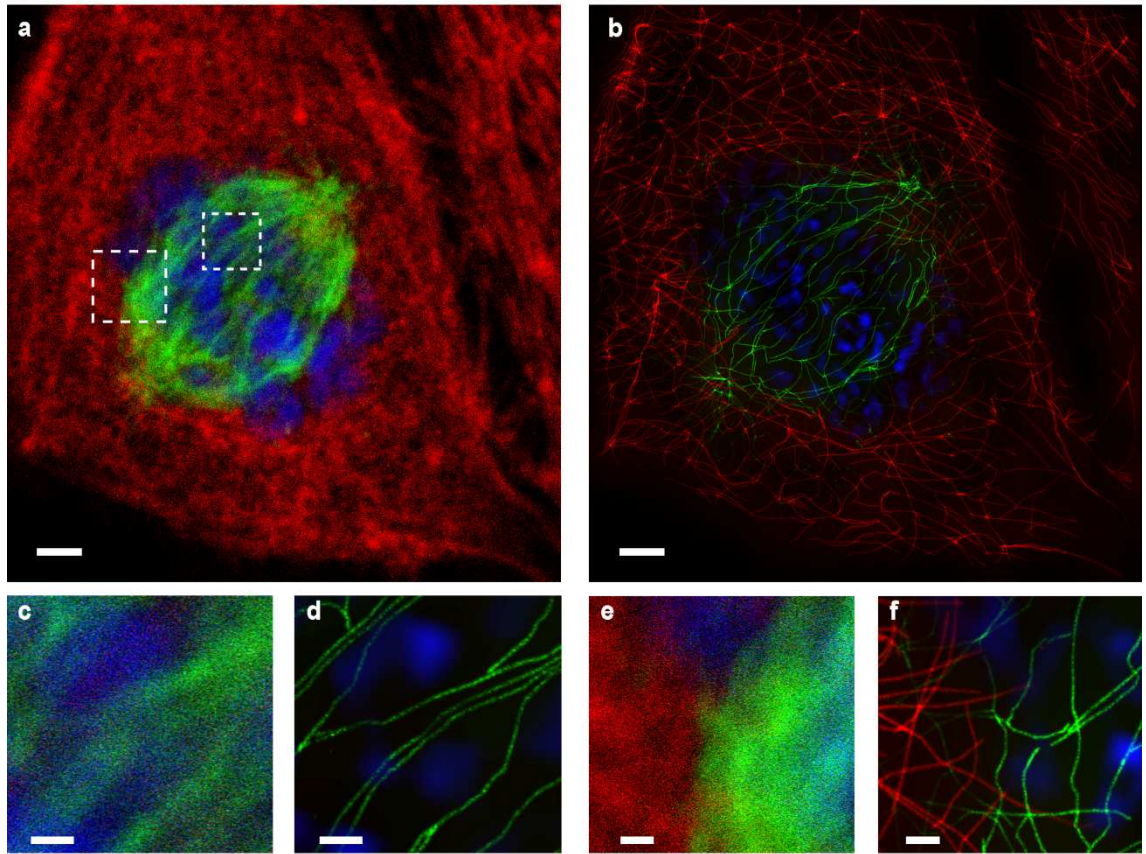


Fig. 6.8. Tests on cell data. (a) One of the 60 LR images acquired whilst translating the sample in steps of 100 nm. Three colours represent three different structures; Red: Actin, Green: Microtubule and Blue: DAPI. (b) Restored SR image by TRAM using the 60 images. (c-d) Zooms of the regions of interest (right dashed box) in (a), showing LR (left) and restored SR views (right), respectively. (e - f) Zooms of the regions of interest (left dashed box) in (a), showing LR (left) and restored SR views (right). Scale bars, 2 μm (a, b) and 400 nm (c - f).

We next analyzed a bovine pulmonary artery endothelial cell sample stained with Texas Red-X phalloidin, anti-bovine α -tubulin and a BODIPY FL labeled secondary antibody, and DAPI. A set of 60 LR observations of all three channels were acquired, with translation of 100 nm between each frame, using a scanning confocal microscope. A LR observation and the restored image are shown respectively in Fig. 6.8(a) and Fig. 6.8(b), the latter demonstrating a dramatic improvement in resolution and signal-to-noise ratio in all three colors. We magnified the two boxed regions of Fig. 6.8(a-b) and showed them in Fig. 6.8(c-d) and Fig. 6.8(e-f), respectively. As seen, in the raw data

where the microtubule network is unresolved and overlaps with DAPI (Fig. 6.8(c)), individual microtubule filaments and DAPI profiles are clearly resolved by TRAM (Fig. 6.8(d)). The measured FWHM of a single microtubule is 31 nm, which represents a resolution improvement of 6.4-fold. When the three stained structures are densely packed and mixed in the LR image (Fig. 6.8(e)), TRAM is capable of refining their relative positions and particularly the boundary between actin and microtubule filaments (Fig. 6.8(f)).

6.4 Conclusion

In summary, in this chapter I first propose to derive a new prior model by combining the 1st- and 2nd-order NLDs and then incorporate it into an energy function in the inverse process to form a new FP-HR restoration method. Based on the FP-HR method, I present a new SR imaging technique that can be used with any motorised microscope with no further hardware modifications. Experimental results on synthetic data demonstrate that our method outperforms several popular HR restoration methods when applied to both synthetic and real natural images. When applied on real fluorescence microscopic data, our method result in a 7-fold increase in the lateral spatial resolution in noisy biological environments, delivering multi-colour image resolution of ~30 nm. We believe that this technique will be of broad interest to the cell-biology community.

Chapter 7

Conclusion

In the previous chapters I have presented several new explorations for image restoration and its applications in fluorescence microscopy. The results of our explorations are summarized as follows.

The first part was devoted to the simplest image restoration, image denoising. After reviewing several popular denoising methods, I pointed out that all these methods were designed by using the 1st-order difference (gradient) of the image intensities to derive the smoothing strengths based on the edge-preservation concept; more complicated features or structures can be preserved as long as edges are preserved, so a good balance between noise removal and feature preserving in the denoised images can be achieved. We further demonstrated that these edge-preserving methods under low-SNR and/or low-contrast conditions may not be able to recover the edges contaminated with severe noise and thus fail to preserve other common features that are made of by the edges, such as blobs, ridges, which are important in the study of many subjects, including live-cell imaging, biometrics, etc. Since blobs and ridges are mathematically most correlated to the 2nd-order difference rather than the 1st-order one which measures edges, I proposed a new 2nd-order NLD and demonstrated its superior performance for blob and ridge detection both in 1-D and 2-D cases, compared to the traditional Laplacian and LoG operators. We further incorporated the 2nd-order NLD into a diffusion model to form a new FP-NAD method. Experiments showed that the FP-NAD outperformed many popular filters for preserving blobs and ridges, reducing noise and minimizing artifacts. However, images captured in the natural environment usually consist of textures and complex networks that are made of a combination of edges and blobs and ridges. Noisy images of this kind can be beyond the capability of FP-NAD. To preserve simultaneously multiple features in natural images, I proposed a new GFP-NAD method, by combining the 1st- and 2nd-order NLD to form a new feature detector in a nonlinear diffusion model. The new feature detector measures image intensity contrasts between neighboring patches in a more sophisticated manner and can therefore effectively capture more features in complex environments. We tested the GFP-NAD on 1-D and 2-D natural images and demonstrated improved performance in removing noise and preserving multiple features and textures, compared to FP-NAD and other popular denoising methods

In the second part of the thesis, I focused on a more sophisticated case of image restoration, super-resolution (SR) restoration in biological fluorescent microscopy to break the barrier of diffraction limit. We first outlined current SR approaches in the fluorescent microscopy. After reviewing several limits of these approaches such as high cost and limited applicability due to complex optical and fluorescent design, I proposed a new and inexpensive SR restoration method for quantitative microscopy in cell biology, where the noise effect is a main challenge. We pointed out that existing SR restoration methods use the edge information during the inverse process and do not perform well in achieving a good balance between noise removal and resolution recovery of features, particularly for fluorescence microscopic images with higher image complexity and smaller features than other images. To overcome this problem, I proposed a new prior model capable of characterizing complex biological structures under severe noise contamination by combining the 1st- and 2nd-order NLDs. The new model was then incorporated in an energy function to form a FR-SR method to seek for an estimation of the original noise-free SR image. To avoid converging to local optimum estimations, I proposed to use an IRLS optimization algorithm, ensuring the convergence towards either a global optimum or a local optimum solution that is most close to the global optimum among all local solutions. By combining the FP-SR restoration with a multiple LR image acquisition modality of translating the microscope cameras, I presented TRAM as a novel, simple and inexpensive SR imaging technique. It can be in principle implemented with any microscopes with no hardware modifications. Numerical experiments illustrated the superior performance of our method over other SR restoration methods, both visually and quantitatively, in simultaneous noise removing and resolution restoring. Experiments on real fluorescence data also result in a ~7-fold increase in lateral spatial resolution in noisy biological environments, delivering multi-colour image resolution of ~30 nm.

Appendix

Energy minimization in Feature-Preserving Super-Resolution Restoration

A.1 Algorithm Procedure

In this appendix, I present a detailed procedure for minimizing the energy function given in Eq. (6.3) for SR restoration. We start by substituting Eq. (6.4) into Eq. (6.3) to rewrite the energy function as,

$$E(\mathbf{I}_l) = \sum_{k=1}^M \phi \left(\left\| \mathbf{J}_k - \mathbf{P}_k \cdot \mathbf{C}_{kl} \mathbf{I}_l \right\|_1^2 \right) + \lambda_{I_l} \sum_{x=1}^N \phi \left(w_1(x) \left\| \nabla_{\text{NL}} \mathbf{I}_l(x) \right\|_{2,\sigma}^2 + w_2(x) \left\| \nabla_{\text{NL}}^2 \mathbf{I}_l(x) \right\|_{2,\sigma}^2 \right), \quad (8.1)$$

where $\left\| \nabla_{\text{NL}} \mathbf{I}_l(x) \right\|_{2,\sigma}^2$ and $\left\| \nabla_{\text{NL}}^2 \mathbf{I}_l(x) \right\|_{2,\sigma}^2$ are respectively the 1st- and 2nd-order non-local difference (NLDs) given by Eq. (3.3), Eq. (3.6) and Eq. (4.8).

The optimization problem, $\mathbf{I}_l = \arg \min_{\mathbf{I}_l} E(\mathbf{I}_l)$, is usually solved by finding the solution \mathbf{I}_l so that the gradient $\frac{dE(\mathbf{I}_l)}{d\mathbf{I}_l} = 0$. However, Eq. (8.1) still contains the scalar

variable $\mathbf{I}_l(x)$, thus the gradient $\frac{dE(\mathbf{I}_l)}{d\mathbf{I}_l}$ cannot be directly calculated. As such, I

rewrite Eq. (6) in a matrix-vector form before differentiation. Since the NLDs involve patches, each of which contains multiple pixels, I define two matrices, $\mathbf{D}_1 \in \mathbb{R}^{N \times N}$ and

$\mathbf{D}_2 \in \mathbb{R}^{N \times N}$ in order to represent the 1st- and 2nd-order NLDs,

$$\mathbf{D}_1 = \begin{bmatrix} \mathbf{0}^{(3W+1) \times N} \\ \mathbf{D}_{NL1} \\ \mathbf{0}^{(3W+1) \times N} \end{bmatrix} \text{ and } \mathbf{D}_2 = \begin{bmatrix} \mathbf{0}^{(3W+1) \times N} \\ \mathbf{D}_{NL2} \\ \mathbf{0}^{(3W+1) \times N} \end{bmatrix}, \quad (8.2)$$

where N is the pixel number in the image, W denotes the half width of the patch, $\mathbf{0}^{(3W+1) \times N}$ is a null matrix to avoid the boundary effect, $\mathbf{D}_{NL1} \in \mathbb{R}^{(N-6W-2) \times N}$ and $\mathbf{D}_{NL2} \in \mathbb{R}^{(N-6W-2) \times N}$ are defined as

$$\mathbf{D}_{NL} = \left[\begin{array}{cccccccccc} \overbrace{-1 \ 0 \ \dots \ 1 \ 0 \ \dots \ 0 \ 0 \ \dots \ 0}^N \\ 0 \ -1 \ 0 \ \dots \ 1 \ 0 \ \dots \ 0 \ \ddots \ 0 \\ \ddots \ \ddots \ \ddots \ \ddots \ \ddots \ \ddots \ \ddots \ \ddots \ \vdots \\ 0 \ \dots \ 0 \ -1 \ 0 \ \dots \ 1 \ 0 \ \dots \ 0 \end{array} \right] \left. \vphantom{\begin{array}{c} \mathbf{D}_{NL} \\ \mathbf{D}_{NL} \\ \mathbf{D}_{NL} \end{array}} \right\}^{N-6W-2} \quad (8.3)$$

and

$$\mathbf{D}_{NL2} = \left[\begin{array}{cccccccccc} \overbrace{-1 \ 0 \ \dots \ 2 \ 0 \ \dots \ -1 \ 0 \ \dots \ 0}^N \\ 0 \ -1 \ 0 \ \dots \ 2 \ 0 \ \dots \ -1 \ \ddots \ 0 \\ \ddots \ \ddots \ \ddots \ \ddots \ \ddots \ \ddots \ \ddots \ \ddots \ \vdots \\ 0 \ \dots \ 0 \ -1 \ 0 \ \dots \ 2 \ 0 \ \dots \ -1 \end{array} \right] \left. \vphantom{\begin{array}{c} \mathbf{D}_{NL2} \\ \mathbf{D}_{NL2} \\ \mathbf{D}_{NL2} \end{array}} \right\}^{N-6W-2}. \quad (8.4)$$

We further define a column vector, $\boldsymbol{\delta}_x \in \mathbb{R}^{N \times 1}$, whose x^{th} element is the only nonzero element with unit value so that the x^{th} element of any vector $\mathbf{v} = [\mathbf{v}(1), \dots, \mathbf{v}(x), \dots, \mathbf{v}(N)]^T$ can be written as

$$\mathbf{v}(x) = \boldsymbol{\delta}_x^T \mathbf{v}. \quad (8.5)$$

Combining Eq.(8.3), (8.4) and (8.5), I rewrite the scalar variable of 1st- and 2nd-order NLD as

$$\|\nabla_{NL} \mathbf{I}_l(x)\|_2^2 = \sum_{i=-W}^W (\boldsymbol{\delta}_{x+i}^T \mathbf{D}_1 \mathbf{I}_l)^2 \quad \text{and} \quad \|\nabla_{NL}^2 \mathbf{I}_l(x)\|_2^2 = \sum_{i=-W}^W (\boldsymbol{\delta}_{x+k}^T \mathbf{D}_2 \mathbf{I}_l)^2. \quad (8.6)$$

The function $E(\mathbf{I}_l)$ is then expressed by using Eq. (8.6) in the following matrix-vector form,

$$\begin{aligned} E(\mathbf{I}_l) = & \sum_{k=1}^M \sum_{x=1}^N \phi \left(\left[\boldsymbol{\delta}_x^T (\mathbf{P}_k \cdot \mathbf{C}_{kl} \mathbf{I}_l - \mathbf{J}_k) \right]^2 \right) \\ & + \lambda_{I_l} \sum_{x=1}^N \phi \left(w_1(x) \sum_{i=-W}^W (\boldsymbol{\delta}_{x+i}^T \mathbf{D}_1 \mathbf{I}_l)^2 + w_2(x) \sum_{i=-W}^W (\boldsymbol{\delta}_{x+k}^T \mathbf{D}_2 \mathbf{I}_l)^2 \right), \end{aligned} \quad (8.7)$$

which no longer contains any scalars related to \mathbf{I}_l . Eq. (8.7) now allows us to directly computer the gradient,

$$\begin{aligned} \frac{dE(\mathbf{I}_l)}{d\mathbf{I}_l} = & \left(\lambda_{I_l} \mathbf{D}_1^T \mathbf{A}_{NL1,l} \mathbf{D}_1 + \lambda_{I_l} \mathbf{D}_2^T \mathbf{A}_{NL2,l} \mathbf{D}_2 + \sum_{k=1}^M \mathbf{C}_{kl}^T \mathbf{P}_k^T \mathbf{A}_k \mathbf{P}_k \mathbf{C}_{kl} \right) \mathbf{I}_l \\ & - \sum_{k=1}^M \mathbf{C}_{kl}^T \mathbf{P}_k^T \mathbf{A}_k \mathbf{J}_k \end{aligned} \quad (8.8)$$

where the $N \times N$ diagonal matrices, \mathbf{A}_{NL1} and \mathbf{A}_{NL2} , are given as

$$\begin{aligned} \mathbf{A}_{\text{NL1},l} &= \left[\sum_{x=1}^N w_1(x) \sum_{i=-W}^W \phi' \left(w_1(x) \|\nabla_{\text{NL}} \mathbf{I}_l(x)\|^2 + w_2(x) \|\nabla_{\text{NL}}^2 \mathbf{I}_l(x)\|^2 \right) \boldsymbol{\delta}_{x+i} \boldsymbol{\delta}_{x+i}^T \right] \\ \mathbf{A}_{\text{NL2},l} &= \left[\sum_{x=1}^N w_2(x) \sum_{i=-W}^W \phi' \left(w_1(x) \|\nabla_{\text{NL}} \mathbf{I}_l(x)\|^2 + w_2(x) \|\nabla_{\text{NL}}^2 \mathbf{I}_l(x)\|^2 \right) \boldsymbol{\delta}_{x+i} \boldsymbol{\delta}_{x+i}^T \right] \end{aligned} \quad (8.9)$$

and the $N \times N$ diagonal matrix \mathbf{A}_k , is given as

$$\begin{aligned} \mathbf{A}_k &= \text{diag}(\boldsymbol{\Phi}_k) \\ \boldsymbol{\Phi}_k &= \left[\phi' \left(\left(\boldsymbol{\delta}_1^T (\mathbf{P}_k \cdot \mathbf{C}_{kl} \mathbf{I}_l - \mathbf{J}_k) \right)^2 \right), \dots, \phi' \left(\left(\boldsymbol{\delta}_N^T (\mathbf{P}_k \cdot \mathbf{C}_{kl} \mathbf{I}_l - \mathbf{J}_k) \right)^2 \right) \right]^T. \end{aligned} \quad (8.10)$$

The minimization, i.e., $\frac{dE(\mathbf{I}_l)}{d\mathbf{I}_l} = 0$, leads to the following equation,

$$\left(\lambda_{I_l} \mathbf{D}_1^T \mathbf{A}_{\text{NL1},l} \mathbf{D}_1 + \lambda_{I_l} \mathbf{D}_2^T \mathbf{A}_{\text{NL2},l} \mathbf{D}_2 + \sum_{k=1}^M \mathbf{C}_{kl}^T \mathbf{P}_k^T \mathbf{A}_k \mathbf{P}_k \mathbf{C}_{kl} \right) \mathbf{I}_l = \sum_{k=1}^M \mathbf{C}_{kl}^T \mathbf{P}_k^T \mathbf{A}_k \mathbf{J}_k, \quad (8.11)$$

which is a nonlinear equation of \mathbf{I}_l because \mathbf{A}_{NL1} , \mathbf{A}_{NL2} and \mathbf{A}_k also involve the variable \mathbf{I}_l , so will have multiple solutions that correspond to local and global minima of the energy function $E(\mathbf{I}_l)$. We here apply a modified iterative reweighted least squares (MIRLS) method [185]. We first rewrite Eq. (8.11) as,

$$\sum_{k=1}^M \left(\frac{1}{2} \mathbf{B}_k - \mathbf{Q}_k \right) = \sum_{k=1}^M \left(\frac{1}{M} \lambda_{I_l} \mathbf{F}_k \mathbf{I}_l - \frac{1}{2} \mathbf{B}_k \right), \quad (8.12)$$

where the matrices \mathbf{B}_k , \mathbf{F}_k , \mathbf{Q}_k are given respectively as

$$\begin{aligned} \mathbf{B}_k &= \mathbf{C}_{kl}^T \mathbf{P}_k^T \mathbf{A}_k \mathbf{J}_k \\ \mathbf{Q}_k &= \mathbf{C}_{kl}^T \mathbf{P}_k^T \mathbf{A}_k \mathbf{P}_k \mathbf{C}_{kl} \mathbf{I}_l \\ \mathbf{F}_k &= \mathbf{D}_1^T \mathbf{A}_{\text{NL1},l} \mathbf{D}_1 + \mathbf{D}_2^T \mathbf{A}_{\text{NL2},l} \mathbf{D}_2 \end{aligned} \quad (8.13)$$

We then modify the nonlinear equation Eq. (8.12) of \mathbf{I}_l as,

$$\left\{ \begin{array}{l} \frac{1}{2} \mathbf{B}_1 - \mathbf{Q}_1 = \lambda_{I_1} \mathbf{F}_1 \mathbf{I}_l / M - \frac{1}{2} \mathbf{B}_1 \\ \vdots \\ \frac{1}{2} \mathbf{B}_k - \mathbf{Q}_k = \lambda_{I_k} \mathbf{F}_k \mathbf{I}_l / M - \frac{1}{2} \mathbf{B}_k \\ \vdots \\ \frac{1}{2} \mathbf{B}_M - \mathbf{Q}_M = \lambda_{I_M} \mathbf{F}_M \mathbf{I}_l / M - \frac{1}{2} \mathbf{B}_M \end{array} \right., \quad (8.14)$$

which contains more constraint than Eq. (8.12) since the unknown image \mathbf{I}_l should satisfy not only one equation but also M equations simultaneously. The solution \mathbf{I}_l by using Eq. (8.14) can therefore satisfy Eq. (8.12). The main steps of MIRLS for solving Eq. (8.14) are:

(a) Initialization: Let $\mathbf{I}_l = \mathbf{J}_l$ and $\lambda_{I_l} = \sigma_n$, where LR observation \mathbf{J}_k , the blurring matrix \mathbf{P}_k , the correspondence matrix \mathbf{C}_{kl} and the noise Std σ_n are known.

(b) Computer the weight matrices \mathbf{B}_k , \mathbf{F}_l , \mathbf{Q}_k by Eq. (8.13) based on the current estimate \mathbf{I}_l

(c) For each frame k :

(c1) Solve the equation $\hat{\mathbf{I}}_{l,k} = \operatorname{argmin} \left\| \frac{1}{2} \mathbf{B}_k - \mathbf{Q}_k \right\|_2^2$. The solution $\hat{\mathbf{I}}_{l,k}$ is an intermediate solution of the final estimation $\mathbf{I}_{l,k}$ in step (c).

(c2) Given $\hat{\mathbf{I}}_{l,k}$, calculate the final estimation $\mathbf{I}_{l,k}$ in step (c) by solving the equation $\mathbf{I}_{l,k} = \operatorname{argmin} \left\| \lambda_{I_k} \mathbf{F}_k \hat{\mathbf{I}}_{l,k} / M - \frac{1}{2} \mathbf{B}_k \right\|_2$

(d) The solution \mathbf{I}_l is obtained by a weighted average of $\{\mathbf{I}_{l,k}\}_{k=1,\dots,M}$

$$\mathbf{I}_l = \left[\sum_{k=1}^M \mathbf{w}_1(k) \mathbf{I}_{l,k}(1), \sum_{k=1}^M \mathbf{w}_2(k) \mathbf{I}_{l,k}(2), \dots, \sum_{k=1}^M \mathbf{w}_N(k) \mathbf{I}_{l,k}(N) \right]^T, \quad (8.15)$$

where the weight vector is given as

$$\mathbf{w}_i = [\phi'(\mathbf{I}_1(i) - \mathbf{I}_l(i)), \dots, \phi'(\mathbf{I}_M(i) - \mathbf{I}_l(i))]^T / C_k, i = 1, 2, \dots, N, \quad (8.16)$$

and C_k is a normalization factor. This step enforces that the multiple solutions $\mathbf{I}_{l,k}$ by step (c) should be similar to each other.

(e) Go to step (c) if Eq. (8.12) cannot be satisfied using the current estimation \mathbf{I}_l ; otherwise update the parameter λ_{I_l} according to the residual noise in \mathbf{I}_l [173].

(f) The iteration stops when \mathbf{I}_l converges (measured by MSDN Eq. (3.21) between two adjacent images) and is considered to be the restored image; otherwise go to step (b) to compute again the weight matrices with updated \mathbf{I}_l .

The intermediate solution $\hat{\mathbf{I}}_{l,k} = \operatorname{argmin} \left\| \frac{1}{2} \mathbf{B}_k - \mathbf{Q}_k \right\|_2^2$ in Step (c1) can be solved by many approaches, e.g. conjugate gradient (CG), Wiener Filter, or shrinkage method. I solve it by iteratively using Wiener Filter method with a slight modification as

$$\hat{\mathbf{I}}_{l,k} = \frac{1}{2} \left(\mathbf{I}_{l,k}^{\text{pre}} + \left(\mathbf{P}_k^T \mathbf{P}_k + \text{eps} \right)^{-1} \left(\mathbf{P}_k^T \mathbf{J}_k - \mathbf{P}_k^T \mathbf{P}_k \mathbf{I}_{l,k}^{\text{pre}} \right) \right), \quad (8.17)$$

where eps is a small constant to make sure the stability of the matrix inverse, $\mathbf{I}_{l,k}^{\text{pre}}$ is the solution for the previous iteration. Given the intermediate solution $\hat{\mathbf{I}}_{l,k}$, we then solve the equation

$$\begin{aligned} \mathbf{I}_{l,k} &= \operatorname{argmin} \left\| \lambda_{I_k} \mathbf{F}_k \hat{\mathbf{I}}_{l,k} / M - \frac{1}{2} \mathbf{B}_k \right\|_2^2 \\ &= \operatorname{argmin} \left\| \frac{1}{2} \lambda_{I_k} \mathbf{F}_k \left(\mathbf{I}_{l,k} + \left(\mathbf{P}_k^T \mathbf{P}_k + \text{eps} \right)^{-1} \left(\mathbf{P}_k^T \mathbf{J}_k - \mathbf{P}_k^T \mathbf{P}_k \mathbf{I}_{l,k} \right) \right) / M - \frac{1}{2} \mathbf{B}_k \right\|_2^2, \quad (8.18) \\ &= \operatorname{argmin} \left\| \lambda_{I_k} \mathbf{F}_k \left(\mathbf{I}_{l,k} + \left(\mathbf{P}_k^T \mathbf{P}_k + \text{eps} \right)^{-1} \left(\mathbf{P}_k^T \mathbf{J}_k - \mathbf{P}_k^T \mathbf{P}_k \mathbf{I}_{l,k} \right) \right) / M - \mathbf{B}_k \right\|_2^2 \end{aligned}$$

which is supposed to be also solved by Wiener filter but the stability heavily depends on the constant eps. A small eps can bring several artifacts while a large eps can give inaccurate estimation of the solution $\mathbf{I}_{l,k}$. We revise the equation by adding a regularization term as

$$\begin{aligned} \mathbf{I}_{l,k} &= \operatorname{argmin} \left\| \lambda_{I_k} \mathbf{F}_k \left(\mathbf{I}_{l,k} + \left(\mathbf{P}_k^T \mathbf{P}_k + \text{eps} \right)^{-1} \left(\mathbf{P}_k^T \mathbf{J}_k - \mathbf{P}_k^T \mathbf{P}_k \mathbf{I}_{l,k} \right) \right) / M - \mathbf{B}_k \right\|_2^2, \quad (8.19) \\ &\quad + \left\| \operatorname{Root}(\mathbf{A}_{\text{NL1},k})^{-1} \mathbf{D}_1 \mathbf{I}_{l,k} \right\|_1 + \left\| \operatorname{Root}(\mathbf{A}_{\text{NL2},k})^{-1} \mathbf{D}_2 \mathbf{I}_{l,k} \right\|_1 \end{aligned}$$

where $\|\bullet\|_1$ is the l-1 norm and operator $\operatorname{Root}(\mathbf{A}_{\text{NL1},l})$ generate a new matrix whose elements are square root of the corresponding elements of the matrix $\mathbf{A}_{\text{NL1},l}$. We can then solve Eq.(8.19) using a well-known method of least-absolute-shrinkage-and-selection-operator (lasso) [189] as,

$$\begin{aligned} \mathbf{I}_{l,k}(x) &= \delta_x \mathbf{D}_1 \operatorname{Root}(\mathbf{A}_{\text{NL1},k})^{-1} \operatorname{sgn} \left(\operatorname{Root}(\mathbf{A}_{\text{NL1},k})^{-1} \mathbf{D}_1 \mathbf{I}_{l,k} \right) \\ &\quad \times \left(\left| \operatorname{Root}(\mathbf{A}_{\text{NL1},k})^{-1} \mathbf{D}_1 \mathbf{I}_{l,k} \right| - \lambda_{I_k} / M \right)^+ \\ &\quad + \delta_x \mathbf{D}_2 \operatorname{Root}(\mathbf{A}_{\text{NL2},k})^{-1} \operatorname{sgn} \left(\operatorname{Root}(\mathbf{A}_{\text{NL2},k})^{-1} \mathbf{D}_2 \mathbf{I}_{l,k} \right) \\ &\quad \times \left(\left| \operatorname{Root}(\mathbf{A}_{\text{NL2},k})^{-1} \mathbf{D}_2 \mathbf{I}_{l,k} \right| - \lambda_{I_k} / M \right)^+ \end{aligned}, \quad (8.20)$$

where $\text{sgn}(\bullet)$ is a sign function and $(\bullet)^+$ is a shrinkage function given as [190],

$$(x-a)^+ = \begin{cases} x-a & |x-a| > 0 \\ 0 & \text{else} \end{cases}. \quad (8.21)$$

A.2 Numerical implementation

The calculation of the matrices \mathbf{A}_{NL1} and \mathbf{A}_{NL2} in Eq. (8.9) uses the 1st- and 2nd- order NLD since the image features in most cases are most correlated to the two NLDs. This is true for biological images. The natural images however may contain features that are not only correlated the two but also correlated to other NLDs, the orders of which depend on the features themselves and can vary at different pixel positions x . Since similar patches should use the same number of NLDs, I firstly cluster all image patches into separate classes using K-means clustering method [191]. The number of NLDs for each class is then estimated adaptively using singular vector decomposition (SVD).

I first define a multivariate function $I(\mathbf{P}_x)$ of the patch $\mathbf{P}_x \in R^{(2W+1) \times 1}$, which as defined in Eq. (3.1), is a vector consisting intensities of all pixels within the neighbourhood region \mathcal{N}_x of the pixel x . The value of the function $I(\mathbf{P}_x)$ is chosen to be the x -th element $\delta_x^T \mathbf{I}$ of the image vector \mathbf{I} , namely $I(\mathbf{P}_x) = \delta_x^T \mathbf{I}$. As a result, we can present the function $I(\mathbf{P}_x)$ as its Taylor series,

$$\delta_x^T \mathbf{I} = \begin{bmatrix} 1 & \|\mathbf{P}_x - \mathbf{P}_{x_i}\|_2 & \|\text{vech}[(\mathbf{P}_x - \mathbf{P}_{x_i})(\mathbf{P}_x - \mathbf{P}_{x_i})^T]\|_2 & \dots \end{bmatrix} \times \begin{bmatrix} I(\mathbf{P}_{x_i}) & \|\nabla_{\text{NL}} \mathbf{I}(x_i)\|_2 & \|\nabla_{\text{NL}}^2 \mathbf{I}(x_i)\|_2 & \dots \end{bmatrix}^T, \quad (8.22)$$

where the operator $\text{vech}(\bullet)$ is defined as the half-vectorization operator of the “lower-triangular” portion of a symmetric matrix, e.g.,

$$\text{vech}\left(\begin{bmatrix} a & b \\ c & d \end{bmatrix}\right) = [a \quad b \quad d]^T. \quad (8.23).$$

Using Eq. (8.22) and (8.23), the patch \mathbf{P}_x Eq. (3.1) can be hence rewritten as

$$\mathbf{P}_x = [\delta_{x-W}^T \mathbf{I}, \dots, \delta_{x+W}^T \mathbf{I}]^T = \boldsymbol{\Phi}_x \boldsymbol{\beta}_x, \quad (8.24)$$

where the $(2W+1) \times (2W+1)$ matrix $\boldsymbol{\Phi}_x$ and the $(2W+1)$ -dimensional vector $\boldsymbol{\beta}_x$ are written respectively as,

$$\Phi_x = \begin{bmatrix} 1 & \|\mathbf{P}_x - \mathbf{P}_{x-W}\|_2 & \left\| \text{vech}[(\mathbf{P}_x - \mathbf{P}_{x-W})(\mathbf{P}_x - \mathbf{P}_{x-W})^T] \right\|_2 & \cdots \\ \vdots & \vdots & \vdots & \vdots \\ 1 & \|\mathbf{P}_x - \mathbf{P}_{x+W}\|_2 & \left\| \text{vech}[(\mathbf{P}_x - \mathbf{P}_{x+W})(\mathbf{P}_x - \mathbf{P}_{x+W})^T] \right\|_2 & \cdots \end{bmatrix} \quad (8.25)$$

and

$$\beta_x = \begin{bmatrix} \mathbf{I}(x) \\ \left\| \nabla_{\text{NL}} \mathbf{I}(x_i) \right\|_2 \\ \left\| \nabla_{\text{NL}}^2 \mathbf{I}(x_i) \right\|_2 \\ \vdots \end{bmatrix}. \quad (8.26)$$

As such, the NLD vector β_x can be obtained as

$$\beta_x = (\Phi_x^T \Phi_x)^{-1} \Phi_x^T \mathbf{P}_x. \quad (8.27)$$

As discussed earlier, the number of NLDs used for each patch \mathbf{P}_x , corresponding to the number L of the non-zero elements in the vector β_x , should be identical within same classes and differ between different classes. A small value may give rise to inaccurate modelling and a large one can result in over-fitting of the contaminated noise. Suppose that the class h contains G patches $\{\mathbf{P}_x^h\}_{x=1, \dots, G}$, we therefore determine the NLD number L^h for the class h as the minimal number of non-zero elements of the vector β_x by

$$\begin{aligned} L^h &= \min(\|\beta_x^h\|_0), \\ \text{subject to } \sum_{x=1}^G \|\mathbf{P}_x^h - \Phi_x^h \beta_x^h\|_2^2 &= \sum_{x=1}^G \left\| \mathbf{P}_x^h - \Phi_x^h (\Phi_x^h)^T \mathbf{P}_x^h \right\|_2^2 \leq \gamma^h, \end{aligned} \quad (8.28)$$

where ℓ^0 -norm $\|\mathbf{v}\|_0$ of a vector \mathbf{v} is also the non-zero elements of \mathbf{v} , the parameter γ^h is determined by the noise level for the patches in the class h . Eq. (8.28) can be solved by using the SVD of the matrix Φ_x^h [192], the main steps of which are as follows: (a). For each matrix Φ_x^h , we extract its eigenvalues $\{s_x^h(i)\}_{i=1, \dots, 2W+1}$, where $s_x^h(1) > s_x^h(2) > \dots > s_x^h(2W+1)$; (b) The number L^h is then determined by

$$\begin{aligned} L^h &= \min(m), m = 1, 2, \dots, 2W+1, \\ \text{subject to } \sum_{i=1}^m \sum_{x=1}^G [s_x^h(i)]^2 &\leq 2G\sigma^2, \end{aligned} \quad (8.29)$$

, where σ is the Std of the noise contained in the image \mathbf{I} . In fact, Eq. (8.29) is equivalent to the hard-thresholding method, or hard shrinkage, on the elements $\beta_x(i)$ of NLD vector β_x^h as [79]:

$$\beta_x^h(i) = \begin{cases} \beta_x^h(i) & \beta_x^h(i) > \gamma_x \\ 0 & \text{else} \end{cases}, \quad (8.30)$$

where the threshold γ_x is chosen as $\gamma_x = \frac{\sqrt{2}\sigma}{2W+1}$. In the real application, however, the complexity of performing SVD for each matrix Φ_x^h is unaffordable since all patches require SVD calculation. To simplify the computation, we estimate L^h by performing the SVD on the covariance matrix $\mathbf{C}^h = \frac{1}{G} \sum_{x=1}^G (\mathbf{P}_x^h)(\mathbf{P}_x^h)^T$ of the patch class h so the eigenvalues are computed only once for the class h [192], which is equivalent to the PCA method for the patch class h .

References

- [1] D. Bawden, "Information and digital literacies: a review of concepts," *Journal of documentation*, vol. 57, pp. 218-259, 2001.
- [2] P. M. Lester, *Visual communication: Images with messages*. Belmont, CA: Wadsworth Publishing Company, 2006.
- [3] C. S. Regazzoni, G. Fabri, and G. Vernazza, *Advanced video-based surveillance systems*. Dordrecht, The Netherlands:: Kluwer, 1998.
- [4] I. Bankman, *Handbook of medical imaging: processing and analysis management*. NY, US: Academic Press, 2000.
- [5] T. Furukawa, *Biological imaging and sensing*. Heidelberg, German: Springer-Verlag, 2004.
- [6] B. K. Gunturk and X. Li, *Image Restoration: Fundamentals and Advances* vol. 7. Boca Raton, Florida, US: CRC Press / Taylor & Francis, 2012.
- [7] H. Faraji and W. J. MacLean, "CCD noise removal in digital images," *IEEE Transactions on Image Processing*, vol. 15, pp. 2676-2685, 2006.
- [8] Y. Tsin, V. Ramesh, and T. Kanade, "Statistical calibration of CCD imaging process," in *Proc. IEEE Conference on Computer Vision and Pattern Recognition, (CVPR)*, 2001, pp. 480-487.
- [9] P. Perona and J. Malik, "Scale-space and edge detection using anisotropic diffusion.," *IEEE Trans. Pattern Anal. Machine Intell.*, vol. 12, pp. 629-639, 1990.
- [10] T. Chan, S. Esedoglu, F. Park, and A. Yip, "Total variation image restoration: Overview and recent developments," in *Handbook of Mathematical Models in Computer Vision*. vol. 17, N. Paragios, Y. Chen, and O. Faugeras, Eds., ed New York, US: Springer-Verlag 2006, pp. 17-31.

- [11] C. Tomasi and R. Manduchi, "Bilateral filtering for gray and color images," *Proc. Sixth International Conference on Computer Vision*, pp. 839–846, 1998.
- [12] F. Catté, P. L. Lions, J. M. Morel, and T. Coll, "Image selective smoothing and edge detection by nonlinear diffusion," *SIAM J. Numer. Anal.*, vol. 29, pp. 182–193, 1992.
- [13] J. Weickert, "Coherence-enhancing diffusion filtering," *International Journal of Computer Vision*, vol. 31, pp. 111–127., 1999.
- [14] S. P. Awate and R. T. Whitaker, "Higher-order image statistics for unsupervised, information-theoretic, adaptive, image filtering," *Proc. IEEE Conference on Computer Vision and Pattern Recognition (CVPR)*, vol. 2, pp. 44–51, 2005.
- [15] A. Buades, B. Coll, and J. M. Morel, "A non-local algorithm for image denoising," *Proc. IEEE Conference on Computer Vision and Pattern Recognition (CVPR)*, vol. 2, pp. 60–65, 2005.
- [16] C. Kervrann and J. Boulanger, "Optimal spatial adaptation for patch-based image denoising," *IEEE Trans. on Image Process*, vol. 15, pp. 2866–2878, 2006.
- [17] H. Takeda, S. Farsiu, and P. Milanfar, "Kernel regression for image processing and reconstruction," *IEEE Transactions on Image Processing*, vol. 16, pp. 349–366, 2007.
- [18] P. Chatterjee and P. Milanfar, "Patch-Based Near-Optimal Image Denoising," *IEEE Transactions on Image Processing*, vol. 21, pp. 1635–1649, 2012.
- [19] L. I. Rudin and S. Osher, "Total variation based image restoration with free local constraints," *Proc. IEEE International Conference on Image Processing*, vol. 1, pp. 31–35, 1994.
- [20] M. Elad and A. Feuer, "Restoration of a single superresolution image from several blurred, noisy, and undersampled measured images," *IEEE Trans. Image Process.*, vol. 6, pp. 1646–1658, 1997.

- [21] N. F. G. Martin and J. W. England, *Mathematical Theory of Entropy*. Cambridge, UK: Cambridge University Press, 2011.
- [22] S. Osher, M. Burger, D. Goldfarb, J. Xu, and W. Yin, "An iterative regularization method for total variation-based image restoration," *Multiscale Modeling & Simulation*, vol. 4, pp. 460-489, 2005.
- [23] C. Liu and D. Sun, "A Bayesian approach to adaptive video super resolution " *Proc. IEEE Conference on Computer Vision and Pattern Recognition (CVPR)*, pp. 209 - 216, 2011.
- [24] E. Abbe, "Beitrage zur Theorie des Mikroskops und der mikroskopischen Wahrnehmung," *Arch. Mikr. Anat.*, vol. 9, pp. 413–420, 1873.
- [25] B. Zhang, J. Zerubia, and J. C. Olivo-Marin, "Gaussian approximations of fluorescence microscope point-spread function models," *Applied Optics*, vol. 46, pp. 1819-1829, 2007.
- [26] S. W. Hell, "Microscopy and its focal switch," *Nat. Methods*, vol. 6, pp. 24-32, 2009.
- [27] R. Heintzmann and M. G. L. Gustafsson, "Subdiffraction resolution in continuous samples," *Nature Photonics*, vol. 3, pp. 362-364, 2009.
- [28] A. L. McEvoy, D. Greenfield, M. Bates, and J. Liphardt, "Q&A: Single-molecule localization microscopy for biological imaging," *BMC biology*, vol. 8, p. 106, 2010.
- [29] M. Chalfie, T. Yuan, G. Euskirchen, W. Ward, and D. Prasher, "Green fluorescent protein as a marker for gene expression," *Science*, vol. 263, pp. 802-805, 1994.
- [30] D. J. Stephens and V. J. Allan, "Light microscopy techniques for live cell imaging," *Science Signalling*, vol. 300, p. 82, 2003.

- [31] K. Jaqaman, D. Loerke, M. Mettlen, H. Kuwata, S. Grinstein, S. Schmid, and G. Danuser, "Robust single-particle tracking in live-cell time-lapse sequences " *Nat. Methods* vol. 5, pp. 695–702, 2008.
- [32] B. O. Leung and K. C. Chou, "Review of super-resolution fluorescence microscopy for biology," *Applied Spectroscopy*, vol. 65, pp. 967-980, 2011.
- [33] T. Akgun, Y. Altunbasak, and R. M. Mersereau, "Super-resolution reconstruction of hyperspectral images," *IEEE Transactions on Image Processing*, vol. 14, pp. 1860-1875, 2005.
- [34] J. Yu, Y. Wang, and Y. Shen, "Noise reduction and edge detection via kernel anisotropic diffusion. ," *Pattern Recognition Letters*, vol. 29, pp. 1496-1503, 2008.
- [35] P. Coupé, P. Hellier, C. Kervrann, and C. Barillot, "Nonlocal means-based speckle filtering for ultrasound images," *IEEE Transactions on Image Processing*, vol. 18, pp. 2221-2229, 2009.
- [36] P. Milanfar, "A tour of modern image filtering," *To appear in IEEE Signal Processing Magazine*, vol. 30, 2013.
- [37] M. Bates, B. Huang, G. T. Dempsey, and X. Zhuang, "Multicolor Super-Resolution Imaging with Photo-Switchable Fluorescent Probes," *Science*, vol. 317, pp. 1749-1753, September 21, 2007 2007.
- [38] J. Shi and J. Malik, "Normalized cuts and image segmentation," *IEEE Transactions on Pattern Analysis and Machine Intelligence*, vol. 22, pp. 888-905, 2000.
- [39] A. L. Yuille, P. W. Hallinan, and D. S. Cohen, "Feature extraction from faces using deformable templates," *International Journal of Computer Vision*, vol. 8, pp. 99-111, 1992.
- [40] W. Zhao, R. Chellappa, P. J. Phillips, and A. Rosenfeld, "Face recognition: A literature survey," *ACM Computing Surveys (CSUR)*, vol. 35, pp. 399-458, 2003.

- [41] P. Meer, "Kernel-based object tracking," *IEEE Transactions on Pattern Analysis and Machine Intelligence*, vol. 25, 2003.
- [42] T. Iijima, "Basic theory on normalization of pattern (In case of typical one-dimensional pattern), in Japanese," *Bulletin of the Electrotechnical Laboratory*, vol. 26, pp. 368-388, 1962.
- [43] A. P. Witkin, "Scale-space filtering," *Int. Joint Conf. Artificial Intelligence*, pp. 1019-1021, 1983.
- [44] T. Iijima, "Theory of pattern recognition," *Electronics and Communications in Japan*, pp. 123-134, 1963.
- [45] T. Iijima, "Basic theory of pattern observation, in Japanese," *Papers of Technical Group on Automata and Automatic Control*, 1959.
- [46] L. Rudin, S. Osher, and E. Fatemi, "Nonlinear total variation based noise removal algorithms," *Physica D*, vol. 60, pp. 259-268, 1992.
- [47] M. J. Black, G. Sapiro, D. H. Marimont, and D. Heeger, "Robust anisotropic diffusion," *IEEE Trans. Image Process*, vol. 7, pp. 421-432, 1998.
- [48] Y. Yu and S. Acton, "Speckle reducing anisotropic diffusion," *IEEE Trans. Image Process.*, vol. 11, pp. 1260-1270, 2002.
- [49] J. Weickert, "Theoretical foundations of anisotropic diffusion in image processing," *Computing, Suppl.*, vol. 11, pp. 221-236, 1996.
- [50] D. Tschumperlé and R. Deriche, "Vector-valued Image Regularization with PDE' s: A Common Framework for Different Applications," *IEEE Trans. Pattern Anal. Machine Intell.*, vol. 27, pp. 506-517, 2005.
- [51] D. Tschumperlé and L. Brun, "Non-local image smoothing by applying anisotropic diffusion PDE's in the space of patches.," *Proc. IEEE Int. Conf. Image Process.*, pp. 2957-2960, 2009.

- [52] D. Tschumperlé, "Fast Anisotropic Smoothing of Multi-Valued Images using Curvature-Preserving PDE's," *International Journal of Computer Vision*, vol. 68, pp. 65--82, 2006.
- [53] A. Buades, B. Coll, and J. M. Morel, "A review of image denoising algorithms, with a new one," *SIAM Multiscale Modeling and Simulation*, vol. 4, pp. 490–530, 2005.
- [54] T. Brox, O. Kleinschmidt, and D. Cremers, "Efficient nonlocal means for denoising of textural patterns," *IEEE Trans. Image Process.*, vol. 17, pp. 1083-1092, 2008.
- [55] T. Tasdizen, "Principal neighborhood dictionaries for nonlocal means image denoising," *IEEE Trans. Image Process.*, vol. 18, pp. 2649-2660, 2009.
- [56] J. Boulanger, C. Kervrann, J. Salamero, J.-B. Sibarita, P. Elbau, and P. Bouthemy, "Patch-based non-local functional for denoising fluorescence microscopy image sequences," *IEEE Trans. Med. Imag.*, vol. 29, pp. 442-454, 2010.
- [57] M. Elad and M. Aharon, "Image denoising via sparse and redundant representations over learned dictionaries," *IEEE Trans. on Image Process.*, vol. 15, pp. 3736-3745, 2006.
- [58] K. Dabov, A. Foi, V. Katkovnik, and K. Egiazarian, "Image denoising by sparse 3-D transform-Domain collaborative filtering.," *IEEE Trans. on Image Process.*, vol. 16, pp. 2080-2095, 2007.
- [59] J. L. Starck, E. J. Candès, and D. L. Donoho, "The curvelet transform for image denoising," *IEEE Transactions on Image Processing*, vol. 11, pp. 670-684, 2002.
- [60] M. N. Do and M. Vetterli, "The finite ridgelet transform for image representation," *IEEE Transactions on Image Processing*, vol. 12, pp. 16-28, 2003.

- [61] R. Eslami and H. Radha, "Translation-invariant contourlet transform and its application to image denoising," *IEEE Transactions on Image Processing*, vol. 15, pp. 3362-3374, 2006.
- [62] D. L. Donoho and J. M. Johnstone, "Ideal spatial adaptation by wavelet shrinkage," *Biometrika*, vol. 81, pp. 425-455, 1994.
- [63] F. Luisier, T. Blu, and M. Unser, "A new SURE approach to image denoising: Interscale orthonormal wavelet thresholding," *IEEE Transactions on Image Processing*, vol. 16, pp. 593-606, 2007.
- [64] M. Elad, B. Matalon, and M. Zibulevsky, "Image denoising with shrinkage and redundant representations," *Proc. IEEE Conference on Computer Vision and Pattern Recognition, (CVPR)*, vol. 2, pp. 1924-1931, 2006.
- [65] S. G. Chang, B. Yu, and M. Vetterli, "Spatially adaptive wavelet thresholding with context modeling for image denoising," *IEEE Transactions on Image Processing*, vol. 9, pp. 1522-1531, 2000.
- [66] E. P. Simoncelli and E. H. Adelson, "Noise removal via Bayesian wavelet coring," *Proc. IEEE International Conference on Image Processing*, vol. 1, pp. 379-382, 1996.
- [67] J. Portilla, V. Strela, M. J. Wainwright, and E. P. Simoncelli, "Image denoising using scale mixtures of Gaussians in the wavelet domain," *IEEE Transactions on Image Processing*, vol. 12, pp. 1338-1351, 2003.
- [68] M. J. Wainwright and E. P. Simoncelli, "Scale mixtures of Gaussians and the statistics of natural images," in *Advances in neural information processing systems*. vol. 12, S. A. Solla, T. K. Leen, and K.-R. Muller, Eds., ed Denver, CO, US: MIT Press, 2000, pp. 855-861.
- [69] D. F. Andrews and C. L. Mallows, "Scale mixtures of normal distributions," *Journal of the Royal Statistical Society. Series B (Methodological)*, vol. 36, pp. 99-102, 1974.

- [70] S. Lyu and E. P. Simoncelli, "Modeling multiscale subbands of photographic images with fields of gaussian scale mixtures," *IEEE Transactions on Pattern Analysis and Machine Intelligence*, vol. 31, pp. 693-706, 2009.
- [71] Y. Kim, *Variational Methods: Theory and Its Applications to Image Deblurring and Denoising Problems*. Charleston, South Carolina, US: BiblioBazaar, 2011.
- [72] N. Paragios, Y. Chen, and O. Faugeras, *Handbook of Mathematical Models in Computer Vision*. New York, US: Springer-Verlag, 2005.
- [73] G. Aubert and P. Kornprobst, *Mathematical Problems in Image Processing: Partial Differential Equations and the Calculus of Variations (Applied Mathematical Sciences)*: Springer-Verlag New York, Inc., 2006.
- [74] B. S. Mordukhovich, *Variational Analysis and Generalized Differentiation I: Basic Theory*, 1st ed. New York, US: Springer, 2005.
- [75] J. J. Koenderink, "The structure of images," *Biological cybernetics*, vol. 50, pp. 363-370, 1984.
- [76] A. Chambolle and P. L. Lions, "Image recovery via total variation minimization and related problems," *Numerische Mathematik*, vol. 76, pp. 167-188, 1997.
- [77] P. Blomgren and T. F. Chan, "Color TV: total variation methods for restoration of vector-valued images," *IEEE Transactions on Image Processing*, vol. 7, pp. 304-309, 1998.
- [78] E. Tadmor, S. Nezzar, and L. Vese, "A multiscale image representation using hierarchical (BV, L^2) decompositions," *Multiscale Modeling & Simulation*, vol. 2, pp. 554-579, 2004.
- [79] S. Mallat, *A wavelet tour of signal processing*. San Diego, CA, US: Academic Press, 1999.
- [80] J. Weickert, *Anisotropic diffusion in image processing* vol. 1. Stuttgart, Germany: Teubner Stuttgart, 1998.

- [81] J. Weickert, B. M. T. H. Romeny, and M. A. Viergever, "Efficient and reliable schemes for nonlinear diffusion filtering," *IEEE Transactions on Image Processing*, vol. 7, pp. 398-410, 1998.
- [82] A. Buades, B. Coll, and J. M. Morel, "The staircasing effect in neighborhood filters and its solution," *IEEE Transactions on Image Processing*, vol. 15, pp. 1499-1505, 2006.
- [83] M. Mahmoudi and G. Sapiro, "Fast image and video denoising via nonlocal means of similar neighborhoods," *IEEE Signal Processing Letters*, vol. 12, pp. 839-842, 2005.
- [84] P. Coupé, P. Yger, S. Prima, P. Hellier, C. Kervrann, and C. Barillot, "An optimized blockwise nonlocal means denoising filter for 3-D magnetic resonance images," *IEEE Transactions on Medical Imaging*, vol. 27, pp. 425-441, 2008.
- [85] A. Dauwe, B. Goossens, H. Luong, and W. Philips, "A fast non-local image denoising algorithm," *Proc SPIE Electronic Imaging*, vol. 6812, p. 8, 2008.
- [86] J. Wang, Y. Guo, Y. Ying, Y. Liu, and Q. Peng, "Fast non-local algorithm for image denoising," *IEEE International Conference on Image Processing*, pp. 1429-1432, 2006.
- [87] B. Goossens, Q. Luong, A. Pizurica, and W. Philips, "An improved non-local denoising algorithm," *Proc. Int. Workshop on Local and Non-Local Approximation in Image Processing (LNLA)*, pp. 143-156, 2008.
- [88] A. Buades, B. Coll, and J. M. Morel, "Nonlocal image and movie denoising," *International journal of computer vision*, vol. 76, pp. 123-139, 2008.
- [89] C. Kervrann and J. Boulanger, "Local adaptivity to variable smoothness for exemplar-based image regularization and representation," *International Journal of Computer Vision*, vol. 79, pp. 45-69, 2008.

- [90] D. Van De Ville and M. Kocher, "Nonlocal means with dimensionality reduction and SURE-based parameter selection," *IEEE Transactions on Image Processing*, vol. 20, pp. 2683-2690, 2011.
- [91] C. M. Stein, "Estimation of the mean of a multivariate normal distribution," *The annals of Statistics*, pp. 1135-1151, 1981.
- [92] S. Kindermann, S. Osher, and P. Jones, "Deblurring and denoising of images by nonlocal functionals," *SIAM Multiscale Modeling and Simulation*, vol. 4, pp. 1091-1115, 2005.
- [93] G. Gilboa and S. Osher, "Nonlocal linear image regularization and supervised segmentation," *SIAM Multiscale Modeling and Simulation*, vol. 6, pp. 595– 630, 2007.
- [94] G. Gilboa, J. Darbon, S. Osher, and T. Chan, "Nonlocal convex functionals for image regularization," *UCLA CAM-report*, pp. 06-57, 2006.
- [95] N. Azzabou, N. Paragios, F. Guichard, and F. Cao, "Variable bandwidth image denoising using image-based noise models," *Proc. IEEE Conference on Computer Vision and Pattern Recognition, (CVPR)*, pp. 1-7, 2007.
- [96] P. Chatterjee and P. Milanfar, "Is Denoising Dead?," *IEEE Trans. on Image Process.*, vol. 19, pp. 895-911, 2010.
- [97] V. Katkovnik, A. Foi, K. Egiazarian, and J. Astola, "From Local Kernel to Nonlocal Multiple-Model Image Denoising.," *International Journal of Computer Vision*, vol. 86, pp. 1-32, 2010.
- [98] M. Elad, "Why simple shrinkage is still relevant for redundant representations?," *IEEE Transactions on Information Theory*, vol. 52, pp. 5559-5569, 2006.
- [99] Y. Hou, C. Zhao, D. Yang, and Y. Cheng, "Comments on "Image denoising by sparse 3-D transform-domain collaborative filtering"," *IEEE Transactions on Image Processing*, vol. 20, pp. 268-270, 2011.

- [100] D. Tschumperlé and L. Brun, "Non-Local Regularization and Registration of Multi-Valued Images By PDE's and Variational Methods on Higher Dimensional Spaces," in *Mathematical Image Processing*. vol. 5, M. Bergounioux, Ed., ed: Springer Berlin Heidelberg, 2011, pp. 181-197.
- [101] Kodak, "<http://www.r0k.us/graphics/kodak/kodim23.html>."
- [102] S. S. Blackman, "Multiple-target tracking with radar applications," *Artech House, Dedham, MA.*, 1986.
- [103] FVC, "Fingerprint Verification Competition, 2004<
<http://bias.csr.unibo.it/fvc2004/>>.".
- [104] D. Eberly, *Ridges in Image and Data Analysis*, 1st ed. vol. 7. Dordrecht, The Netherlands: Kluwer Academic, 1996.
- [105] A. J. Danker and A. Rosenfeld, "Blob Detection by Relaxation," *IEEE Trans. Pattern Anal. Machine Intell.*, vol. 3, pp. 79-92, 1981.
- [106] A. A. Efros and T. K. Leung, "Texture synthesis by non-parametric sampling," *Proc. IEEE Int. Conf. Computer Vision*, pp. 1033-1038, 1999.
- [107] S. P. Awate, T. Tasdizen, and R. T. Whitaker, "Unsupervised texture segmentation with nonparametric neighborhood statistics," *Proc. Euro. Conf. Computer Vision*, pp. 494–507, 2006.
- [108] Z. Wang, A. C. Bovik, H. R. Sheikh, and E. P. Simoncelli, "Image quality assessment: From error visibility to structural similarity," *IEEE Trans. Image Process.*, vol. 13, pp. 600–612, 2004.
- [109] R. Gonzalez and R. E. Woods, *Digital image processing*, 2nd ed. Upper Saddle River, NJ, USA: Prentice Hall, 2002.
- [110] M. Jacob and M. Unser, "Design of Steerable Filters for Feature Detection Using Canny-Like Criteria," *IEEE Trans. Pattern Anal. Machine Intell.*, vol. 26, pp. 1007-1019, 2004.

- [111] W. T. Freeman and E. H. Adelson, "The design and use of steerable filters," *IEEE Trans. Pattern Anal. Machine Intell.*, vol. 13, pp. 891 - 906, 1991.
- [112] B. K. P. Horn, *Robot Vision*. Cambridge, MA: MIT Press, 1986.
- [113] P. Viola and M. Jones, "Robust real-time face detection," *Int. J. Computer Vis.*, vol. 57, pp. 137–154, 2004.
- [114] C. A. Z. Barcelos, M. Boaventura, and E. C. Silva, "A well-balanced flow equation for noise removal and edge detection," *IEEE Trans. Image Process.*, vol. 12, pp. 751–763, 2003.
- [115] C. F. Barnes, H. Fritz, and J. Yoo, "Hurricane disaster assessments with image-driven data mining in high-resolution satellite imagery," *IEEE Transactions on Geoscience and Remote Sensing*, vol. 45, pp. 1631-1640, 2007.
- [116] W. Hu, T. Tan, L. Wang, and S. Maybank, "A survey on visual surveillance of object motion and behaviors," *IEEE Transactions on Systems, Man, and Cybernetics, Part C: Applications and Reviews*, vol. 34, pp. 334-352, 2004.
- [117] A. Hyvärinen, J. Hurri, and P. O. Hoyer, *Natural Image Statistics: A Probabilistic Approach to Early Computational Vision*. New York, US: Springer Publishing Company, Incorporated, 2009.
- [118] H. C. Burger, C. J. Schuler, and S. Harmeling, "Image denoising: Can plain neural networks compete with BM3D?," *Proc. IEEE Conference on Computer Vision and Pattern Recognition (CVPR)*, pp. 2392-2399, June 16-21 2012.
- [119] Z. Ming and B. K. Gunturk, "Multiresolution Bilateral Filtering for Image Denoising," *IEEE Transactions on Image Processing*, vol. 17, pp. 2324-2333, 2008.
- [120] D. G. Lowe, "Distinctive Image Features from Scale-Invariant Keypoints," *International Journal of Computer Vision*, vol. 60, pp. 91-110, 2004.

- [121] E. Rosten, R. Porter, and T. Drummond, "Faster and Better: A Machine Learning Approach to Corner Detection," *IEEE Transactions on Pattern Analysis and Machine Intelligence*, vol. 32, pp. 105-119, 2010.
- [122] O. Tuzel, F. Porikli, and P. Meer, "Pedestrian Detection via Classification on Riemannian Manifolds," *IEEE Transactions on Pattern Analysis and Machine Intelligence*, vol. 30, pp. 1713-1727, 2008.
- [123] R. Unnikrishnan, C. Pantofaru, and M. Hebert, "Toward Objective Evaluation of Image Segmentation Algorithms," *IEEE Transactions on Pattern Analysis and Machine Intelligence*, vol. 29, pp. 929-944, 2007.
- [124] J. W. Lichtman and J. A. Conchello, "Fluorescence microscopy," *Nature Methods*, vol. 2, pp. 910-919, 2005.
- [125] R. Won, "Eyes on super-resolution," *Nat. Photonics*, vol. 3, pp. 368-369, 2009.
- [126] W. R. Zipfel, R. M. Williams, and W. W. Webb, "Nonlinear magic: multiphoton microscopy in the biosciences," *Nature biotechnology*, vol. 21, pp. 1369-1377, 2003.
- [127] S. Hell and E. H. K. Stelzer, "Fundamental improvement of resolution with a 4Pi-confocal fluorescence microscope using two-photon excitation," *Optics communications*, vol. 93, pp. 277-282, 1992.
- [128] S. W. Hell, "Toward fluorescence nanoscopy," *Nature biotechnology*, vol. 21, pp. 1347-1355, 2003.
- [129] M. G. L. Gustafsson, D. A. Agard, and J. W. Sedat, "Sevenfold improvement of axial resolution in 3D widefield microscopy using two objective lenses," *Proc. SPIE*, vol. 2412, pp. 1-6, 1995.
- [130] E. Synge, "A suggested method for extending microscopic resolution into the ultra-microscopic region," *The London, Edinburgh, and Dublin Philosophical Magazine and Journal of Science*, vol. 6, pp. 356-362, 1928.

- [131] L. Novotny and B. Hecht, *Principles of nano-optics*. Cambridge, UK: Cambridge university press, 2006.
- [132] A. Lewis, M. Isaacson, A. Harootunian, and A. Muray, "Development of a 500 Å spatial resolution light microscope: I. light is efficiently transmitted through $\lambda/16$ diameter apertures," *Ultramicroscopy*, vol. 13, pp. 227-231, 1984.
- [133] E. Betzig, A. Lewis, A. Harootunian, M. Isaacson, and E. Kratschmer, "Near field scanning optical microscopy (NSOM): development and biophysical applications," *Biophysical Journal*, vol. 49, pp. 269-279, 1986.
- [134] T. A. Klar and S. W. Hell, "Subdiffraction resolution in far-field fluorescence microscopy," *Optics letters*, vol. 24, pp. 954-956, 1999.
- [135] S. W. Hell and J. Wichmann, "Breaking the diffraction resolution limit by stimulated emission: stimulated-emission-depletion fluorescence microscopy," *Optics letters*, vol. 19, pp. 780-782, 1994.
- [136] M. Hofmann, C. Eggeling, S. Jakobs, and S. W. Hell, "Breaking the diffraction barrier in fluorescence microscopy at low light intensities by using reversibly photoswitchable proteins," *Proceedings of the National Academy of Sciences of the United States of America*, vol. 102, pp. 17565-17569, 2005.
- [137] M. G. L. Gustafsson, "Nonlinear structured-illumination microscopy: wide-field fluorescence imaging with theoretically unlimited resolution," *Proceedings of the National Academy of Sciences of the United States of America*, vol. 102, pp. 13081-13086, 2005.
- [138] M. J. Rust, M. Bates, and X. Zhuang, "Sub-diffraction-limit imaging by stochastic optical reconstruction microscopy (STORM)," *Nature methods*, vol. 3, pp. 793-796, 2006.
- [139] E. Betzig, G. H. Patterson, R. Sougrat, O. W. Lindwasser, S. Olenych, J. S. Bonifacino, M. W. Davidson, J. Lippincott-Schwartz, and H. F. Hess, "Imaging intracellular fluorescent proteins at nanometer resolution," *Science*, vol. 313, pp. 1642-1645, 2006.

- [140] S. T. Hess, T. P. K. Girirajan, and M. D. Mason, "Ultra-high resolution imaging by fluorescence photoactivation localization microscopy," *Biophysical journal*, vol. 91, p. 4258, 2006.
- [141] R. Schmidt, C. A. Wurm, S. Jakobs, J. Engelhardt, A. Egner, and S. W. Hell, "Spherical nanosized focal spot unravels the interior of cells," *Nature methods*, vol. 5, pp. 539-544, 2008.
- [142] R. Schmidt, C. A. Wurm, A. Punge, A. Egner, S. Jakobs, and S. W. Hell, "Mitochondrial cristae revealed with focused light," *Nano letters*, vol. 9, pp. 2508-2510, 2009.
- [143] L. Schermelleh, P. M. Carlton, S. Haase, L. Shao, L. Winoto, P. Kner, B. Burke, M. C. Cardoso, D. A. Agard, and M. G. L. Gustafsson, "Subdiffraction multicolor imaging of the nuclear periphery with 3D structured illumination microscopy," *Science*, vol. 320, pp. 1332-1336, 2008.
- [144] S. W. Hell, "Far-Field Optical Nanoscopy," *Science*, vol. 316, pp. 1153-1158, May 25, 2007 2007.
- [145] E. Rittweger, K. Y. Han, S. E. Irvine, C. Eggeling, and S. W. Hell, "STED microscopy reveals crystal colour centres with nanometric resolution," *Nature Photonics*, vol. 3, pp. 144-147, 2009.
- [146] S. Hell. *Fluorescent Dyes Used in STED Microscopy*. Available: <http://nanobiophotonics.mpibpc.mpg.de/old/dyes/>
- [147] B. Harke, C. K. Ullal, J. Keller, and S. W. Hell, "Three-dimensional nanoscopy of colloidal crystals," *Nano letters*, vol. 8, pp. 1309-1313, 2008.
- [148] M. G. L. Gustafsson, "Surpassing the lateral resolution limit by a factor of two using structured illumination microscopy," *Journal of Microscopy*, vol. 198, pp. 82-87, 2001.

- [149] R. Heintzmann, T. M. Jovin, and C. Cremer, "Saturated patterned excitation microscopy—a concept for optical resolution improvement," *JOSA A*, vol. 19, pp. 1599-1609, 2002.
- [150] W. Moerner, "New directions in single-molecule imaging and analysis," *Proceedings of the National Academy of Sciences*, vol. 104, pp. 12596-12602, 2007.
- [151] A. Yildiz, J. N. Forkey, S. A. McKinney, T. Ha, Y. E. Goldman, and P. R. Selvin, "Myosin V walks hand-over-hand: single fluorophore imaging with 1.5-nm localization," *science*, vol. 300, pp. 2061-2065, 2003.
- [152] R. E. Thompson, D. R. Larson, and W. W. Webb, "Precise nanometer localization analysis for individual fluorescent probes," *Biophysical journal*, vol. 82, pp. 2775-2783, 2002.
- [153] A. Pertsinidis, Y. Zhang, and S. Chu, "Subnanometre single-molecule localization, registration and distance measurements," *Nature*, vol. 466, pp. 647-651, 2010.
- [154] M. Wu, B. Huang, M. Graham, A. Raimondi, J. E. Heuser, X. Zhuang, and P. De Camilli, "Coupling between clathrin-dependent endocytic budding and F-BAR-dependent tubulation in a cell-free system," *Nature cell biology*, vol. 12, pp. 902-908, 2010.
- [155] B. Huang, W. Wang, M. Bates, and X. Zhuang, "Three-dimensional super-resolution imaging by stochastic optical reconstruction microscopy," *Science*, vol. 319, pp. 810-813, 2008.
- [156] G. Shtengel, J. A. Galbraith, C. G. Galbraith, J. Lippincott-Schwartz, J. M. Gillette, S. Manley, R. Sougrat, C. M. Waterman, P. Kanchanawong, and M. W. Davidson, "Interferometric fluorescent super-resolution microscopy resolves 3D cellular ultrastructure," *Proceedings of the National Academy of Sciences*, vol. 106, pp. 3125-3130, 2009.

- [157] A. Egner, C. Geisler, C. Von Middendorff, H. Bock, D. Wenzel, R. Medda, M. Andresen, A. C. Stiel, S. Jakobs, and C. Eggeling, "Fluorescence nanoscopy in whole cells by asynchronous localization of photoswitching emitters," *Biophysical journal*, vol. 93, pp. 3285-3290, 2007.
- [158] M. F. Juetten, T. J. Gould, M. D. Lessard, M. J. Mlodzianoski, B. S. Nagpure, B. T. Bennett, S. T. Hess, and J. Bewersdorf, "Three-dimensional sub-100 nm resolution fluorescence microscopy of thick samples," *Nature Methods*, vol. 5, pp. 527-529, 2008.
- [159] S. R. P. Pavani, M. A. Thompson, J. S. Biteen, S. J. Lord, N. Liu, R. J. Twieg, R. Piestun, and W. Moerner, "Three-dimensional, single-molecule fluorescence imaging beyond the diffraction limit by using a double-helix point spread function," *Proceedings of the National Academy of Sciences*, vol. 106, pp. 2995-2999, 2009.
- [160] J. Tang, J. Akerboom, A. Vaziri, L. L. Looger, and C. V. Shank, "Near-isotropic 3D optical nanoscopy with photon-limited chromophores," *Proceedings of the National Academy of Sciences*, vol. 107, pp. 10068-10073, 2010.
- [161] H. Su, L. Tang, Y. Wu, D. Tretter, and J. Zhou, "Spatially adaptive block-based super-resolution," *IEEE Transactions on Image Processing*, vol. 21, pp. 1031-1045, 2012.
- [162] S. Mallat and G. Yu, "Super-resolution with sparse mixing estimators," *Image Processing, IEEE Transactions on*, vol. 19, pp. 2889-2900, 2010.
- [163] H. Stark and P. Oskoui, "High-resolution image recovery from image-plane arrays, using convex projections," *JOSA A*, vol. 6, pp. 1715-1726, 1989.
- [164] W. Dong, L. Zhang, G. Shi, and X. Wu, "Image deblurring and super-resolution by adaptive sparse domain selection and adaptive regularization," *IEEE Transactions on Image Processing*, vol. 20, pp. 1838-1857, 2011.

- [165] T. E. Bishop, S. Zanetti, and P. Favaro, "Light field superresolution," *Proc. IEEE International Conference on Computational Photography (ICCP)*, pp. 1-9, 2009.
- [166] L. Zhang, H. Zhang, H. Shen, and P. Li, "A super-resolution reconstruction algorithm for surveillance images," *Signal Processing*, vol. 90, pp. 848-859, 2010.
- [167] M. M. Islam, V. K. Asari, M. N. Islam, and M. A. Karim, "Super-resolution enhancement technique for low resolution video," *IEEE Transactions on Consumer Electronics*, vol. 56, pp. 919-924, 2010.
- [168] K. Nguyen, S. Sridharan, S. Denman, and C. Fookes, "Feature-domain super-resolution framework for Gabor-based face and iris recognition," *Proc. IEEE Conference on Computer Vision and Pattern Recognition (CVPR)*, pp. 2642-2649, 2012.
- [169] R. R. Peeters, P. Kornprobst, M. Nikolova, S. Sunaert, T. Vieville, G. Malandain, R. Deriche, O. Faugeras, M. Ng, and P. Van Hecke, "The use of super - resolution techniques to reduce slice thickness in functional MRI," *International Journal of Imaging Systems and Technology*, vol. 14, pp. 131-138, 2004.
- [170] A. Rueda, N. Malpica, and E. Romero, "Single-image super-resolution of brain MR images using overcomplete dictionaries," *Medical Image Analysis*, vol. 17, pp. 113-132, 2013.
- [171] J. A. Kennedy, O. Israel, A. Frenkel, R. Bar-Shalom, and H. Azhari, "Super-resolution in PET imaging," *IEEE Transactions on Medical Imaging*, vol. 25, pp. 137-147, 2006.
- [172] M. D. Robinson, S. J. Chiu, J. Lo, C. Toth, J. Izatt, and S. Farsiu, "New Applications of Super-resolution in Medical Imaging," in *Super-Resolution Imaging*, P. Milanfar, Ed., ed Boca Raton, Florida, US: CRC Press, 2011, p. 383.
- [173] S. Farsiu, D. Robinson, M. Elad, and P. Milanfar, "Advances and challenges in super-resolution," *Int. J. Imaging Syst. Technol.*, vol. 14, pp. 47-57, 2004.

- [174] S. D. Babacan, R. Molina, and A. K. Katsaggelos, "Variational Bayesian Super Resolution," *IEEE Trans. Image Process.*, vol. 20, pp. 984-999, 2011.
- [175] Q. Wang, X. Tang, and H. Shum, "Patch based blind image super resolution," *Proc. IEEE International Conference on Computer Vision (ICCV)*, vol. 1, pp. 709-716, 2005.
- [176] H. Greenspan, "Super-Resolution in Medical Imaging," *Comput. J.*, vol. 52, pp. 43-63, January 1, 2009 2009.
- [177] Z. Qiu, L. Yang, and W. Lu, "A new feature-preserving nonlinear anisotropic diffusion for denoising images containing blobs and ridges," *Pattern Recognit. Lett.*, vol. 33, pp. 319-330, 2012.
- [178] Z. Qiu, L. Yang, and W. Lu, "A New Feature-preserving Nonlinear Anisotropic Diffusion Method for Image Denoising," *Proc. BMVC, 2011*, pp. 73.1--73.0, 2011.
- [179] S. Farsiu, M. D. Robinson, M. Elad, and P. Milanfar, "Fast and robust multiframe super resolution," *IEEE Trans. Image Process.*, vol. 13, pp. 1327-1344, 2004.
- [180] A. Zomet, A. Rav-Acha, and S. Peleg, "Robust super-resolution," in *Proc. IEEE CVPR 2001*, 2001, pp. 645-650.
- [181] S. C. Park, M. K. Park, and M. G. Kang, "Super-resolution image reconstruction: a technical overview," *IEEE Signal Processing Magazine*, vol. 20, pp. 21-36, 2003.
- [182] M. J. Black and P. Anandan, "The Robust Estimation of Multiple Motions: Parametric and Piecewise-Smooth Flow Fields," *Comput. Vis. Image Underst.*, vol. 63, pp. 75-104, 1996.
- [183] R. C. Aster, B. Borchers, and C. H. Thurber, *Parameter estimation and inverse problems*. NY, US: Academic Press, 2012.

- [184] D. Eberly, R. Gardner, B. Morse, S. Pizer, and C. Scharlach, "Ridges for image analysis " *Journal of Mathematical Imaging and Vision*, vol. 4, pp. 353-373, 1994.
- [185] I. Daubechies, R. DeVore, M. Fornasier, and C. S. n. Güntürk, "Iteratively reweighted least squares minimization for sparse recovery," *Commun. Pure Appl. Math.*, vol. 63, pp. 1-38, 2010.
- [186] P. Milanfar, *Super-resolution imaging* vol. 1. Boca Raton, FL, US: CRC Press, 2010.
- [187] S. Farsiu and P. Milanfar. (2007). *MDSP Super-Resolution and Demosaicing Datasets*. Available: <http://www.soe.ucsc.edu/milanfar/software/sr-datasets.html>
- [188] P. Frantsuzov, M. Kuno, B. Janko, and R. A. Marcus, "Universal emission intermittency in quantum dots, nanorods and nanowires," *Nat. Phys.*, vol. 4, pp. 519-522, 2008.
- [189] R. Tibshirani, "Regression shrinkage and selection via the lasso," *Journal of the Royal Statistical Society. Series B (Methodological)*, pp. 267-288, 1996.
- [190] I. Daubechies, M. Defrise, and C. De Mol, "An iterative thresholding algorithm for linear inverse problems with a sparsity constraint," *Communications on pure and applied mathematics*, vol. 57, pp. 1413-1457, 2004.
- [191] J. A. Hartigan and M. A. Wong, "Algorithm AS 136: A k-means clustering algorithm," *Journal of the Royal Statistical Society. Series C (Applied Statistics)*, vol. 28, pp. 100-108, 1979.
- [192] P. Chatterjee and P. Milanfar, "Clustering-based denoising with locally learned dictionaries," *Image Processing, IEEE Transactions on*, vol. 18, pp. 1438-1451, 2009.